LANCASTER UNIVERSITY

Solar Wind-Magnetosphere Interactions: A Statistical Analysis of Spacecraft Measurements

by

Nathan Case MPhys (Hons)

This thesis is submitted in partial fulfilment of the requirements
for the degree of Doctor of Philosophy

in the
Faculty of Science and Technology
Department of Physics

April 2014

Declaration of Authorship

I, Nathan Case, declare that this thesis titled 'Solar Wind-Magnetosphere Interactions: A Statistical Analysis of Spacecraft Measurements' and the work presented in it are my own. I confirm that:

- This work was done wholly or mainly while in candidature for a research degree at this University.
- Where any part of this thesis has previously been submitted for a degree or any other qualification at this University or any other institution, this has been clearly stated.
- Where I have consulted the published work of others, this is always clearly attributed.
- Where I have quoted from the work of others, the source is always given. With the exception of such quotations, this thesis is entirely my own work.
- I have acknowledged all main sources of help.
- Where the thesis is based on work done by myself jointly with others, I have made clear exactly what was done by others and what I have contributed myself.

Signed: _____

Date: _____

"Space is big. You just won't believe how vastly, hugely, mind-bogglingly big it is. I mean, you may think it's a long way down the road to the chemist's, but that's just peanuts to space."

—Douglas Adams

LANCASTER UNIVERSITY

Abstract

Faculty of Science and Technology
Department of Physics

Doctor of Philosophy

by Nathan Case MPhys (Hons)

When investigating solar wind-magnetosphere-ionosphere coupling, it is important to understand how the solar wind, and the interplanetary magnetic field (IMF) frozen into it, behaves as it reaches the Earth. Magnetic reconnection, for example, is a phenomenon whose morphology is governed by the IMF orientation and wields a large influence over many of the processes occurring within the magnetosphere. Exploiting nearly a decade of spacecraft data, primarily from ESA's Cluster mission and NASA's ACE mission, the three studies presented in this thesis aim to help improve the specification of the IMF at the magnetopause.

Presented in Chapter 4, a study is undertaken to determine the length of time it takes the solar wind to travel from an upstream observer, situated $\sim$ 240 R_E upstream of the Earth, to the near-Earth environment. By isolating those periods when the Cluster spacecraft were within the unimpeded solar wind, the study is able to compare near-Earth magnetic field data to data from the upstream observer ACE. Using a cross-correlation method to analyse these data provides nearly 5000 propagation delay times which are then compared to a simple "flat-delay" (i.e. distance/speed) and to the frequently used OMNIweb data set. The results of the study show that statistically both methods are similar and provide good estimates, however, there are times when the estimated propagation delay is significantly different from the observed delay.

The boundary between the solar wind and the Earth's terrestrial magnetic field is known as the magnetopause. This boundary is an important region for solar wind-magnetospheric coupling as it is one of the primary locations for magnetic reconnection.

To study the magnetopause, it is pivotal to know its location, however, this is non-trivial since the magnetopause is not static but is instead located where there is a pressure balance between the changing solar wind and the magnetosphere. In Chapter 5 the Cluster satellites are used to determine the location of the magnetopause. Over 2709 individual locations, spread over varying magnetic latitudes and local times, are recorded and compared to four frequently-used magnetopause models. The results show that two of the models overestimate the distance to the magnetopause (by $\sim 1\ R_E$) and that two underestimate it (by $\sim 0.5\ R_E$ and $\sim 0.25\ R_E$ respectively).

As the solar wind approaches the Earth's magnetosphere it is slowed and a bowshock is formed. Inside this bowshock, the solar wind is turbulent and the orientation of the magnetic field changes through a process known as magnetic draping. In Chapter 6, an investigation of eight years worth of near-magnetopause magnetic field data, provided by the Cluster mission, is undertaken and the changes in magnetic field orientation are presented. Over the course of 2688 magnetopause crossings, it is found that the upstream IMF conditions have a considerable impact upon the amount of modification of the orientation of the magnetic field as does the location of the recording on the magnetopause. Overall, only 13% of data points exhibit "perfect draping" (where the y- and z- components of the magnetic field are not substantially affected by the magnetosheath traversal).

Acknowledgements

I would firstly like to thank my supervisor, Prof. Jim Wild, for the continued support and guidance that he has given throughout the course of my PhD. Jim provided me with an STFC-funded opportunity to undertake my PhD studies in the Space Plasma and Radio Science (SPEARS) group at Lancaster University and for that I am very grateful.

Secondly, I would like to thank my wife and my parents for their unwavering support and encouragement. Though I am sure that they must have grown tired of my magnetospheric mutterings, without them this thesis would never have been written.

I would also like to thank the rest of the members of the SPEARS group, past and present, for their help and advice. A special mention must be made to Carl Bryers, Patrick Cannon, Dave Hartley and Rob Kidd whose friendship has helped make this PhD an enjoyable experience.

The data used in this thesis originate from several sources. I gratefully acknowledge the NASA/GSFC Space Physics Data Facility's OMNIweb service for their data. In addition I also acknowledge the Cluster Active Archive data facility and the Cluster FGM and CIS teams for the use of their Cluster data.

Contents

List of Figures

List of Tables

Abbreviations

ACE	**A**dvanced **C**omposition **E**xplorer
CAA	**C**luster **A**ctive **A**rchive
CIS	**C**luster **I**on **S**pectrometry
DPU	**D**ata **P**rocessing **U**nit
ESA	**E**uropean **S**pace **A**gency
FOV	**F**ield **o**f **V**iew
FGM	**F**lux**g**ate **M**agnetometer
GSE	**G**eocentric **S**olar **E**cliptic
GSM	**G**eocentric **S**olar **M**agnetospheric
HIA	**H**ot **I**on **A**nalyzer
IMF	**I**nterplanetary **M**agnetic **F**ield
MHD	**M**agneto**h**ydro**d**ynamics
NASA	**N**ational **A**eronautics and **S**pace **A**dministration
PFN	**P**hase **F**ront **N**ormal
RPA	**R**etarding **P**otential **A**nalyzer
TOF	**T**ime **o**f **F**light

Physical Constants

Astronomical Unit	AU	=	1.49598×10^{11} m
Boltzmann Constant	k_B	=	1.38065×10^{23} J/K
Electron Volt	eV	=	1.60218×10^{-19} J
Earth radius (mean)	R_E	=	6.371×10^{6} m
Solar mass	$M_\odot$	=	1.98855×10^{30} kg
Solar radius	$R_\odot$	=	6.995×10^{8} m
Speed of Light	c	=	2.99792×10^{8} m/s
Vacuum Permittivity	ϵ_0	=	8.85419×10^{-12} F/m

Chapter 1

Introduction

Space weather, a term first used in the 1990s, refers to conditions on the Sun, in the solar wind and in the near-Earth environment that can influence the performance and reliability of space-borne and ground-based technological systems and can endanger human life or health (*Wright et al.*, 1995). Though this definition is a relatively new one, the effects of space weather have interested mankind for millennia; from prehistoric petroglyphs to modern satellite missions, we have been documenting the effect of the Sun on the Earth and on us. Whilst it is highly unlikely that prehistoric rock art of the aurora forms meaningful understanding of the processes behind space weather, it shows that, even in prehistoric times, we were interested in space weather and recording its effects here on Earth.

Our understanding of space weather has, of course, evolved over time with varying forms of understanding existing throughout human history. Ancient tales in Nordic countries attribute the aurora to Ullr (the god of winter and death), whilst in medieval

times red auroral displays were considered a sign of ill omen from the Heavens. A more formal understanding started to develop during the 17th and 18th centuries, with Henry Cavendish (*Cavendish*, 1790) making the first quantifiable recordings of an aurora by estimating its height above the ground. In the 19th century, Richard Carrington (*Carrington*, 1859) made the first documented connection between high solar activity and an extreme geomagnetic storm - an event which became known as the Carrington Event. Afterwards, space weather became an active area of scientific research and, upon commencement of the space age, mankind was able to measure the effects of the Sun on the near-Earth environment *in situ*.

The driver behind space weather is, of course, the Sun. This main sequence star located at the center of the solar system is roughly 4.6 billion years old, has a diameter of around 109 times that of Earth and has a mass of 1.989×10^{30} kilograms (approximately 330,000 times the mass of Earth). The Sun is composed of approximately 71% hydrogen and 27% helium, with a smaller amount of heavier elements such as oxygen and carbon. The hydrogen in the Sun's core is continually being converted through nuclear fusion to produce helium. Through this nuclear reaction the Sun produces huge amounts of energy which is then expelled into the solar system.

Approximately 1400 W/m^2 of solar energy, in the form of electromagnetic radiation, is continually deposited on the Earth. Additionally, solar mass is transported out into the solar system through the solar wind.

The solar wind is a continual, but variable, outflow of plasma and it carries the Sun's magnetic field frozen within it (the concept of frozen-in flow is discussed in detail in section 2.3.2). The time it takes for the solar wind to reach Earth is also variable but is

generally of the order of one hour. Since the plasma is composed of electrically charged particles and has the interplanetary magnetic field (IMF) embedded within it, it interacts with the Earth's own magnetic field.

The Earth's terrestrial magnetic field, roughly dipolar in nature, creates a magnetic bubble or cavity surrounding the Earth known as the magnetosphere. As discussed in section 2.4, the magnetosphere is somewhat distorted from a dipole field due to the interaction with IMF: the dayside magnetosphere is compressed whilst the nightside magnetosphere is extended into a long tail region. Through a process known as magnetic reconnection, which is discussed in section 2.4.4, the magnetosphere is coupled with the solar wind and is affected by changes in it.

The Earth's upper atmosphere, known as the ionosphere, is also connected to the solar wind through the changes in the magnetosphere. For example, energetic particles, which originate in the solar wind and are accelerated along magnetic field lines in the magnetosphere, bombard the neutral atoms in the ionosphere producing the aurorae.

There has been much research into how the Sun and the solar wind interact with our terrestrial environment and what effects it can have on life here on Earth - such as enhanced solar activity resulting in the disruption of national power grids. Although today we understand many of the complex intricacies of the relationship between the Sun and the Earth, research into this field is still ongoing and many issues, such as the processes behind the acceleration of the solar wind, remain unresolved.

In order to resolve such issues, we must first be able to accurately determine when events occurring on the Sun might reach the Earth and how they might evolve during

that journey. The main theme of the research in this thesis is to investigate mapping solar wind data from an upstream observer to the Earth.

The structure of this thesis is as follows: firstly, a theory chapter covers the fundamentals of solar terrestrial physics. This theory chapter will cover the basic properties of plasmas and charged particles as well as the formation of the solar wind. The chapter will then discuss the near-Earth magnetic environment and how the solar wind interacts with it. The effects of this interaction will then also be detailed.

A chapter on the data and instrumentation used in the research for this thesis is then provided. The chapter explores the different data sources and satellite missions exploited during the research, going into further detail about the specific instruments used.

Three research chapters follow, each investigating a certain aspect of the journey of the solar wind as it traverses from an upstream observer to Earth. Chapter 4 looks at the propagation delay time between an upstream observer and arrival at the Earth. Chapter 5 studies the effect the solar wind has on the Earth's magnetic environment - specifically the location of the boundary between the solar wind regime and the Earth's terrestrial magnetic field regime. This boundary, known as the magnetopause, is discussed further in section 2.4.2. Chapter 6 then investigates the orientation changes of the magnetic field as it drapes over this boundary.

It should be noted that the research presented in Chapters 4 and 5 has been published in a peer-reviewed journal. This is indicated at the beginning of these chapters.

Finally, a conclusion chapter summarises the current research in the field and highlights possible further areas of research.

Chapter 2

Background Theory

2.1 Basics of Plasma Physics

Of the four fundamental states of matter, plasma is by far the most abundant in the observable Universe, with estimates suggesting that more than 99% of all known matter is in the plasma state (*Baumjohann and Treumann*, 1996). Plasma is a gas of electrically charged particles in which the number of negatively charged particles is roughly equal to the number of positively charged particles. Both positive and negative charge carriers are evenly distributed throughout a plasma resulting in average charge neutrality, though transient electrically charged regions may exist for periods of time. This equality between the density of both negative and positive charge carriers on a large scale, along with possible smaller regions of charge imbalance, is known as quasineutrality.

In most plasmas, except for extremely dense plasmas such as the interior of the Sun, the average kinetic energy of a particle is much larger than the average potential energy

between the particle and its neighbours. This is the definition of a free particle.

For the plasma state to exist, three fundamental criteria must be fulfilled. Each of these will now be discussed in turn.

2.1.1 Debye Shielding

A single stationary point-like charged particle (e.g. an electron of charge e), in the absence of any other charged particle, produces an electrostatic field ($\mathbf{E}$) as described by the Poisson equation (*Gombosi*, 1998):

$$\nabla \cdot \mathbf{E} = \frac{e}{\epsilon_0}\delta^3(\mathbf{r}) \tag{2.1}$$

where $\delta(\mathbf{x})$ is the Dirac delta function, ϵ_0 is the vacuum permittivity and $\mathbf{r}$ is the radial unit vector. The solution to equation 2.1 is well known and is the electric field of a single charge:

$$\mathbf{E}_0(\mathbf{r}) = \frac{e}{4\pi\epsilon_0}\frac{\mathbf{r}}{r^3} \tag{2.2}$$

where r is the distance from the charged particle.

Since $\nabla \times \mathbf{E}_0 = 0$, the electric field vector can be expressed in terms of a scalar potential as $\mathbf{E}_0 = -\nabla\psi_0$ where the scalar potential is:

$$\psi_0(\mathbf{r}) = \frac{e}{4\pi\epsilon_0 r} \tag{2.3}$$

This scalar potential is known as the Coulomb Potential and it describes the electric potential field created by a stationary point-like charged particle. The effect of the Coulomb Potential is that particles of the opposite charge to the point-like charged particle are attracted to it whilst particles of a similar charge (e.g. both negatively charged) are repelled from it. In a plasma, where there is an abundance of both negatively and positively charged particles, a "cloud" of oppositely charged particles forms around a single charged particle. This effect is known as *Debye Shielding*.

Due to the Debye Shielding, the single point charge is no longer in the absence of other charged particles and so the electric potential field differs from ψ_0 in equation 2.3. The new potential, known as the Debye potential (ψ_D), can be expressed as a function of the original potential:

$$\psi_D = \psi_0(\mathbf{r}) \exp\left(-\frac{r}{\lambda_D}\right) \tag{2.4}$$

where λ_D is a parameter known as the Debye length and is defined as:

$$\lambda_D = \sqrt{\frac{\epsilon_0 k_B T}{e^2 n}} \tag{2.5}$$

where k_B is the Boltzmann constant, T is the effective plasma temperature and n is the electron/ion density.

The result of Debye potential, given in equation 2.4, is that at distances larger than the Debye length the effective potential of the single point charge diminishes exponentially due to Debye Shielding. At lengths much greater than the Debye length (i.e. $L >> \lambda_D$),

the electro-static force from individual charges is essentially zero and so the plasma is quasineutral. This is the first criterion of a plasma.

2.1.2 Plasma Parameter

Several definitions exist for the term plasma parameter, including "the ratio of the average potential and kinetic energies in the plasma" or "the ratio of the maximum impact parameter to the classical distance of closest approach in Coulomb scattering". If it is defined as the latter, then the plasma parameter (Λ) is given by:

$$\Lambda = 4\pi n {\lambda_D}^3 \tag{2.6}$$

Another definition for the plasma parameter is "the number of electrons in a plasma contained within a Debye sphere" (a sphere with a radius equal to the Debye length) and is given by:

$$N_D = \frac{4}{3}\pi n {\lambda_D}^3 \tag{2.7}$$

These two different definitions for the plasma parameter only vary by a small numerical amount and so are often used interchangeably. Regardless of which definition is used, the second plasma criterion is that the plasma parameter of the ionised gas must be large e.g. $\Lambda >> 1$.

2.1.3 Plasma Frequency

When the quasineutrality of a plasma is disturbed by some external force, the electrons (and to a lesser extent the ions) oppose the disturbance to restore charge neutrality. Due to their inertia, they oscillate around the equilibrium position. The frequency of this oscillation is known as the plasma frequency (ω_p).

According to Poisson's equation (equation 2.1), a displacement of the charge carriers in a plasma results in a uniform electric field in the direction of the net displacement (δ) (*Gombosi*, 1998):

$$E = \frac{en}{\epsilon_0}\delta \tag{2.8}$$

where e is the standard electrical charge and n is the number density of charge carriers. The equations of motion for the electrons and ions are:

$$\begin{aligned} m_e\frac{d^2\delta_e}{dt^2} &= -eE \\ m_i\frac{d^2\delta_i}{dt^2} &= eE \end{aligned} \tag{2.9}$$

where m_e and m_i are the electron and ion masses, respectively. Combining the equations of motion gives the oscillating relative motion between the ions and electrons:

$$\begin{aligned}\frac{d^2\delta}{dt^2} &= \frac{d^2\delta_e}{dt^2} - \frac{d^2\delta_i}{dt^2} \\ &= -\left(\frac{e^2 n}{\epsilon_0 m_e} + \frac{e^2 n}{\epsilon_0 m_i}\right)\delta\end{aligned} \tag{2.10}$$

The frequency of the oscillation, as described in equation 2.10, is the *plasma frequency* and is the sum of the squares of the oscillation frequencies of the electrons (ω_{pe}) and the ions (ω_{pi}):

$$\omega_p{}^2 = \omega_{pe}{}^2 + \omega_{pi}{}^2 \tag{2.11}$$

where ω_{pe} and ω_{pi} are given by

$$\omega_{pe} = \sqrt{\frac{e^2 n}{\epsilon_0 m_e}} \tag{2.12}$$

$$\omega_{pi} = \sqrt{\frac{e^2 n}{\epsilon_0 m_i}} \tag{2.13}$$

as can be seen from equation 2.10.

Since the mass of the ions is much greater than the mass of the electrons ($m_i >> m_e$), the oscillation frequency of the electrons is much higher than that of the ions ($\omega_{pe} >> \omega_{pi}$). The plasma frequency is therefore approximately equal to the electron plasma frequency ($\omega_p \approx \omega_{pe}$). It is also clear that the plasma frequency is dependant upon the density of the charge carriers in the plasma.

In some plasmas, such as the Earth's ionosphere, there is a substantial contamination of neutral ions. If the charged particles in the plasma frequently collide with these neutrals then the medium behaves less like a plasma and more like a normal gas. For the plasma state to remain, the time average between two charged-neutral particle collisions (τ_n) must be larger than the reciprocal of the plasma frequency, i.e. $\omega_p \tau_n >> 1$. This is the third plasma criterion.

2.2 Charged Particle Motion

In the solar wind plasma, the mean free path of the charge carriers is so large ($\sim$ 1AU for solar wind protons) that they can be considered collisionless. In the absence of collisions and in the presence of electromagnetic fields, a single charged particle will behave in a fairly predictable way. The starting point to understanding the behaviour is to know that the motion of a charged particle in such a system is governed by the Lorentz force ($\mathbf{F}_L$):

$$\mathbf{F}_L = q\left(\mathbf{E} + \mathbf{v} \times \mathbf{B}\right) \tag{2.14}$$

which, in the context of a single particle, can be expressed as:

$$m\frac{d\mathbf{v}}{dt} = q\left(\mathbf{E} + \mathbf{v} \times \mathbf{B}\right) + \mathbf{F}_g \tag{2.15}$$

where m is the mass of the particle, $\mathbf{v}$ is its total velocity and q is its charge. The term $\mathbf{F}_g$ represents nonelectromagnetic forces, such as the gravitational force.

2.2.1 Particle Gyration

For a particle in a magnetic field which is both uniform and unchanging, and in the absence of an electric field (i.e. $\mathbf{E} = 0$), the charged particle will experience cyclotron gyration.

Ignoring nonelectromagnetic forces and if $\mathbf{B}$ is assumed to act in the $\hat{\mathbf{z}}$ direction only, i.e. $\mathbf{B} = B\hat{\mathbf{z}}$, then the equation of motion, given in equation 2.15, becomes:

$$\frac{d\mathbf{v}}{dt} = \frac{q}{m}\mathbf{v} \times \mathbf{B} = \frac{q}{m}\begin{bmatrix} \hat{\mathbf{x}} & \hat{\mathbf{y}} & \hat{\mathbf{z}} \\ v_x & v_y & v_z \\ 0 & 0 & \mathbf{B} \end{bmatrix} \tag{2.16}$$

which gives:

$$\frac{dv_x}{dt} = \frac{qB}{m}v_y \tag{2.17}$$

$$\frac{dv_y}{dt} = -\frac{qB}{m}v_x \tag{2.18}$$

$$\frac{dv_z}{dt} = 0 \tag{2.19}$$

Equations 2.17 and 2.18 imply that the particle has a circular motion perpendicular to $\mathbf{B}$ (i.e. in the x/y plane) with angular frequency Ω:

$$\Omega = \frac{q\mathbf{B}}{m} \tag{2.20}$$

This angular frequency is often referred to as the cyclotron frequency or gyrofrequency. The radius of this circular motion, centred about the magnetic field line, is often known as the Larmor radius (r_L) or gyroradius and is given by:

$$r_L = \frac{v_\perp}{\Omega} = \frac{mv_\perp}{q\mathbf{B}} \tag{2.21}$$

where $v_\perp$ is the perpendicular velocity and is constant for all particles of the same species. Equations 2.20 and 2.21 show that heavier particles, of the same charge, will rotate at a lower gryofrequency and at a larger gyroradius and that particles with a faster perpendicular velocity will also rotate at a larger gyroradius. Ions and electrons, owing to their opposite electric charge, will rotate in opposite directions.

In addition to the circular component of the velocity, equation 2.19 shows that particles travel with a constant velocity along the magnetic field line. The combination of the parallel and perpendicular velocities results in a helix motion along the field line, as shown in Figure 2.1.

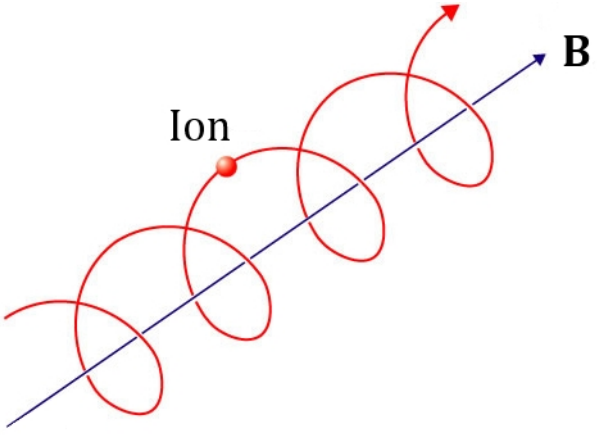

FIGURE 2.1: Cyclotron motion of an ion along a uniform and steady magnetic field line (Image credit: EFDA).

2.2.2 Electric Field Drift

If there is an electric field influencing the charged particle, then the equations of motion change from those discussed in section 2.2.1. If the field is chosen to lie in the x-z plane, so that $E_y = 0$, then the equation of motion, given in equation 2.15, has the components:

$$\frac{dv_x}{dt} = \frac{q}{m}E_x \pm \Omega v_y \tag{2.22}$$

$$\frac{dv_y}{dt} = -\Omega v_x \tag{2.23}$$

$$\frac{dv_z}{dt} = \frac{q}{m}E_z \tag{2.24}$$

To determine the velocity components, these equations are integrated. For v_z this is trivial and is given by:

$$v_z = v_{z_0} + \frac{qE_z}{m}t \tag{2.25}$$

which shows that the particle is accelerated along the field line. Note that in space plasmas, the component of an electric field parallel to the direction of the magnetic field will usually vanish. This is because the parallel component of the electric field will accelerate electrons and ions along the magnetic field line in opposite directions, as shown by equation 2.25, thus creating a charge imbalance and destroying the parallel electric field.

The electric field modifies the y-component of the velocity by superimposing a $-\frac{E_x}{B}$ term into it. The effect of this is to cause a drifting (of velocity v_{gc}) of the guiding centre of the gyroradius (this is in the $-y$ direction for positive E_x). The perpendicular component of v_{gc} is defined as the electric field drift velocity (v_E) and is given by:

$$v_E = \frac{\mathbf{E} \times \mathbf{B}}{B^2} \tag{2.26}$$

The physical result of this is that, during the first half of an ion's orbit about a magnetic field line, it is accelerated in $v_\perp$ by the electric field which increases its r_L. During the second half of the orbit, the electric field decelerates the ion and reduces r_L. The particle's helix shaped motion, which is formed in the absence of a magnetic field, is hence deformed from that shown in Figure 2.1.

This drifting of the guiding centre, often termed the E-cross-B drift, does not introduce currents into the plasma as the drift is independent of any of the characteristics of the particles themselves (e.g. q, m or $v_\perp$). Both positive and negative charge carriers drift in the same direction and with the same speed, regardless of mass.

2.2.3 Magnetic Field Drift

The magnetic field in which the particle inhabits can be quite variable. Two obvious variations are gradients in the field strength and a curvature of the field lines. Both of these have an impact on the motion of a charged particle orbiting along the magnetic field line.

In the case of a gradient of the magnetic field, in a direction perpendicular to the direction of the magnetic field, a similar effect to that found with a non-zero electric field is created. Using the Lorentz force and taking a Taylor expansion of the **B** field (assuming that the scale length of the magnetic field gradient is much larger than the gyroradius), it is possible to find that a force is produced (e.g. F_y):

$$F_y = \pm q v_\perp r_L \frac{1}{2}\frac{\partial \mathbf{B}}{\partial y} \tag{2.27}$$

and that a guiding centre drift velocity is formed:

$$\mathbf{v}_{gc} = \frac{1}{q}\frac{\mathbf{F}\times\mathbf{B}}{B^2} = \frac{1}{q}\frac{F_y}{B}\hat{\mathbf{x}} = \pm\frac{v_\perp r_L}{B}\frac{1}{2}\frac{\partial B}{\partial y}\hat{\mathbf{x}} \tag{2.28}$$

Since the choice of direction was arbitrary, this can be generalised to provide the grad-B drift velocity ($\mathbf{v}_{\nabla B}$):

$$\mathbf{v}_{\nabla B} = \pm\frac{v_\perp r_L}{2}\frac{\mathbf{B}\times\nabla B}{B^2} \tag{2.29}$$

The grad-B drift causes electrically charged particles to drift (in opposite directions for electrons and ions) perpendicular both to the magnetic field direction and to the direction of the field gradient. Thus a current, transverse to the magnetic field, is formed.

If the magnetic field lines are curved, with a constant radius of curvature $\mathbf{R}_c$, then another type of drift is encountered by the charged particles. Travelling along a curved

field introduces the centrifugal force into the particle's motion. The average centrifugal force ($\mathbf{F}_{cf}$) is given by:

$$\mathbf{F}_{cf} = \frac{mv_{\parallel}^2}{\mathbf{R}_c}\hat{r} = mv_{\parallel}^2\frac{\mathbf{R}_c}{R_c^2} \tag{2.30}$$

which, by replacing $q\mathbf{E}$ for $\mathbf{F}_{cf}$ in equation 2.15, gives rise to a drift:

$$\mathbf{v}_r = \frac{1}{q}\frac{\mathbf{F}_{cf}\times\mathbf{B}}{B^2} = \frac{mv_{\parallel}^2}{qB^2}\frac{\mathbf{R}_c\times\mathbf{B}}{R_c^2} \tag{2.31}$$

where $\mathbf{v}_r$ is known as the curvature drift. This drift, like the grad-B drift, causes electrons and ions to drift perpendicular to the magnetic field line.

In the case of the near-Earth environment, the curvature drift and the grad-B drift combine since there is a gradient in the magnetic field, depending upon the distance from the Earth, and there is a curvature drift due to the field lines connecting at the magnetic poles. The total magnetic field drift ($\mathbf{v_t}$) is simply an addition of the curvature and grad-B drifts:

$$\mathbf{v}_t = \frac{m}{q}\frac{\mathbf{R}_c\times\mathbf{B}}{R_c^2B^2}\left(v_{\parallel}^2 + \frac{1}{2}v_{\perp}^2\right) \tag{2.32}$$

The total magnetic field drift causes the electrons to flow in an easterly direction about the Earth and the ions to flow in a westerly direction - creating a current around the Earth.

2.2.4 Magnetic Mirroring

In the case of converging field lines, such as at the Earth's magnetic poles, the magnetic field strength changes along the field line with particularly strong magnetic field near the poles. A particle on one of these converging field lines will be subjected to a force along the field line (F_z) of:

$$F_z = -\mu \frac{\partial B_z}{\partial z} \tag{2.33}$$

where μ is known as the magnetic moment of the gyrating particle and is given by:

$$\mu \equiv \frac{1}{2} \frac{m v_\perp^2}{B} \tag{2.34}$$

Equation 2.33 can be can be generalised to:

$$\mathbf{F}_\parallel = -\mu \nabla_\parallel B \tag{2.35}$$

As the particle moves into a different strength magnetic field region its gyroradius changes, but its magnetic moment remains invariant. This can be shown by using the principle of the conservation of energy and the definition of the magnetic moment (equation 2.34):

$$\frac{d}{dt}\left(\frac{1}{2} m v_\parallel^2 + \frac{1}{2} m v_\perp^2\right) = \frac{d}{dt}\left(\frac{1}{2} m v_\parallel^2 + \mu B\right) = 0 \tag{2.36}$$

From equation 2.35, it can be found that:

$$\frac{d}{dt}\frac{mv_{\parallel}^2}{2} = -\mu\frac{dB}{dt} \tag{2.37}$$

Combining equations 2.36 and 2.37;

$$-\mu\frac{dB}{dt} + \frac{d}{dt}(\mu B) = 0 \tag{2.38}$$

If B is assumed to be time invariant then only the second term of this equation remains. Differentiation of this second term results in:

$$B\frac{d\mu}{dt} = 0 \tag{2.39}$$

and, since B is non-zero in this case, it is shows that μ does not vary over time (or is invariant).

So, in the case of a particle moving into a stronger field region (where B is increasing), the particle's $v_{\perp}$ must increase so that μ may remain constant. Additionally, since energy must be conserved (as shown in equation 2.36), an increase in $v_{\perp}$ must result in a decrease in $v_{\parallel}$. If B is large enough, $v_{\parallel}$ is reduced to zero and then, if stronger still, it will cause $v_{\parallel}$ to change sign. At which point, the particle is reflected back along the magnetic field line. The point at which the particle is reflected by this mirror force is known as the mirror point. If the particle is not lost from the magnetic field line, through collisions with the atmosphere, it will continually bounce between two mirror

points (one near the North pole and one near the South). Collision with the atmosphere may occur if the particle's pitch angle, α (the angle between the velocity vector of the particle and the magnetic field vector), is sufficiently small. A small pitch angle, as shown in equation 2.40, occurs when the particle's velocity is dominated by the parallel component.

$$\alpha = \tan^{-1}\left(\frac{v_{\perp}}{v_{\parallel}}\right) \tag{2.40}$$

In the case where the parallel component of the velocity is dominant, one can think of the mirror point of the particle being located inside the atmosphere and so a collision with an atmospheric particle becomes more likely.

2.3 The Solar Wind

The solar wind is a high-speed plasma outflow which originates from the Sun's corona and terminates at the boundary of interstellar space (some 160 AU from the Sun). This boundary, known as the heliopause, has only recently been crossed by any man-made object[1].

The first suggestion of a continuous solar wind was made by *Biermann* (1951), based upon studies of comet tails, with a subsequent detailed mathematical theory of the solar wind provided by *Parker* (1958). The first spacecraft observations of the solar wind were made by the Lunik 2 and 3 spacecraft in 1960 and the Mariner 2 spacecraft in 1966.

[1]NASA's Voyager 1 spacecraft crossed the heliopause on August 25, 2012

As the solar wind flows through the heliosphere its properties, such as speed and temperature, change. In table 2.1, the average values for several solar wind properties at 1AU are given.

Table 2.1: Average solar wind properties at 1AU

Property	Value
Flow speed	450 $km \cdot s^{-1}$
Travel time	3.5 $\times 10^5$ s
Proton density	6.6 cm^{-3}
Proton temperature	1.2 $\times 10^5$ K
Electron density	7.1 cm^{-3}
Electron temperature	1.4 $\times 10^5$ K
Avg. electron collision time	3.5 $\times 10^6$ s
Magnetic field strength	7.0 nT

The solar wind is composed mainly of an equal number of electrons and protons, approximately 8% ionised helium and trace amounts of other heavier elements.

The classical approach to describe how the solar wind is formed in the Sun's corona is using hydrostatic equilibrium equations and this approach, as well as its limitations, will now be discussed.

2.3.1 Solar Wind Formation

The basic understanding for the formation of the solar wind was built using a fluid model to describe an equilibrium state of the solar corona. The starting point for this model is to use the equations for conservation of mass and momentum in a fluid - since the solar wind is assumed to be a fully ionised, quasineutral plasma. By ignoring the effects of any magnetic fields and heat conduction, the conservation equations become:

$$
\begin{aligned}
&i)\ \frac{1}{r}\frac{d}{dr}(r^2\rho u) = 0 \\
&ii)\ \rho u\frac{du}{dr} + \frac{dp}{dr} + \rho\frac{GM_\odot}{r^2} = 0 \\
&iii)\ \frac{3}{2}u\frac{dp}{dr} + \frac{5}{2}p\frac{1}{r^2}\frac{d}{dr}(r^2u) = 0
\end{aligned}
\tag{2.41}
$$

where ρ, u and p are the mass density, radial velocity and pressure of the solar wind, respectively, r is radial distance from the co-ordinate origin (i.e. the center of the Sun) and $M_\odot$ is the solar mass (*Gombosi*, 1998). The simplest solution to equations 2.41 is to assume that the solar corona is stationary (i.e. $u = 0$). In this case, only the momentum equation remains:

$$\frac{dp_s}{dr} + \rho_s\frac{GM_\odot}{r^2} = 0 \tag{2.42}$$

where the "s" subscript indicates the static case. Assuming an isothermal corona, the equation for pressure in a hydrostatic equilibrium becomes:

$$\frac{dp_s}{dr} + p_s\frac{m_p}{2k_BT}\frac{GM_\odot}{r^2} = 0 \tag{2.43}$$

since $\rho_s = p_s\frac{m_p}{2k_BT}$. The solution to equation 2.43 is:

$$p_s = p_\odot \exp\left[\frac{GM_\odot m}{2k_BT}\left(\frac{1}{r} - \frac{1}{R}\right)\right] \tag{2.44}$$

where $p_\odot$ is the pressure at the base of the solar corona (at a distance R). An interesting point to note about this solution is that at distances $r \to \infty$, p_s does not vanish:

$$p_\infty = p_\odot \exp\left[\frac{GM_\odot m}{2k_B TR}\right] \tag{2.45}$$

The solution, as given in equation 2.44, assumes a constant gravitational field throughout the heliopause which is clearly unrealistic. Additionally, for a coronal temperature of 10^6K, the pressure at $r \to \infty$ would be approximately 10^{-4} of $p_\odot$. This is many orders of magnitude higher than expected and thus cannot represent an equilibrium state between the solar corona and the interstellar medium (*Kivelson and Russell*, 1995).

After understanding that a hot, static corona cannot exist, it was in *Parker* (1960) that a coronal solution with non-zero radial velocities was first conceived. In a steady-state spherically symmetrical corona (the simplest case), the pressure gradient can be expressed by simply re-arranging the energy equation (given in equation 2.41 (iii)):

$$\frac{dp}{dr} = -\frac{5}{3}\frac{p}{u}\frac{du}{dr} - \frac{10}{3}\frac{p}{r} \tag{2.46}$$

This can then be substituted into the momentum equation (equation 2.41 (ii)) to give:

$$\frac{u^2 - {a_s}^2}{u}\frac{du}{dr} = \frac{2{a_s}^2}{r} - \frac{GM_\odot}{r^2} \tag{2.47}$$

where ${a_s}^2 = \frac{5p}{3\rho}$ and describes the local speed of sound. Integrating equation 2.47, and assuming an isothermal corona where a_s is constant, gives a fairly good approximation

of the solar corona:

$$\frac{1}{2}u^2 - {a_s}^2 \ln(u) = 2{a_s}^2 \ln(r) + \frac{GM_\odot}{r} + c \tag{2.48}$$

where c is a constant of integration. There are five mathematically valid classes of isothermal solutions, as shown in Figure 2.2, which are a result of the integration constant. A full description of these classes can be found in *Gombosi* (1998).

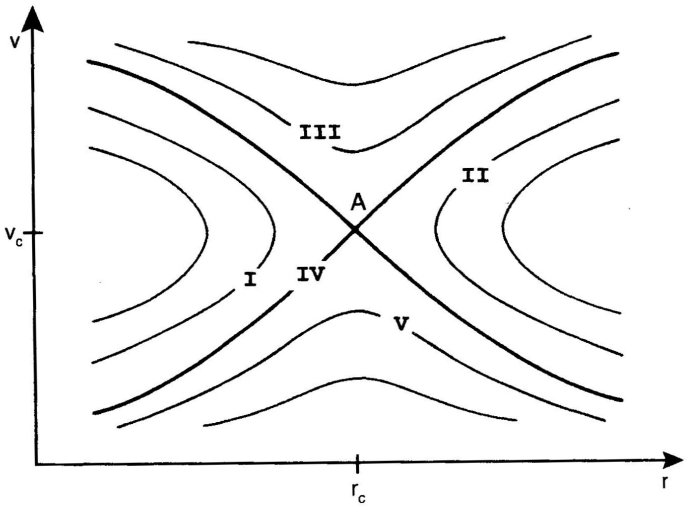

FIGURE 2.2: Mathematically admissable classes of isothermal solutions of an expanding corona (*Gombosi*, 1998).

The solution hence used is solution IV, in which the solar wind is subsonic at the base of the corona and is then accelerated to supersonic speeds at the sonic point (r_c):

$$r_c = \frac{3}{5}\frac{mGM_\odot}{2k_B T} \tag{2.49}$$

This suggests a sonic point located at around 4-6$R_\odot$ (solar radii), though it is now thought that the sonic point is located at around 1$R_\odot$. Clearly, the simplified solution

given here fails to fully account for the acceleration process of the solar wind and there must be further acceleration mechanisms involved. Research into coronal heating and solar wind acceleration mechanisms, such as ion cyclotron waves, is still on-going.

Both of the approaches used above assume a spherically symmetrical, isothermal, coronal outflow which is obviously an unrealistic simplification. In fact, the corona is asymmetrical and the solar wind has several source regions - with the solar wind properties depending upon which region it originated from. The two primary types of solar wind are known as "slow" solar wind ($v_{slow} \approx 350$ km·s^{-1}) and "fast" solar wind ($v_{fast} \approx 650$ km·s^{-1}).

The source of the long-lived fast solar wind is perhaps the most well understood. High speed streams of solar wind escape from coronal holes (regions of open magnetic field lines) and travel out relatively unrestricted by the Sun's magnetic field into the heliosphere. The plasma in a coronal hole is cooler and lower in density than on average and so the high speed solar wind is also cooler and lower in density. It is thought that low speed flows tend to originate from the outer regions of coronal streamers that straddle regions of magnetic polarity reversals. The location of the high and slow outflow regions is dependant upon the solar activity, with slow outflows located between latitudes of $\pm \sim 35$ degrees around the solar equator during solar minimum (when the Sun's activity is at its lowest) and moving pole-ward during solar maximum (see Figure 2.3).

Another source of solar wind plasma are large transient events called coronal mass ejections (CMEs). Though CMEs can form in several ways, magnetic reconnection of complex field lines in the solar corona is considered to be the primary driver behind them

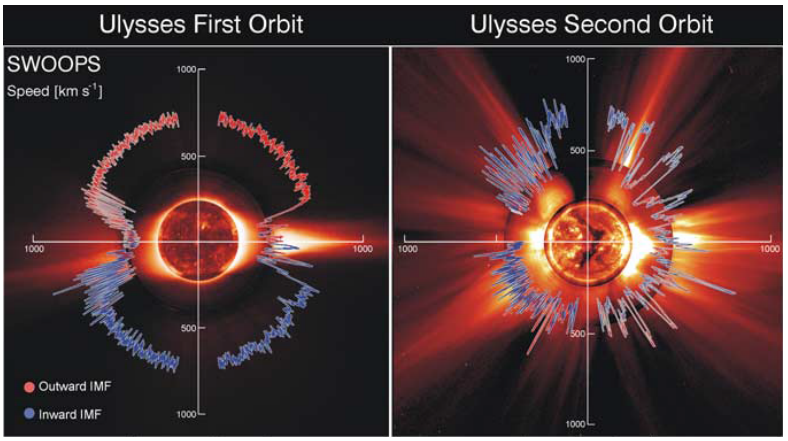

FIGURE 2.3: Polar plots of solar wind speed as a function of latitude for the Ulysses spacecraft's first two solar orbits. The first orbit was during solar minimum whilst the second was during solar maximum (*McComas et al.*, 2003).

(*Antiochos et al.*, 1999). The process of magnetic reconnection (which is discussed in detail in section 2.4.4), in structures such as solar flares, can create huge plasmoids which are no longer tied to the Sun's magnetic field and are accelerated into interplanetary space. These interplanetary CMEs, known as ICMEs, can travel through the interplanetary space at speeds of 600 km/s carrying billions of tonnes of plasma with them (*Iju et al.*, 2013).

The solar wind flows out from the Sun in an approximately radial direction, however, as the Sun rotates (with a period of $\sim$ 25 days) the solar wind source region rotates along with it. This rotation of the source region causes sequential "parcels" of solar wind to flow out radially in a slightly different angular direction (as is demonstrated in Figure 2.4).

The magnetic field is embedded within the solar wind (as discussed in section 2.3.2) but is also anchored into the solar wind source region. As the source region rotates and the parcels flow radially away from Sun, the magnetic field is is forced into a spiral

configuration, linking these individual parcels to the source region on the Sun. This spiral formation, first envisaged in *Parker* (1958), is known as the Parker Spiral.

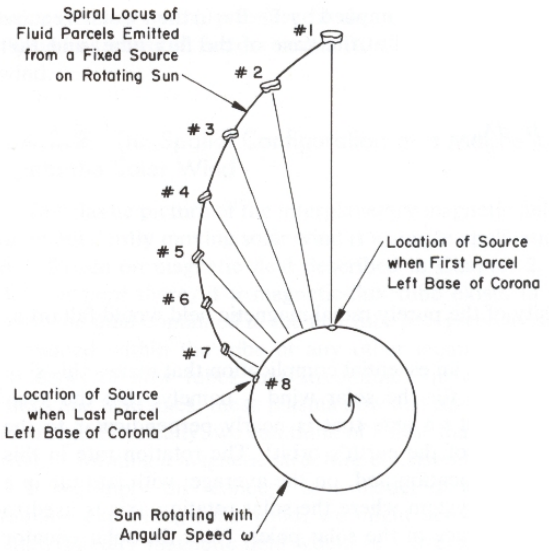

FIGURE 2.4: A schematic diagram illustrating how the rotation of the solar wind source region creates a Parker Spiral. The magnetic field is embedded into the solar wind whilst also being anchored into the source region and so is twisted into a spiral configuration (*Kivelson and Russell*, 1995).

Due to the Sun's rotation creating the Parker Spiral, flows of different speeds can become aligned and fast streams are able to "catch up" with slow streams. Co-rotating interaction regions are formed as the fast solar wind is compressed behind slow solar wind, as shown in Figure 2.5.

2.3.2 Frozen-in Flux

The Sun's magnetic field extends into interplanetary space where it is known as the interplanetary magnetic field. Understanding how this IMF behaves starts with the ideal magnetohydrodynamics (MHD) approximation of Ohm's Law:

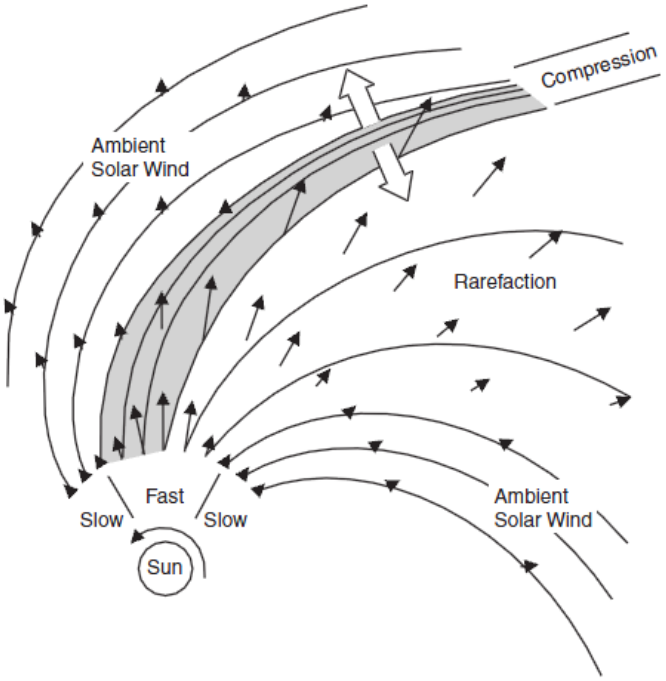

FIGURE 2.5: A schematic diagram of the slow and high speed stream interactions. The solar wind plasma is compressed where the streamlines converge. (*Pizzo*, 1978).

$$\mathbf{E} + \mathbf{u} \times \mathbf{B} = 0 \tag{2.50}$$

Using the ideal MHD approximation allows for the simplification of the core MHD equations by neglecting certain terms. The assumptions made in the ideal case, such as assuming there is charge quasi-neutrality throughout the plasma and that the electric field time derivative is zero, are valid when describing the solar wind.

Using equation 2.50, it can be shown that the magnetic flux is conserved along the plasma flow lines. To describe how the flux is tied into the plasma flow, equation 2.50 is combined with Faraday's Law:

$$\nabla \times \mathbf{E} = -\frac{\partial \mathbf{B}}{\partial t} \tag{2.51}$$

to give the magnetic induction equation:

$$\frac{\partial \mathbf{B}}{\partial t} = \nabla \times (\mathbf{u} \times \mathbf{B}) \tag{2.52}$$

If equation 2.52 is expressed in a coordinate system which is rotating with the Sun (at speed $\omega_\odot$) and if differential rotation is ignored, then it becomes (see *Gombosi* (1998) for derivation):

$$\frac{\partial \mathbf{B}}{\partial t} + [(\omega_\odot \times \mathbf{r}) \cdot \nabla] = \nabla \times (\mathbf{u} \times \mathbf{B}) \tag{2.53}$$

The left hand side of equation 2.53 is the total convective derivative of the magnetic field in the co-rotating system - which vanishes if we assume a steady-state axially symmetric situation and thus equation 2.53 simplifies to:

$$\nabla \times (\mathbf{u} \times \mathbf{B}) = 0 \tag{2.54}$$

Since the curl of $\mathbf{u} \times \mathbf{B}$ is zero, a scalar potential exists which is equal to $\mathbf{u} \times \mathbf{B}$ and, using the ideal MHD version of Ohm's Law (equation 2.50), this scalar potential must represent the electric field. The scalar product of the scalar potential with both the plasma flow and magnetic field is also zero, which demonstrates that $\mathbf{u}$ and $\mathbf{B}$ are equipotentials.

The result of this is that, with certain assumptions in place, the magnetic field and plasma flow vectors are always parallel in a frame of reference rotating with the Sun i.e.

$$\mathbf{u} \times \mathbf{B} = 0 \therefore \mathbf{u} \,||\, \mathbf{B}. \tag{2.55}$$

This property, that the magnetic field lines move with the plasma, is known as the Alfvén frozen-flux theorem or the "frozen in theorem". A consequence of the frozen in theorem is that the magnetic field lines follow a Parker spiral configuration just as the solar wind plasma does.

The IMF can be orientated in any direction when it arrives at Earth. Its orientation is an important factor in the coupling between the solar wind and the magnetosphere, primarily due to magnetic reconnection (see section 2.4.4). Southward IMF, where the IMF is aligned with the negative z-axis in the geocentric solar ecliptic (GSE) reference frame, will more strongly reconnect with the dayside magnetosphere and allow for the transport of solar wind particles and energy into the magnetospheric system.

2.4 The Magnetosphere

Due to the huge amounts of molten iron in the Earth's outer core acting as a geodynamo, the Earth has its own geomagnetic field. If the Earth were positioned in an isolated system, free of any outside magnetic interference, the configuration of its magnetic field would be approximated by a magnetic dipole field (see Figure 2.6).

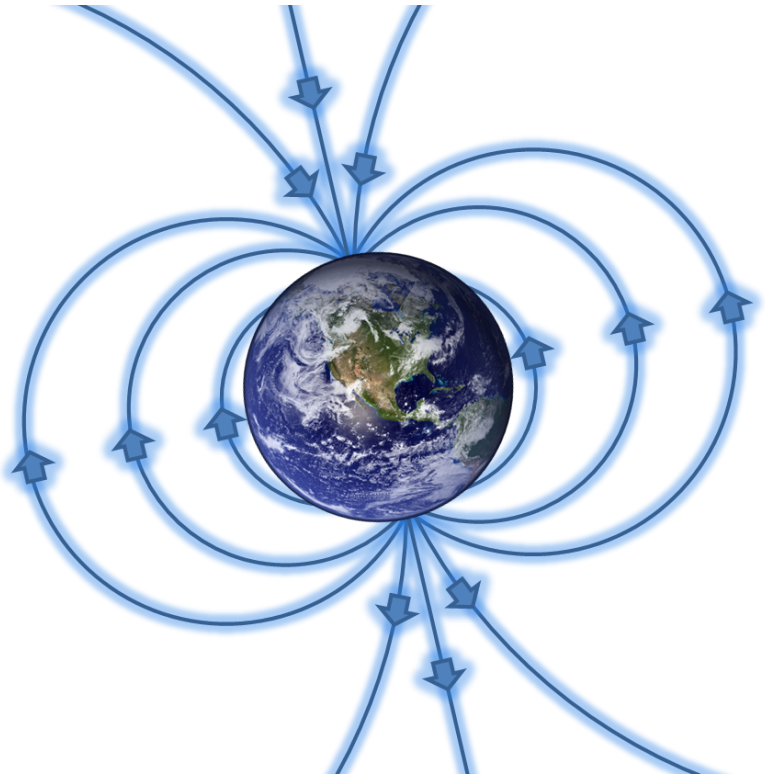

FIGURE 2.6: A schematic diagram depicting a tilted magnetic dipole field - which would be a good approximation of the Earth's magnetic field in an isolated system.

The Earth's magnetic axis is not fixed; the North and South poles "wander" independently and by a varying amount. However, as a general approximation, the magnetic axis is tilted by $\sim 11^{\circ}$ from the rotational spin axis. When working with magnetospheric spacecraft it is often useful to know their location with respect to the Earth's magnetic frame, rather than the Earth's rotational frame, and so the Geocentric Solar Magnetospheric (GSM) co-ordinate system was developed. This cartesian co-ordinate system has its X axis directed toward the Sun (the axis is known as the Sun-Earth line) and its Z axis is the projection of the Earth's magnetic dipole axis (positive North) on to the plane perpendicular to the X axis. The difference between the GSM system and the GSE system (where the Y axis points along the ecliptic plane towards dusk) is simply a rotation about the X-axis.

Due to interactions with the magnetised solar wind, the dipole approximation is only valid for a couple of R_E from the Earth's surface. At distances further than this, complex interactions between the IMF and the terrestrial magnetic field create structures not found in a dipole field.

The terrestrial magnetosphere is defined as the region of space in which electrically charged particles are influenced by the Earth's magnetic field. Its size is variable, depending upon the impinging solar wind conditions, and its shape is distorted from the dipole approximation. There are multiple large-scale structures within the Earth's magnetosphere, as shown in Figure 2.7, some of which will now be discussed.

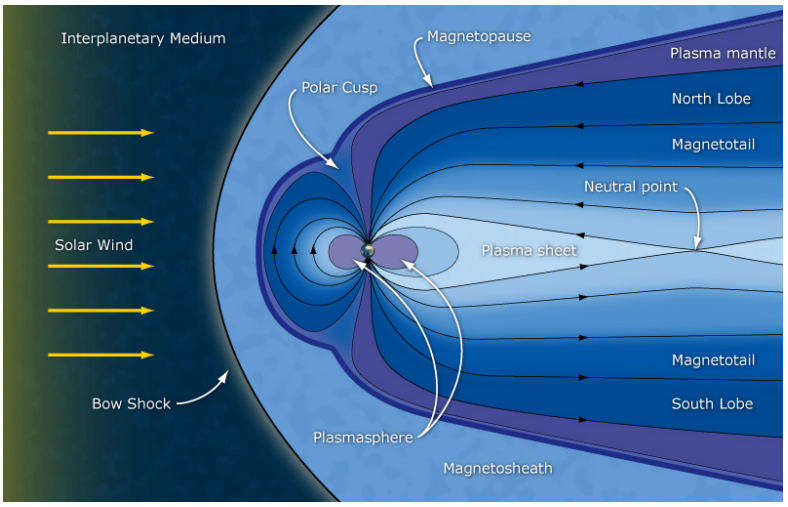

FIGURE 2.7: An illustration of the Earth's magnetosphere - the region of space dominated by the Earth's magnetic field but constrained by the impinging solar wind and IMF. (Image credit:ESA/C. T. Russell)

2.4.1 The Bow Shock

Since the solar wind is a magnetised, supersonic and superalfvénic plasma flow, a standing shock wave is formed when it encounters a magnetised obstacle such as the Earth. This standing shock wave is known as the bow shock. The solar wind cannot pass

through the Earth's magnetic field, due to the embedded IMF, and thus the shock wave is necessary to slow down the solar wind so that its flow can be diverted around the terrestrial magnetic field.

The size, shape and location of the bow shock are not constant and are affected by changes in the solar wind. In the often used bow shock model of *Farris and Russell* (1994), the location is governed by the size and shape of the magnetised obstacle (the Earth), the solar wind dynamic pressure, the orientation of the IMF with respect to the shock normal and the upstream Mach number. *Farris and Russell* (1994) provides the following equation to describe D_{BS}, the distance to the bow shock from the center of the magnetised obstacle:

$$D_{BS} = R_C \left[\frac{D_{OB}}{R_C} + 0.8 \frac{(\gamma - 1){M_1}^2 + 2}{(\gamma - 1)({M_1}^2 - 1)} \right] \tag{2.56}$$

where M_1 is the upstream (solar wind) Mach number and γ is the ratio of the specific heats. Additionally, D_{OB} is the standoff distance of the obstacle from the obstacle's center and R_C is the radius of the curvature of the obstacle, the definition of which is:

$$R_C = \frac{\kappa}{1 + \epsilon \cos\theta} \sqrt{\frac{A\,(\epsilon,\theta)}{B\,(\epsilon,\theta)}} \tag{2.57}$$

where κ and ϵ describe the size and shape of the curvature and θ describes the location on the curve. The terms A and B are multi-order trigonometrical functions which depend upon both ϵ and θ (*Farris and Russell*, 1994). At the nose of a conical revolution (such

as the bowshock) the radius of the curvature is equal to the semilatus rectum (κ) and at $\theta = 90^\circ$ the radius of the curvature is equal to:

$$R_C = \kappa \left[1 + \epsilon^2\right]^{\frac{3}{2}} \tag{2.58}$$

The shape of the dayside ($X_{GSE} \geq 0$) bow shock is fairly elliptical, but with an extended tail region on the nightside ($X_{GSE} < 0$). The average distance to the bow shock "nose" (the most sunward tip of the bowshock) is approximately $15R_E$ whilst the average distance to the bow shock in the dusk/dawn meridians is approximately $25R_E$ (though there is some dawn/dusk asymmetry) (*Fairfield*, 1971).

2.4.2 Magnetopause

Since the solar wind is supersonic, it passes through the bow shock where it is then slowed. This "shocked" plasma is diverted around the magnetosphere due to the frozen in magnetic field (see section 2.3.2) not allowing it pass through the Earth's magnetic field. The zone in which this shocked plasma resides is known as the magnetosheath. The plasma in the magnetosheath is much denser, hotter and slower than the solar wind.

The dayside magnetopause, in a first order approximation, can be considered as a tangential discontinuity which separates the shocked solar wind in the magnetosheath from the magnetospheric region. The thickness of this discontinuity can vary from around 400 to 700 km (*Berchem and Russell*, 1982).

It is important to note that a first order approximation requires that there is no plasma transport across the discontinuity (e.g. from the shocked solar wind to the magnetosphere) and that the normal magnetic field component is zero. The tangential magnetic field component, the density and the pressure can all be discontinuous (*Gombosi*, 1998).

The location of the magnetopause, as with the bowshock, is dependant upon the impinging solar wind conditions. It is located where the total pressure (magnetic and thermal) of the magnetosheath (subscript *sh*) is balanced by the total pressure of the magnetosphere (subscript *sp*) e.g.:

$$p_{sh} + \frac{\mathbf{B}^2{}_{sh}}{2\mu_0} = p_{sp} + \frac{\mathbf{B}^2{}_{sp}}{2\mu_0} \tag{2.59}$$

Inside the magnetopause, particularly in the nose region, the total pressure is dominated by the Earth's magnetic field and so the thermal pressure contribution can be neglected. Outside the magnetopause, the total pressure is still a combination of the thermal and magnetic pressures. However, in a first order approximation, the contribution from the shocked solar wind tangential magnetic field component can be neglected thus the pressure balance equation becomes:

$$\rho_{sh} {u_{sh}}^2 = K \frac{{\mathbf{B}_e}^2}{\mu_0} \left(\frac{R_E}{R_{mp}} \right)^6 \tag{2.60}$$

where u_{sh} is the speed of the shocked solar wind in the magnetosheath in the normal direction, K is the magnetic field compression factor (~ 2), $\mathbf{B}_e$ is the equatorial magnetic

field at the Earth's surface and R_{mp} is the magnetopause stand off distance (*Gombosi*, 1998).

Rearranging equation 2.60, for average solar wind conditions, gives $R_{mp} \approx 10\ R_E$. According to *Fairfield* (1971), the average distance to the magnetopause in the ecliptic plane is 11.0 R_E and $\sim$ 15.5 R_E in the meridional directions. There are many models, which aim to predict the location of the magnetopause in three dimensions, in use throughout the scientific literature (see *Case and Wild* (2013) for a list of examples). These are normally best fit results based upon satellite measurements.

2.4.3 Polar Cusps

In both the northern and southern hemispheres exist regions of null magnetic field known as the polar cusps. These funnel-shaped regions lie between the first/last sunward and tailward connected magnetic field lines (see Figure 2.7). The exact location of the polar cusps is dependent upon the impinging solar wind conditions (especially IMF direction and dynamic pressure) but generally lies somewhere between 70° and 86° in invariant latitude (*Zhou et al.*, 2000). Their existence was predicted in the *Chapman and Ferraro* (1931) model magnetosphere and were first observed through in-situ data from the ISIS 2 mission in 1971 (*Heikkila and Winningham*, 1971).

These cusp regions are one of the main routes for solar wind plasma to enter into the Earth's magnetosphere and therefore contain both magnetosheath plasma and magnetospheric plasma. The magnetospheric plasma is a mixed distribution since the magnetic field lines in the cusps connect to all regions of the magnetosphere. The region has a

complex structure and magnetic topology which is not very well understood. It has a large spatial extent and is highly dynamic (*Shen et al.*, 2011).

Nykyri et al. (2012) showed that magnetosheath particles are accelerated locally, in the polar cusp region, as they drift along the potential gradients created by magnetic reconnection. A fraction of these accelerated particles can then enter the magnetosphere: along the dawn flank for ions and along the dusk flank for electrons (*Fritz et al.*, 2012). The cusps play an important role in the connection between the magnetosheath and the magnetosphere.

2.4.4 Magnetic Reconnection

Magnetic reconnection is a fundamental process which violates the concept of frozen-in flow. To understand magnetic reconnection, and the reason why the frozen-in flux theorem breaks down, it is intuitive to start with the induction equation:

$$\frac{\partial \mathbf{B}}{\partial t} = \nabla \times (\mathbf{u} \times \mathbf{B}) + \eta \nabla^2 \mathbf{B} \tag{2.61}$$

This form (as opposed to that given in equation 2.52) includes not only the magnetic field convection term but also a diffusion term (where η is the magnetic viscosity ($\eta = \frac{1}{\sigma \mu_0}$)). In cases where the the transport time of the MHD fluid is much shorter than the diffusion time for the magnetic field, such as in the solar wind, we find through dimensional analysis that:

$$\mu_0 \sigma u L \gg 1 \tag{2.62}$$

where L is the typical scale length of the flow (of speed u). This leads to the definition of the magnetic Reynolds number, R_m:

$$R_m \simeq \frac{1}{\eta} uL \tag{2.63}$$

which again is generally a very large number in ideal MHD fluids such as the solar wind.

A direct consequence of the frozen-in theorem is that when two different plasma regimes meet (such as the magnetosheath and magnetosphere), a boundary layer must be formed between them (e.g. the magnetopause). This is because plasma can only flow along field lines (not across them) and so the two distinct plasma regimes cannot mix. The magnetic field topology on either side of the boundary layer can be completely different, with differing field direction and strength, but, close to the boundary, the fields will be antiparallel and tangential to the boundary.

In the boundary layer, where the scale length (L) is small, the plasma becomes quite stagnant and so the diffusive term of the induction equation dominates. In this case, i.e. where there is no plasma flow, the induction equation is simplified to:

$$\frac{\partial \mathbf{B}}{\partial t} = \eta \nabla^2 \mathbf{B} \tag{2.64}$$

and the magnetic Reynolds number approaches unity.

In the one-dimensional case, where the magnetic field is assumed to be in the z-direction and x is the direction normal to the boundary, equation 2.64 can be simplified further:

$$\frac{\partial \mathbf{B}_z}{\partial t} = \eta \frac{\partial^2 \mathbf{B}_z}{\partial x^2} \tag{2.65}$$

The solution of equation 2.65, at time t, takes the form of an error function:

$$\mathbf{B}_z(x,t) = -\mathbf{B}_0 \mathrm{erf}\left(\frac{x}{2\sqrt{\eta t}}\right) \tag{2.66}$$

where:

$$\mathrm{erf}(u) = \frac{2}{\sqrt{\pi}} \int_0^u e^{-x^2}\, \mathrm{d}x. \tag{2.67}$$

Equation 2.66 shows that, over time, the magnetic field dissipates from the magnetic discontinuity and so the discontinuity itself will "erode". The result of this decay is shown in Figure 2.8.

It is important to note that although the magnetic flux is conserved, the magnetic energy density decreases with time. Magnetic flux is conserved through diffusion along the field gradients but the magnetic energy is converted into heat through Joule heating and is transferred to the surrounding plasma.

The idea that magnetic fields are annihilated is a little too simplified - due to looking at the problem in one dimension only. Instead of the magnetic field annihilating at some neutral point, it in fact is zero over a single line which intersects the plane of the magnetic field (known as an x-type neutral line). Using Faraday's Law:

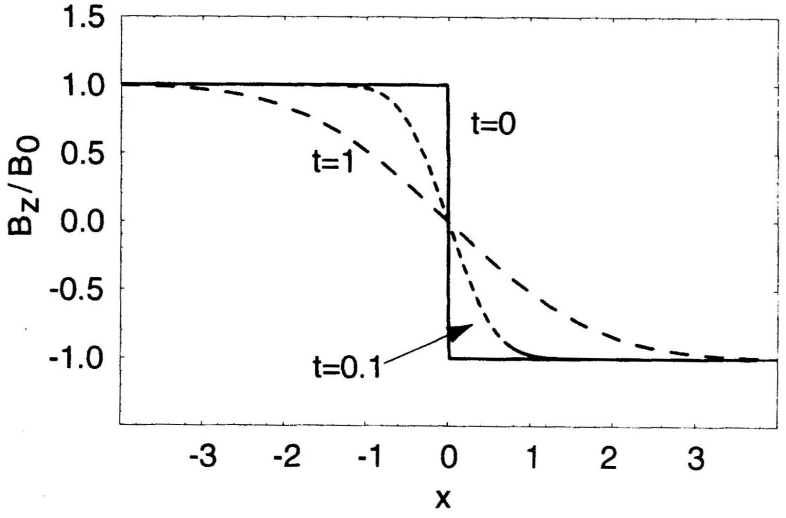

FIGURE 2.8: Schematic representation of the time evolution of erosion of a magnetic discontinuity during magnetic reconnection (*Gombosi*, 1998).

$$\nabla \times \mathbf{E} = \frac{\partial \mathbf{B}}{\partial t} = 0 \tag{2.68}$$

which in the x-component reduces to:

$$\frac{\partial \mathbf{E_y}}{\partial z} = 0 \tag{2.69}$$

we find that a uniform electric field is formed. This electric field causes inflow into the diffusion region (a region where $R_m < 1$) from the "top" and "bottom" of the system and outflow through the "sides". So now, rather than being annihilated, the field lines "snap" as they enter into the diffusion region. They then "reconnect" with the snapped field lines entering from the opposite direction and leave the diffusion region through the sides. This configuration is shown in Figure 2.9.

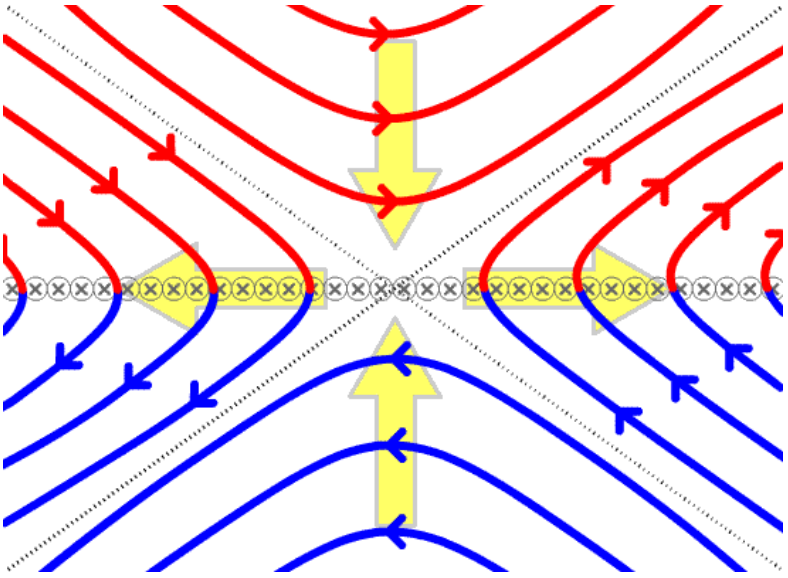

FIGURE 2.9: Schematic representation of x-type magnetic field reconnection. Field lines are driven into the diffusion region from the top and bottom by a uniform E_y field where they then snap. They reconnect with the opposite incoming snapped field lines and leave the diffusion region through the sides.

The primary consequence of this reconnection process is that plasma, sourced from two different regimes, is now able to mix (which is a complete violation of the frozen-in theorem). The two plasma populations, which were originally on separate and isolated flux tubes, are now on the same flux tube and can mix with ease. Additionally, even though only relatively small regions of the original flux tubes were involved in the reconnection process, the entire flux tube is now reconnected to a completely different plasma region.

2.5 Solar Wind-Magnetosphere-Ionosphere Coupling

As discussed in the previous sections, the solar wind is a plasma outflow which constantly bombards the near-Earth system. Protecting the Earth from this bombardment is the terrestrial magnetic field which, due to the frozen-in flux theorem, acts as a shield preventing the plasma from stripping away the Earth's atmosphere.

However, the frozen-in flux theorem can, and does, break down. In cases where the magnetic Reynold's number approaches unity, such as at the boundary between the magnetosheath and the magnetosphere, the frozen-in flux theorem no longer holds and magnetic reconnection takes place. Magnetic reconnection couples field lines from the IMF to the terrestrial magnetic field and allows solar wind particles, who would not normally be able to cross magnetic field lines, to enter into the near-Earth environment.

Reconnection at the dayside magnetosphere causes open magnetic field lines, anchored at the Earth's pole, to stretch out into interplanetary space. The solar wind flow "drags" these open field lines anti-sunward towards the magnetotail region of the magnetosphere. In this region open field lines reconnect with those from the opposite pole to form a new geomagnetic field line and a new interplanetary field line. The geomagnetic field line travels earthward whilst the interplanetary field line flows off into interplanetary space. This process, though the description here has been extremely simplified, is known as the Dungey cycle (see Figure 2.10) and was first proposed by *Dungey* (1961).

The Dungey cycle is one example of how the magnetosphere, and plasma flows within it, is coupled to the solar wind.

In addition to creating plasma flow, reconnection at the magnetopause causes an influx of solar wind particles to populate the terrestrial magnetic field lines. This increase in charged particles enhances magnetospheric currents, such as the ring current, and can modify the magnetic field strength on the Earth's surface. Additionally, some of these charged particles are lost into the upper atmosphere (known as the ionosphere) and can form, for example, auroral displays.

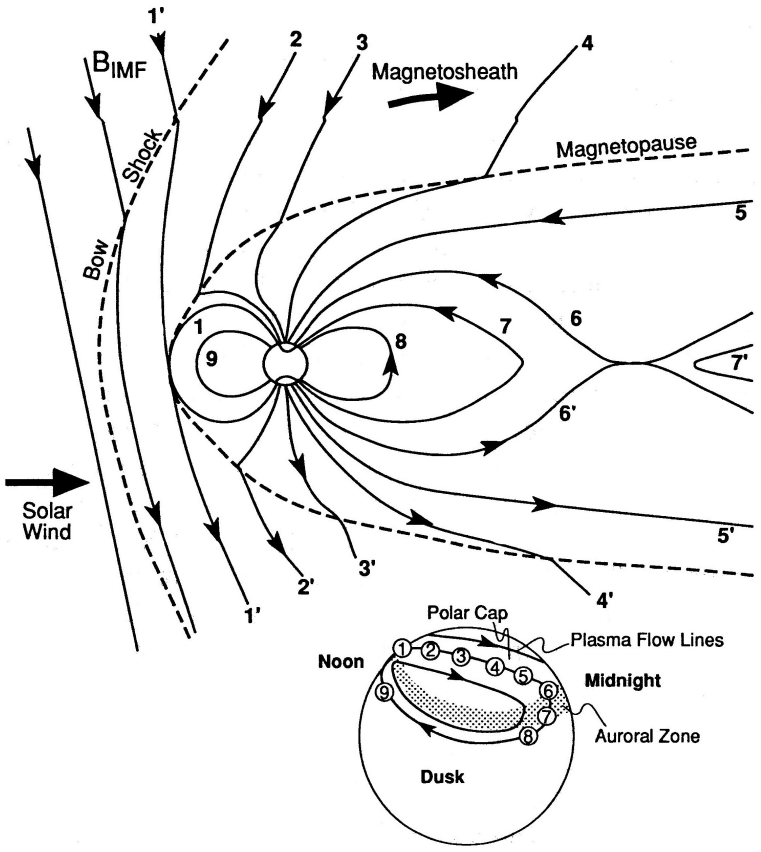

FIGURE 2.10: The schematic figure demonstrates plasma flow through the magnetosphere driven by magnetic reconnection. The numbered field lines show the evolution of a field line involved in the Dungey cycle. Dayside reconnection occurs at the front on the magnetosphere. Reconnection then re-occurs in the magnetotail at point 6. (*Kivelson and Russell*, 1995)

Magnetic reconnection is a very important factor when discussing solar wind-magnetosphere-ionosphere coupling. Both it and many other magnetospheric processes depend upon the impinging solar wind conditions. To be able to accurately understand these processes and predict when they might occur requires a knowledge of the solar wind and IMF conditions in our near-Earth environment. The work presented in this thesis is part of the effort to provide better specification of the IMF at Earth.

Chapter 3

Instrumentation

The research presented in the chapters that follow has utilised data from several sources. These data are provided by two spacecraft missions (ESA's Cluster mission and NASA's ACE mission) and one multi-spacecraft database (NASA's OMNIweb). In this chapter an introduction to these data sources, and the instruments used in the collection of the data, is provided.

3.1 Fluxgate Magnetometer

A fluxgate magnetometer (FGM) is the most common instrument used to measure magnetic fields since it is relatively simple to build and is accurate and reliable. An FGM sensor is comprised of a highly magnetically permeable alloy ring (or core) around which are wrapped two electrically conductive coils (one primary/drive coil and one secondary/sense coil).

Some known, varying, current is applied to the drive coil which generates a magnetic field in the core. Any background level of magnetic field (which is the field level the magnetometer is designed to measure) will contribute to the total field of the core. The changing magnetic field in the core then induces a voltage through the sense coil.

However, to accurately determine the strength and direction of the external magnetic field it is not enough to measure the voltage alone. Instead the magnetometer uses an effect known as hysteresis to describe the magnetic saturation of the core (where the magnetic field of the core is no longer able to increase with the applied magnetic field).

The current through the drive coil is increased to such a level that it creates magnetic saturation in the core. Since an induced voltage only occurs when the magnetic field is changing, as the core reaches magnetic saturation the voltage across the sense coil is lost. In the case of no external magnetic field, the output voltage is in-step with both half-cycles of the input current - as shown in Figure 3.1.

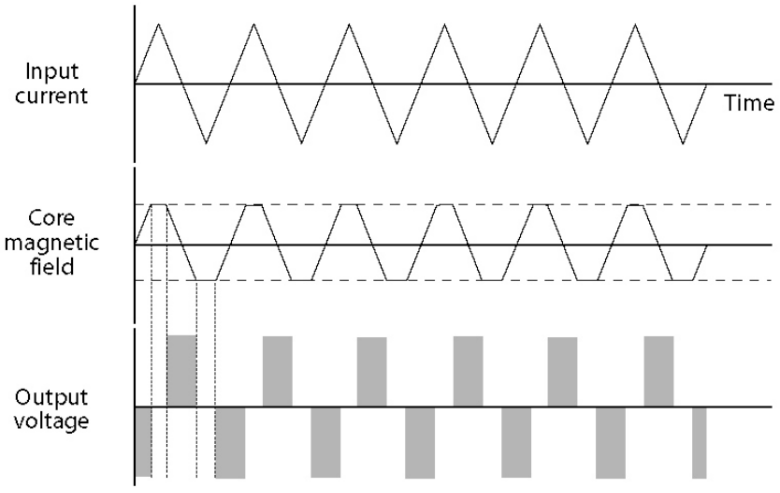

FIGURE 3.1: In the absense of an external field, the output voltage across the sense coil is in-step with the input current across the drive coil for both half-cycles (*Wild*, 2000).

However, in the presence of an external magnetic field the core reaches saturation in one

of the half-cycles faster than in the other (depending upon the direction of the field) and thus the output voltage is no longer in-step with the input current for both half-cycles - as shown in Figure 3.2.

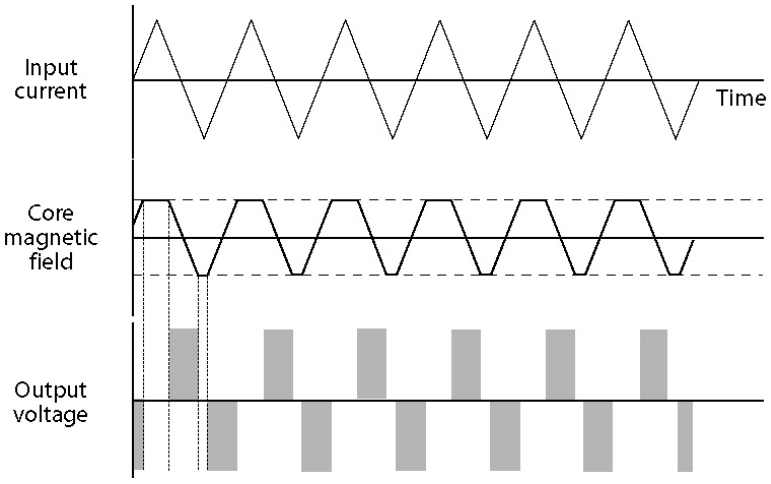

FIGURE 3.2: In the presence of an external field, the output voltage across the sense coil is no longer in-step with the input current across the drive coil for both half-cycles (*Wild*, 2000).

It is then both the size and phase of the induced voltage spikes which provides the magnitude and direction of the external magnetic field. In order to provide a three-dimensional measurement of the magnetic field, three orthogonal coils must be used - this is often known as a three-axis or tri-axial fluxgate magnetometer.

3.2 Electrostatic Analyser

There are several different types of charged particle detectors in use in spacecraft missions, though the basic principles governing them are generally the same. In this section, the electrostatic analyser is discussed.

In the presence of an electric field, for example between two parallel charged plates, an electrically charged particle will experience an electric force (the Lorentz force). Basic

Newtonian physics states that this force will create an acceleration on the particle and that this acceleration is dependent upon its mass and charge. Particles that are highly charged or are low in mass are accelerated more than heavier, lowly charged particles and so, in the case of moving particles, experience a larger deflection.

If instead of two parallel plates, an electric field is created between to spherical shells then the charged particles are continually accelerated toward the center of the shells i.e. they experience circular motion. The radius of the particle's circular path is dependent upon the particle's initial velocity, mass and charge. If the path radius of the particle is greater than the radius of the outer shell then the particle will collide with the outer shell and if the path radius is less than the radius of the inner shell then the particle will collide with the inner shell.

For a single species, such as electrons, the mass and charge of the particles are well known. Since the radius the two circular shells is also known, by sweeping through different electric field strengths over time it is possible to determine the number of electrons with a specific energy (i.e. the energy required to have a radius whose path fits between the two shells). This set up is schematically shown in Figure 3.3.

3.3 The Cluster Mission

Along with the Solar Heliospheric Observatory (SOHO) mission, the Cluster Mission formed part of ESA's first cornerstone programme: the Solar Terrestrial Science Programme. The four-spacecraft Cluster mission was proposed in November 1982 and, after an initial failed launch in June 1996 in which all four spacecraft were destroyed, the

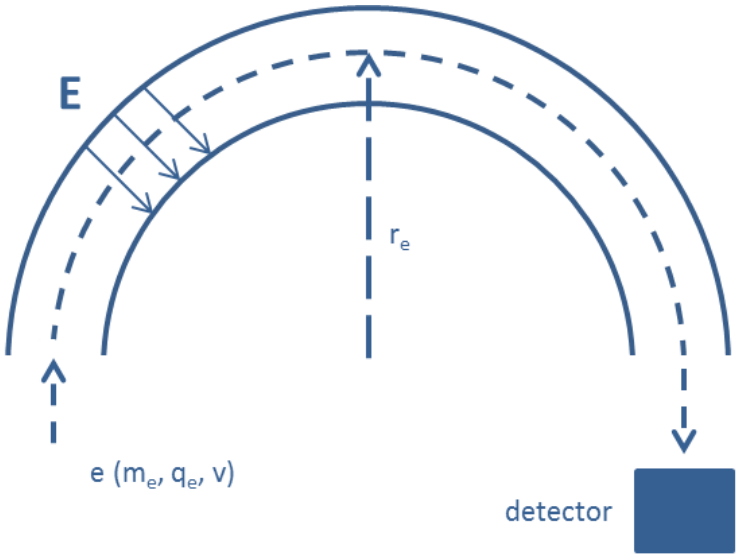

FIGURE 3.3: A schematic diagram of an electrostatic analyser. By varying the electric field (E) only electrons with a certain energy (velocity) will make it through the analyser to the detector.

mission's spacecraft were rebuilt and successfully launched in summer 2000 (*Credland et al.*, 1997; *Escoubet et al.*, 1997).

Initially the Cluster spacecraft were placed into a geostationary transfer orbit and then, after a series of manoeuvres was undertaken for each spacecraft, they were placed into their final 57 hour polar orbit about the Earth - with a perigee of 4 R_E (26,000 km) and an apogee of 19.6 R_E (125,000 km) (*Escoubet et al.*, 1997).

Since the mission's orbit is essentially fixed in inertial space, the apogee location changes throughout the year as the Earth orbits the Sun. During the months of November to June, the apogee of the mission's orbit crosses through the magnetopause region of the magnetosphere and out into the unimpeded solar wind (known as the "dayside region") whilst during the months of July to October, the spacecraft predominantly reside in the magnetotail region of the magnetosphere (know as the "nightside region").

After months of calibrations and optimisations the mission was declared operational on 1st February 2001 (*Escoubet et al.*, 2001). Though the mission was expected to end in December 2005, it has since been extended several times and remains almost fully operational to this date.

3.3.1 Scientific Objectives

The Cluster mission was designed to study the small-scale structures and macroscopic turbulence that arise in many regions of the magnetosphere in three dimensions (*Escoubet et al.*, 2001). The primary regions of interest are:

- the solar wind and bow shock,

- the magnetopause,

- the polar cusps,

- the magnetotail and

- the auroral zones.

Over the mission's lifetime, the orbital configuration of the Cluster spacecraft has evolved to allow it to pass into all of the regions noted above. The spacecraft orbit the Earth in a varyingly-shaped tetrahedral configuration and this tetrahedral shape has enabled investigations on small- and medium-scale magnetospheric structures, of sizes ranging from about 100 km to 23 R_E. This is due to the simultaneous multi-point measurements taken at each spacecraft. Such investigation had previously been impossible since most

magnetospheric missions contained only one, or occasionally two, spacecraft in the region of interest (*Escoubet et al.*, 1997).

Orbital dynamics mean that the tetrahedral constellation cannot be maintained throughout the whole orbit and so the constellation is optimised depending upon what region of space is of interest. For example, in February 2001, when Cluster crossed the polar cusps, the tetrahedron was optimised to be perfectly situated over the northern and southern cusps whilst in August 2001, when the Cluster orbit intersected the magnetotail, the perfect tetrahedron moved to the neutral sheet near apogee (*Escoubet et al.*, 2001).

3.3.2 Instrumentation

Each Cluster spacecraft is identical, with a suite of eleven instruments on-board each measuring a range of different parameters. The instruments on-board the Cluster spacecraft, along with their Principle Investigators (at launch), are listed in Table 3.1.

For the research undertaken in this thesis, the two instruments from which data are exploited are FGM and CIS.

There are two three-axis FGM sensors (see section 3.1) located on each spacecraft. To reduce electromagnetic interference from the main spacecraft electronics, the sensors are located 3.7 m along (inboard) and at the end of the 5.2 m spacecraft boom (outboard). Whilst either sensor can be designated as the primary sensor, the outboard sensor has been designated as such on all four spacecraft since launch (*Gloag et al.*, 2010).

TABLE 3.1: Instruments on-board the Cluster spacecraft (*Escoubet et al.*, 2001)

Acronym	Instrument	Principle Investigator
ASPOC	Active Spacecraft Potential Control	K. Torkar (IRF, Austria)
CIS	Cluster Ion Spectrometry	H. Rème (CESR, France)
DWP	Digital Wave Processing experiment	H. Alleyne (Sheffield, UK)
EDI	Electron Drift Instrument	G. Paschmann (MPE, Germany)
EFW	Electric Field and Wave experiment	M. André (IRFU, Sweden)
FGM	Fluxgate Magnetometer	A. Balogh (IC, UK)
PEACE	Plasma Electron And Current Experiment	A. Fazakerley (MSSL, U.K.)
RAPID	Research with Adaptive Particle Imaging Detectors	P. Daly (MPA, Germany)
STAFF	Spatio-Temporal Analysis of Field Fluctuation experiment	N. Cornilleau-Wehrlin (CETP, France)
WBD	Wide Band Data	D. A. Gurnett (Iowa U., U.S.A.)
WHISPER	Waves of High Frequency and Sounder for Probing of Electron density by Relaxation	P. M. E. Décréau (LPCE, France)

The FGM instruments measure the magnetic field in the near spacecraft environment and have eight magnetic field ranges, though only five are used in the Cluster magnetometers (see Table 3.2), and different sampling rates. The instrument data processing units (DPU) automatically switch between the different ranges, or can be specifically instructed to do so, as and when required, by mission control.

TABLE 3.2: FGM operating ranges (from *Balogh et al.* (1997)).

Range Number	Range (nT)	Resolution (nT)
2	-64 to $+63.97$	7.8×10^{-3}
3	-256 to $+255.87$	3.1×10^{-2}
4	-1204 to $+1023.5$	0.125
5	-4906 to $+4904$	0.5
7	-65536 to $+65504$	8

These operating ranges were selected to provide good resolution in the solar wind (the magnetic field magnitude is generally between 3 nT and 30 nT) and up to the

highest magnetic field magnitudes Cluster was expected to encounter during its orbit (∼1000 nT). The highest range (range 7) was only used for ground testing (*Balogh et al.*, 1997).

The magnetic field components are constantly measured at a frequency of 201.75 Hz, however, there is insufficient bandwidth to allow transmission of data at such high temporal resolution. The data are therefore digitally filtered by the DPU to match the allowed telemetry data rate, which is determined by the spacecraft's telemetry mode. In normal operation (nominal mode) the magnetometer's primary sensor has a transmission rate of 15.5 vectors per second. There are other telemetry modes, known as burst modes, which allow higher transmission rates if required.

The Cluster FGM data used in this thesis are obtained from the Cluster Active Archive (CAA). The CAA is a repository of of pre-processed and validated Cluster data as well as a source for other useful information such as calibration data and instrument documentation (see *Laakso et al.* (2010)). The primary FGM data products in the CAA are calibrated and validated magnetic field data, given in the GSE co-ordinate system, at three different time resolutions: no averaging (∼22 Hz), averaged to five vectors per second and averaged over one spacecraft spin (∼four seconds).

In Chapters 4 and 6, the Cluster FGM data are used to determine the orientation of the IMF in the near Earth region of space (at the bowshock and magnetopause respectively). In Chapter 5, the data are used in a magnetopause crossing detection routine to determine the location of the Earth's magnetopause.

The CIS experiment was designed primarily to study the dynamics of magnetised plasma,

in the near Earth region of space. To achieve this, CIS is able to measure the full three-dimensional ion distribution of the major magnetospheric ions over a range of energies. The experiment is composed of two instruments, a Composition and Distribution Function analyser (CIS1/CODIF) and a Hot Ion Analyser (CIS2/HIA), which allows the experiment to record both mass per charge composition (CIS1) and high angular resolution for ion beam and solar wind measurements (CIS2) (*Rème et al.*, 2001).

The CODIF instrument measures the complete 3D distribution functions of the major ion species (H^+, He^+, He^{++} and O^+) at spacecraft spin resolution. It consists of a toroidal energy-per-charge (E/q) analyzer with a 360 degree disk-shaped field of view (FOV), and a $\geq$15 keV/e post-acceleration into a time-of-flight (TOF) analysis section.

Whilst the primary sensor covers ion energies between 0.02 and 32 keV/charge, an additional Retarding Potential Analyser (RPA) component extends the range of energies to as low as the spacecraft potential (essentially zero). As such, CODIF is able to cover the complete energy range of plasma distributions which may be of interest during the Cluster mission.

Since CODIF operates in two very different plasma regions (e.g. high density magnetosheath and low density magnetotail), it is necessary that it can operate at two different sensitivities. As such, CODIF has two 180 degree sections which are set at different sensitivities (by a factor of 100) which enables the instrument to provide statistically meaningful count rates whilst also keeping the count rates at an acceptable level for the on-board electronics. The only exception to this is solar wind H^+ ions which often saturate even the lower sensitivity section.

The HIA is a symmetrical quadrispherical electrostatic analyser (see Section 3.2) which has a uniform 360 degree disc-shaped FOV. Particles enter the analyser and are deflected by 90 degrees (hence the quadrispherical). They then pass through the analyser where a charge is applied between two plates. This potential only allows charged particles with a limited range of energy and initial azimuth angle to be transmitted to the focussing plane. The deflected ions are then detected in the focussing plane using two micro channel plates and several anodes (*Rème et al.*, 2001).

The CIS data are used in Chapter 4 to check plasma temperatures as a way of determining whether the Cluster satellites are inside the magnetosheath or out in the unimpeded solar wind. As with the FGM data, for the research presented in this thesis, CIS data is obtained from CAA.

3.4 The ACE Mission

NASA's Advanced Composition Explorer (ACE) spacecraft mission was proposed in 1986 as a part of the Explorer Concept Study Program and was launched in August 1997. ACE is an upstream solar wind observer, designed to continuously monitor the earthward-bound solar wind, and so was placed into a Lissajous orbit (a non-periodic Halo orbit) about the Sun-Earth Lagrangian point 1 (L1).

Lagrangian points are regions of equilibrium between the gravitational potential fields of large orbiting masses. In the restricted three bodied problem, where one large body of mass (such as the Earth) orbits another (the Sun) and a third "massless" body (a

spacecraft) interacts with both, there are five such Lagrangian points (*Koon et al.*, 2008). A schematic diagram of the locations of the Langrange points is given in Figure 3.4.

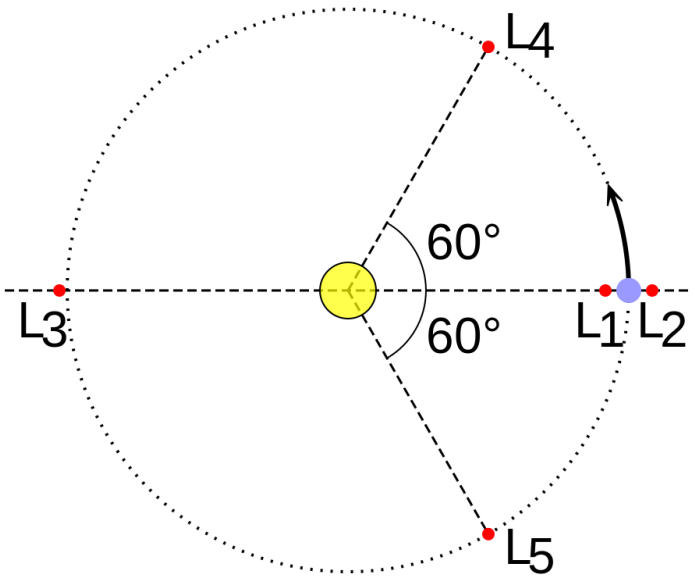

FIGURE 3.4: A schematic diagram showing the five Lagrangian points in the restricted three bodied problem. All points orbit with the same periodicity as the smaller body (e.g. the Earth) even though none lay exactly on the smaller body's orbital path.

At collinear point L1 the Earth's gravitational pull has the effect of reducing the gravitational potential of the Sun on the spacecraft, allowing it to orbit with the same periodicity as that of the Earth. Effectively, the spacecraft is always located directly between the Sun and the Earth, even as the Earth progresses through its orbit.

By placing ACE in orbit around L1, which is approximately 1.5 million kilometres ($\sim 235 R_E$) sunward of the Earth (0.99 AU from the Sun), it is able to constantly record the earthward solar wind. The average propagation time from the Sun to L1 for the solar wind is around three days whilst the average propagation delay time from L1 to Earth is of the order of one hour.

The propellant tanks in ACE originally held 195kg of hydrazine fuel which, it was anticipated, would provide a mission lifetime of five years with "considerable margin" (*Chiu et al.*, 1998). Although some of the original instruments have since been disabled or placed in a reduced data collection mode, ACE is still operational today and it is predicted that there is enough propellant to keep it in orbit until 2024 (*Davis and Hamell*, 2008).

3.4.1 Scientific Objectives

The primary objective of the ACE mission is to sample the elemental and isotopic composition of several particle populations. Those populations are:

- the solar corona,

- the solar wind,

- the nearby interstellar medium and

- galactical matter.

By studying these particle populations, the ACE mission was designed to investigate a wide range of "fundamental problems" in four areas: The Elemental and Isotopic Composition of Matter, Origin of the Elements and Subsequent Evolutionary Processing, Formation of the Solar Corona and Acceleration of the Solar Wind, and Particle Acceleration and Transport in Nature (*Stone et al.*, 1998).

ACE is able to take measurements of a range of nuclei ($1 \leq Z \leq 30$), from solar wind to galactic cosmic ray energies (100 eV up to several hundred MeV), at a resolution not yet

achieved at its launch (*Stone et al.*, 1998). ACE enables simultaneous measurements over a very broad energy range with a variety of instruments each optimised for specific ranges and it provides near-real time *in situ* monitoring which has allowed for the prediction of space weather events here at Earth (and further into the solar system).

3.4.2 Instrumentation

There are nine different science instruments on-board ACE which allow coverage of the wide range of energies ACE was designed to study. The instruments on-board, along with a description of the particle population they were designed to study, are given in Table 3.3.

Table 3.3: Instruments on-board the ACE spacecraft

Acronym	Instrument	Measured Species	Measured Quantities	Typical Energy (MeV/nuc)
CRIS	Cosmic Ray Isotope Spectrometer	$2 \leq Z \leq 30$	Z, M, E	≈200
SIS	Solar Isotope Spectrometer	$2 \leq Z \leq 30$	Z, M, E	≈20
ULEIS	Ultra Low Energy Isotope Spectrometer	$2 \leq Z \leq 28$	M, E	≈1
SEPICA	Solar Energetic Particle Ionic Charge Analyzer	$2 \leq Z \leq 28$	Q, Z, E	≈1
EPAM	Electron, Proton, & Alpha Monitor	H, He, e^-	Z, M, E	≈0.3
SWIMS	Solar Wind Ion Mass Spectrometer	$2 \leq Z \leq 30$	M, E/Q	≈0.001
SWICS	Solar Wind Ion Composition Spectrometer	$2 \leq Z \leq 30$	Z, E	≈0.001
SWEPAM	Solar Wind Electron, Proton & Alpha Monitor	H, He, e^-	E/Q dist.	≈0.001
MAG	Magnetometer	B	B_x, B_y and B_z	

For the research undertaken in this thesis, data from the magnetic field and solar wind instruments are used. The magnetometer instrument provides 3 to 6 vec/s resolution magnetic field data at an accuracy of ±0.1nT with ultra-sensitivity and low noise. It consists of two boom-mounted three-axis fluxgate magnetometers, which are located at the end of separate ∼4 meter long booms. Both magnetometers are identical and either can serve as the primary, or sole, sensor (*Smith et al.*, 1998).

The data for solar wind measurements is provided by the SWICS, SWIMS and SWEPAM instruments. The SWICS instrument is an ion composition sensor and it uses a combination of electrostatic deflection, post-acceleration, time-of-flight, and energy measurements for particle identification (*Gloeckler et al.*, 1998). The SWIMS instrument consists of an electrostatic deflection system, a time-of-flight High Mass Resolution Spectrometer (HMRS) and associated electronics. It is able to determine the abundance of nearly all of the chemical elements and most of their isotopes in the mass range 3 to 60 amu (*Gloeckler et al.*, 1998).

Of primary interest in this thesis, though, are the bulk parameters of the solar wind (e.g. velocity and density) rather than the composition and, for this, data from the SWEPAM instrument are exploited. The SWEPAM experiment provides the measurements from which the solar wind bulk flow and kinetic properties can be determined. The SWEPAM instrument has two sensors to measure the ion and electron distributions separately (SWEPAM-I for ions and SWEPAM-E for electrons). Both sensors contain a spherical section electrostatic analyzer which funnel incoming electrons or ions into electron multiplier detectors (*McComas et al.*, 1998).

Data from the ACE mission are freely and publicly available through the National

Oceanic and Atmospheric Administration (*Zwickl et al.*, 1998) and through the CDAWeb portal.

3.5 The OMNIweb Data Set

The OMNIweb data service, hosted at http://omniweb.gsfc.nasa.gov/ by NASA and the Goddard Space Flight Center, freely provides both high (1-min, 5-min) and low (1-hour) resolution near-Earth magnetic field and plasma data. The high-resolution OMNI data set, made available through the OMNIweb interface, is an interspersal of data from the ACE, Wind, IMP 8 and Geotail missions.

In addition to this combined data set, the OMNIweb service has collated the individual data sets for each spacecraft mission and has made them available for download through its service. The data for the combined set are chosen based on quality selection criteria and are primarily selected from the ACE (see section 3.4) and WIND missions.

Since the process of lagging data from an upstream observer (e.g. ACE) to the Earth is non-trivial, the OMNI data set provides a convenient source of near-Earth magnetic field and plasma data and so it is widely used throughout the solar-terrestrial scientific community.

3.5.1 Lagging to the Bow Shock

It is impractical and, indeed, almost impossible to have constant recording of the solar wind conditions in the near-Earth region of space. The time for which any near-Earth

spacecraft can be observing the incoming solar wind is constrained by its orbital configuration and there will always be periods of time where it cannot accurately observe upstream conditions. As such, unless there were multiple spacecraft in a similar orbital configuration, thus creating a "net" of observers, constant recording is not feasible using near-Earth spacecraft alone.

An upstream observer, located at L1 (see Section 3.4), however, has a continuous and unobstructed view of the earthward solar wind conditions. Since L1 is located ∼1.5 million kilometres upstream of the Earth, it takes some finite period of time (of the order of one hour) for the solar wind, as measured by the observer, to reach the Earth.

To account for this, the OMNI dataset is time-shifted using a set routine so that it better represents the conditions at the bow shock at any given time. To do this, the key assumption is that IMF conditions observed by a spacecraft at some fixed point in space and time lie on a phase front which travels along with the solar wind, so that when the phase front passes through another location at a later time the same conditions would be observed.

The determination of this phase front, specifically the phase front normal (PFN) direction, is a key element of the time shifting calculation. The OMNI service calculates the PFN, for each 15-16 sec magnetic field vector, in two different ways: using a constrained minimum variance analysis which assumes that IMF B lies in the plane of the discontinuity (MVAB-0) and a cross-product analysis (CP) of the magnetic field vectors just before and just after the discontinuity.

The MVAB-0 technique, as described in *Haaland et al.* (2006), is a development of the MVAB method which was first discussed in *Weimer et al.* (2003) and later corrected

in *Weimer* (2004). The MVAB method is itself based upon the MVA technique whose applicability to spacecraft data was first demonstrated in *Sonnerup and Scheible* (1998). The MVA methods are based upon finding the eigensolutions to the symmetric, 3 by 3 magnetic variance matrix:

$$M_{ij} \equiv \langle B_i B_j \rangle - \langle B_i \rangle \langle B_j \rangle \tag{3.1}$$

where B_i and B_j are the Cartesian vector components of the magnetic field measurements.

With the MVAB-0 technique, the magnetic variance matrix (equation 3.1) is multiplied by the projection matrix:

$$P_{ij} = \delta_{ij} - \hat{e}_i \hat{e}_j \tag{3.2}$$

where δ_{ij} is the Kronecker δ and the unit vector $\hat{e}$ is defined by:

$$\hat{\mathbf{e}} = \frac{\langle \mathbf{B} \rangle}{B} \tag{3.3}$$

The eigenvector corresponding to the intermediate eigenvalue, taken from the resultant matrix, is used as the prediction for the PFN (*Haaland et al.*, 2006).

The CP method, as outlined in *Knetter and Neubauer* (2004), assumes that the discontinuity is perfectly tangential. In this case, the PFN ($\mathbf{n}$) can be estimated by calculating

the cross product of the discontinuity's upstream magnetic field vector ($\mathbf{B_u}$) and downstream vector ($\mathbf{B_d}$):

$$\mathbf{n} = \frac{\mathbf{B_u} \times \mathbf{B_d}}{|\mathbf{B_u} \times \mathbf{B_d}|} \tag{3.4}$$

To determine the PFN, OMNI first use the CP method. If an acceptable PFN is determined, then this calculated value is used as the PFN, else if CP does not produce an acceptable PFN (such as if the angle between the before and after vectors is less than 13°), then the MVAB-0 technique is instead used. If neither CP nor MVAB-0 techniques produce an acceptable PFN, then an interpolation between the last and next acceptable points is attempted (so long as the time interval between the two is not over three hours).

Once the PFN has been determined, the time-shifting equation (equation 3.5) is used to calculate the lag time (Δt).

$$\Delta t = \frac{n \cdot (R_d - R_o)}{n \cdot V} \tag{3.5}$$

where R_o represents the location of an observing spacecraft (e.g. ACE) and R_d represents the displaced location (i.e. the bowshock nose). The solar wind velocity is denoted as V and the PFN is n.

The location of the bowshock is obtained through the following equation (see equation 2.56 for definition of terms):

$$D_{BS} = D_{OB}\left[1 + 1.1\frac{(\gamma - 1)\,M_1^2 + 2}{(\gamma + 1)\left(M_1^2 - 1\right)}\right] \tag{3.6}$$

It is interesting to note that *Farris and Russell* (1994) suggest that this model should not be used as it does not take into account the shape of the obstacle and instead suggest that the model given in equation 2.56 be used when calculating the distance to the bowshock.

It is important to note that the curvature of variation surfaces is ignored when calculating the delay time as is any propagation of the phase fronts relative to the solar wind flow. Other assumptions made include assuming that the discontinuity is perfectly tangential when using the CP method (which is the most commonly used method to determine the PFN) and that the response time of the magnetosphere to changes in the solar wind is negligible.

All of the above assumptions may introduce some error into the delay time calculation. Testing the OMNI predictions is therefore an important task and is one which is undertaken in Chapter 4.

Chapter 4

A statistical comparison of solar wind propagation delays derived from multi-spacecraft techniques

This chapter is formed from the publication *Case and Wild* (2012).

Undertaken in this chapter is a large-scale statistical study of the solar wind propagation delay between NASA's Advanced Composition Explorer spacecraft and ESA's Cluster 1 spacecraft. This study focuses on those periods when Cluster was within the unimpeded solar wind, upstream of the bow shock nose, between 2001 and 2010. Using a cross-correlation method to compare the ACE and Cluster data, nearly 5000 propagation delays have been calculated and compared to both corresponding propagation delays in the OMNIweb dataset and to those computed by a simple "flat" (i.e. distance/speed) propagation model. The results show that statistically there is little difference between

the OMNI and flat propagation delay times and that the cross-correlation method agrees well with both, but there are times when the various methods give significantly different propagation estimates. We find that the solar wind speed and IMF orientation seem to have no influence upon the relationship between the estimated and observed solar wind propagation delays.

4.1 Introduction

To understand many of the processes in the coupled solar wind-magnetosphere-ionosphere system, it is necessary to characterise the interplanetary conditions which drive them. Many magnetospheric phenomena, such as geomagnetic storms and auroral substorms, are known to be driven by the solar wind with key aspects of their evolution tied to particular solar wind and interplanetary magnetic field (IMF) conditions [e.g. *Zhou et al.* (2000); *Angelopoulos et al.* (2008) and *Wild et al.* (2009)]. To correctly attribute the sequence of cause and effect between magnetospheric dynamics and drivers in the solar wind and embedded IMF, accurate specification of interplanetary conditions is essential.

Although many satellites sample the solar wind and IMF upstream of the Earth, continuous monitoring of the field and plasma conditions impinging upon the magnetosphere some 10 R_E sunward of the planet is not possible due to the orbital motion of the satellites. A common approach is to exploit satellite measurements made at a location much further upstream and apply a temporal delay to account for the propagation of solar wind and IMF structures from the satellite to the magnetosphere, assuming that the structures do not evolve in the intervening period. The Advanced Composition Explorer

(ACE) satellite is particularly suited to this role. ACE orbits about Lagrangian liberation point 1 (L1) and is, therefore, constantly within the antisunward flowing solar wind $\sim 240\ R_E$ ($\sim$1.5 million km) upstream of Earth (*Stone et al.*, 1998).

Previous studies have shown that most propagation delays are of the order of one hour (*Mailyan et al.*, 2008), although it is not accurate to assume this value for all intervals. Variations of $\pm 30\ mins$ in the delay times, even over short time scales, are possible (*Weimer et al.*, 2003).

Several studies have set out to ascertain more accurate values for the solar wind propagation delay under various conditions (e.g. *Khan and Cowley* (1999), *Horbury et al.* (2001), *Weimer et al.* (2003) and *Weimer and King* (2008)). However, no method has been proposed that is able to accurately determine a delay for all situations. Indeed, most methods outlined are applied to the solar wind during certain conditions, primarily when there is a discrete discontinuity in the IMF (e.g. *Mailyan et al.* (2008)).

The difficulty in accurately predicting the delay time of the solar wind has been the primary reason for the development of OMNIWeb (http://omniweb.gsfc.nasa.gov). OMNIWeb combines data from multiple spacecraft (ACE, Wind, IMP 8 and Geotail) to produce a high resolution database of solar wind conditions lagged to the nose of the Earth's bow shock. They calculate the appropriate lag time to apply to the data, using the time-shift equation given in equation 4.1:

$$\Delta t = \frac{n \cdot (R_d - R_o)}{n \cdot V} \tag{4.1}$$

where R_o represents the location of an observing spacecraft (i.e. ACE) and R_d represents the displaced location (i.e. the bowshock nose). The solar wind velocity is denoted as V and the phase front normal (PFN) of the solar wind is n.

The determination of the PFN, using a single spacecraft observer, is non-trivial and is estimated using a suite of methods based upon Minimum Variance Analysis (MVA) and Cross Product (CP) methods (refer to section 3.5.1 for further details). The OMNI website notes, however, that when applied to the whole data set all the methods give statistically similar results.

Although not routinely available, the disposition of magnetospheric spacecraft, such as Cluster, leads to intervals when a satellite is located in the solar wind, just upstream of the bow shock, for a short period (typically a few hours). Such conjunctions of satellites, one in the vicinity of the L1 point and another just upstream of the bow shock, present opportunities to compare the estimated interplanetary conditions impinging upon the magnetosphere (based upon lagged upstream data) to *in situ* solar wind and IMF measurements. These well-instrumented periods therefore allow the accuracy of the solar wind propagation techniques to be examined. In this study we present solar wind propagation delays, as calculated by a cross-correlation method using L1 and near-Earth satellites, and compare these to the corresponding propagation delays computed by the popular OMNIWeb tool and simple flat propagation estimates.

4.2 Methodology

An example of the methodology used in this study, which is to cross-correlate upstream data with near-Earth data to determine an appropriate delay time, is shown in Figure 4.1. The plots in columns a), b) and c) of Figure 4.1 show the IMF conditions between 12:20 and 14:20UT, on 01 March 2003, at ACE (a), Cluster-1 (b) and the corresponding OMNI data (c) for the same interval. Plot d) shows the clock angle at ACE in blue and at Cluster in green. Clearly, the clock angles do not match up due to the solar wind propagation delay from ACE to Cluster.

The clock angle was chosen as the variable on which to perform the correlation analysis since it gives an overview measure of the IMF, rather than a singular component of the IMF (e.g. B_z), and since it yielded a greater number of valid delays than the field magnitude (the definition of validity is described in section 4.2.3).

The IMF clock angle is determined by calculating the arctangent of the ratio of the y- and z-components of the magnetic field, as shown in equation 4.2. It describes the direction of the IMF in the y/z plane.

$$\theta = \arctan\left[\frac{By}{Bz}\right] \tag{4.2}$$

By performing a cross-correlation analysis, the process of which is described in detail in section 4.2.2, on the ACE and Cluster clock angles, it is possible to determine an

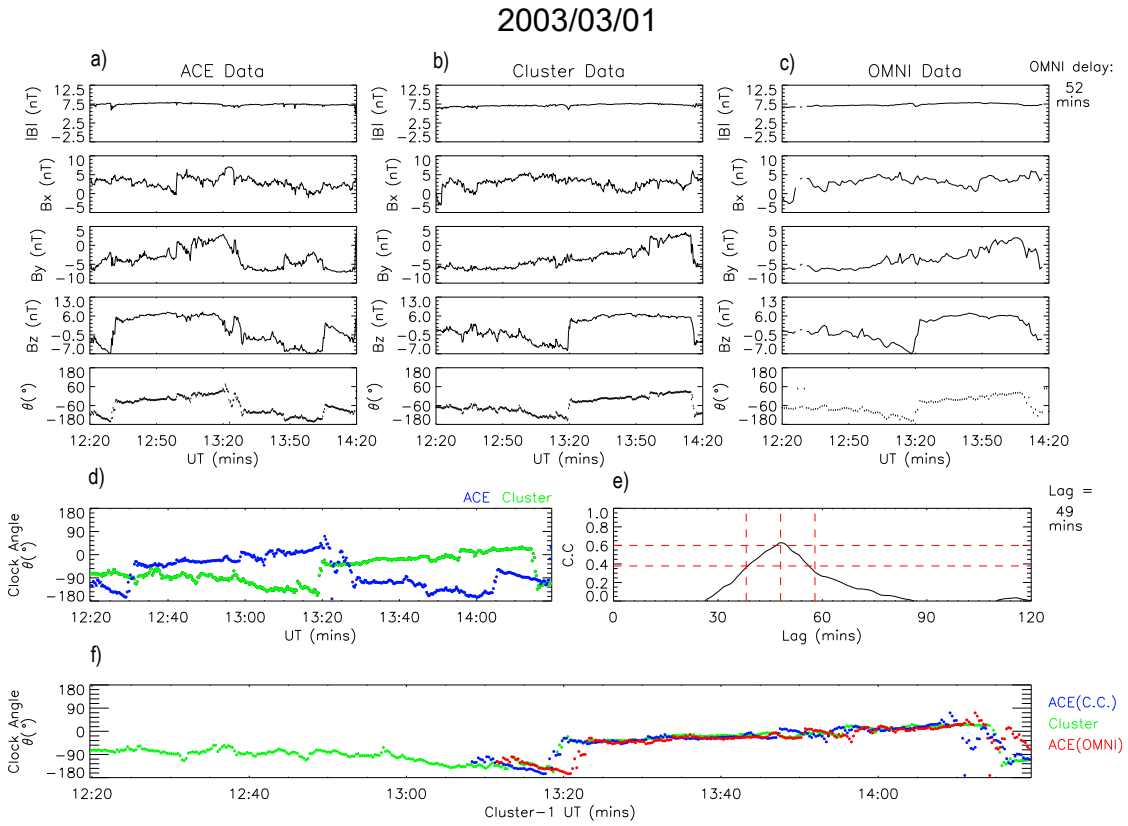

FIGURE 4.1: Columns a) and b) show the magnetic field conditions at ACE and Cluster; whilst column c) plots the corresponding OMNI data. Plot d) shows the clock angle at ACE (blue) and at Cluster (green) on the same time series. As discussed later in the text: the cross-correlation profile is shown in plot e) where the horizontal red lines indicate the maximum threshold (60%) and the minimum correlation (0.6); the vertical lines indicate the 10 mintue window about the highest peak. Plot f) shows the clock angle (θ) at ACE lagged by the calculated cross-correlation delay in blue and by the OMNI delay in red. Shown in green is the measured clock angle at Cluster.

appropriate delay between the time-series of IMF measurements at ACE and the equivalent time-series occurring some time later at Cluster (assuming both time-series are measurements of the same IMF variations but displaced in time).

Plot e) in Figure 4.1, is of the cross-correlation profile for the ACE and Cluster clock angles shown in plot d). The plot presents the corresponding correlation coefficients as a function of the delay time for which the segment of ACE data is shifted by. The peak of the correlation profile in this example fulfils certain conditions, as discussed in section 4.2.3, and so the delay time represented by the highest correlation is used.

In this case, since the correlation conditions are met, the full width plot f) in Figure 4.1 shows the clock angle measured by ACE shifted by the calculated propagation delay time in blue, shifted by the corresponding averaged propagation delay from OMNI in red and the clock angle measured at that time at Cluster in green. In this example, when the clock angle measured by ACE is shifted by the cross-correlation delay it clearly aligns with the Cluster clock angle (which is expected) and it also aligns much more closely than when it is shifted by the OMNI delay.

This cross-correlation analysis can be repeated for all times when both ACE and Cluster data are available, yielding a database of ACE-to-Cluster propagation delays. These delays can then be directly compared to any other method or model that estimates the propagation delay of the solar wind from ACE. In this study, the delays derived from the cross-correlation analysis are directly compared to contemporaneous delays within the OMNI dataset and to a simple antisunward planar propagation delay model, known as a "flat" delay.

The flat delay assumes that the solar wind simply traverses from point A, i.e. ACE, to point B, i.e. the bow shock nose, at a constant speed and that there are no fundamental changes to the solar wind as it traverses. Since OMNI calculates the lag time to the bow shock nose, and since the nose is not fixed in position, the distance the solar wind travels is variable and is dependent upon the model used. The position of the bow shock nose, in the flat propagation calculation, is taken to be the same as OMNI predicts, so as to eliminate any differences due to modelling. The position of ACE also varies slightly due to its orbital configuration at L1 which is taken into account. Since this is a simple propagation calculation, only the separation distance and propagation velocity

in the GSE x-direction are used in the computation. The GSE x-component of the solar wind velocity is taken as it passes ACE and is assumed to be constant throughout its Earthward propagation.

As shown in equation 4.3, the delay is calculated by dividing the separation distance of ACE and the bow shock nose, in the GSE x-direction, (Δs_x), by the average x-component of the solar wind velocity, measured by ACE, during the correlation period (V_{avg}).

$$t_{lag} = \frac{\Delta s_x}{V_{avg}} \tag{4.3}$$

4.2.1 Data selection

Simultaneous data were obtained from both the ACE and the Cluster 1 satellites during periods where Cluster's orbit would place it, for the most-part, sunward of the Earth's magnetosphere. This condition restricted our study to the months of January to April, from years 2001 to 2010, inclusive.

Two further restrictions were imposed to ensure that Cluster was outside of the bow-shock. Firstly, only data recorded when Cluster was located at distances greater than 15 R_E upstream of Earth were used. Secondly, the ion temperature, as measured by the Hot Ion Analyser which is a part of the Cluster Ion Spectrometer (CIS) instrument (discussed in section 3.3.2), must also have been less than 1keV for the data to be included (see *Wang et al.* (2012) for temperature distributions of the different plasma regimes). This allows for direct comparison with OMNI data which has been propagated from an

upstream spacecraft to the bow shock nose, as determined by the bowshock model of *Farris and Russell* (1994) and the magnetopause model of *Shue et al.* (1997).

Since Cluster was not necessarily located at the bow shock when the data was recorded, the delay time calculated may not represent the true delay time for propagation to the bow shock. The delay calculated was therefore increased by an appropriate factor based upon the solar wind speed, as measured by Cluster, and the difference between Cluster's location and the location of the bow shock, as given by OMNI, at that time. The factor, which was generally of the order of one minute, was simply a speed/distance calculation in the GSE x-direction only, as the GSE y-z difference between the spacecraft and the bowshock nose is minimal when compared to the y-z distance from the Earth-Sun line for the ACE spacecraft.

4.2.2 Correlation Conditions

Performing a cross-correlation analysis of two data sets is most straight forward when the data are joined to the same time tags, however, the three different data sources used in this study provide data at different cadence. The data are therefore re-sampled to the required cadence using a mean average over the resample period - ignoring any bad data flags.

The length of the period over which the cross-correlation analysis is performed can be important and must first be defined. Too short a period may result in no correlation being obtained whilst too long a period may be affected by any long term repeating structures. After reviewing several different correlation periods (i.e. of 5, 10, 20 and 30 minutes in length) and the resulting correlation profiles on the same sets of data, a period

of approximately ten minutes, or exactly 38×16 second resolution data points, was found to provide the highest correlation coefficient for the majority of the data intervals. Once the lag time with the maximum cross-correlation coefficient has been identified, both of the raw time-series are shifted by one minute and a new lag time corresponding to the maximum cross-correlation coefficient is again identified. A period of one minute for the shifting was chosen to produce a time delay data set of the same cadence as the OMNI data set.

Determining the limits of the cross-correlation analysis, i.e. the minimum and maximum lags over which to perform the comparison, is non-trivial and, for best results, would require *a priori* knowledge of the propagation delay time. However, it is clear that there must be some propagation delay between ACE and Cluster, since the solar wind travels at a finite velocity over a finite distance; it is therefore not unreasonable to set the minimum condition at zero minutes. If it is assumed that the propagation delay between the spacecraft is typically one hour, a maximum limit of two hours is reasonable.

4.2.3 Quality Measures

To ensure that the delays calculated by the cross-correlation function were valid, several quality measures were introduced on the resultant correlation profiles. One of these conditions was applied to all data, whilst two further conditions were variable and could be adjusted to view their effects on the quantity and quality of data.

The compulsory condition was that the peak of the correlation function must be positive. A negative correlation would imply that the data is anti-correlated which is unphysical in this case.

The first of the two variable quality measures was the minimum acceptable correlation coefficient. By defining a minimum correlation coefficient, only those delays calculated from data which correlates at this minimum level or higher are included. If this level is set high, then only data which has correlated well is used and so the confidence in the quality of the calculated delay is increased. However, if this level is set too high then significant amounts of data would no longer meet the criteria and would be excluded from the results.

The correlation function will often produce several peaks; sometimes it is clear which peak is more dominant from visual inspection, however in other cases there may only be a slight difference in the height of the peaks. In order to confidently determine the propagation delay, the correlation coefficient peak (i.e. a delay at which the correlation coefficient is at its highest) must be distinct. The definition of distinct is somewhat arbitrary, thus requiring the use of the second variable condition. The maximum relative percentage height of any secondary peaks to the primary peak (herein named the "maximum threshold" condition) ensures that the primary peak is distinct from any secondary peaks.

After manually investigating the effect of altering both the minimum acceptable correlation coefficient and the maximum threshold condition, the values of 0.6 and 60% were chosen. These values were found to increase the quality of the inspected delays whilst also producing enough delays to enable a statistical study to be undertaken.

In addition to the correlation function, a least squares fit was performed on the data sets for different delay values. Only if the least squares minimum coincided with the

maximum correlation peak was the delay recorded. This was to ensure that not only did the two data sets correlate but that they also aligned.

Figure 4.1 is an example where the cross-correlation meets all required conditions and, as such, the delay it produces would be accepted. There is clearly only one distinct peak in its correlation profile, in addition, this peak is positive and of a value which meets or exceeds the minimum correlation value.

Of course, this is not always the case and depending upon the conditions set in place, much of the data may be rejected. Figure 4.2 displays the data in the same format as in Figure 4.1, for a different time period in March 2003; however, the computed delay is not accepted because the maximum correlation peak in Figure 4.2 fails to meet the required minimum correlation coefficient. In addition, whilst there is a larger peak in the correlation, there are also multiple smaller peaks indicating that this example may fail on the threshold condition also.

4.3 Results

In the following section, the cross-correlation delays are compared against those predicted by the OMNI dataset. OMNI freely provide high resolution solar wind data, such as the solar wind plasma and IMF parameters, which have already been lagged to the bow shock nose. Since this lagging is a non-trivial process, the OMNI data set is a widely used and accepted source of solar wind data.

The OMNI team have accounted for several different variables when they produced their estimated propagation times, as shown in equation 4.1, though to achieve such high

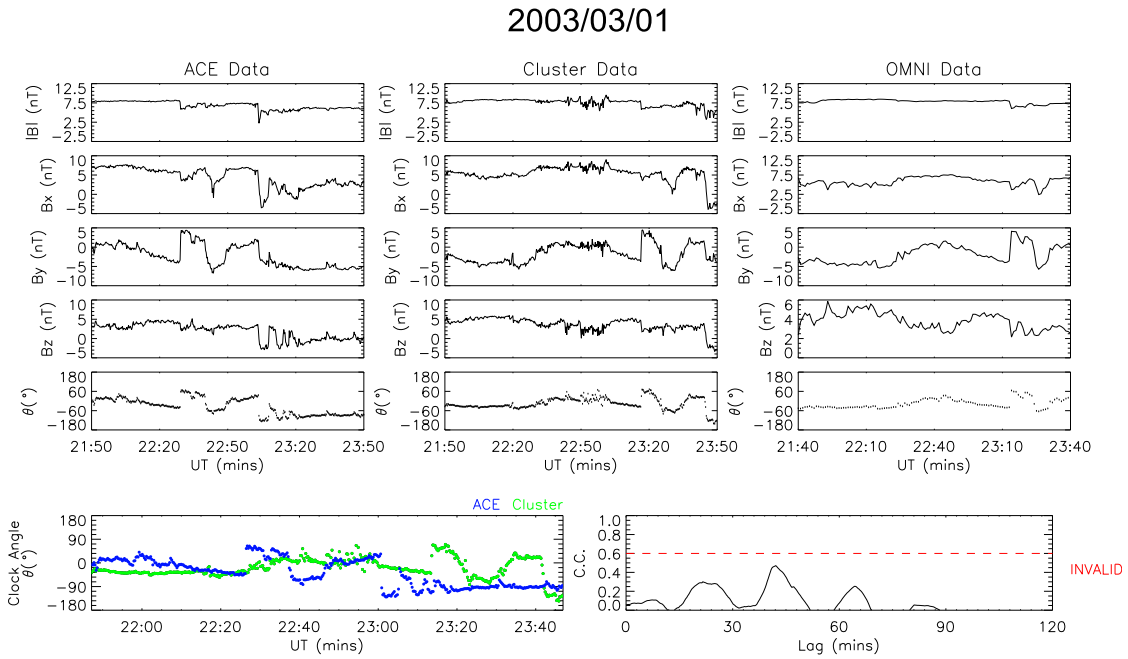

FIGURE 4.2: An example where the correlation conditions are not met, specifically the maximum correlation coefficient fails to meet the required minimum level; therefore the delay is not accepted. The format of the figure is the same as Figure 4.1.

resolution data two key assumptions are made. Firstly, the solar wind travels in a series of phase fronts, but any curvature in these fronts is ignored, and secondly that these fronts convect at the solar wind velocity.

With the amount of data available in this study it is possible to directly test the OMNI model in a statistical survey, not just as a specific case study. This study will also show the relationship of two delays based upon the solar wind speed and IMF orientation, as measured by ACE.

Plotted in Figure 4.3 are the corresponding OMNI and calculated cross-correlation delays. They have been grouped into five minute bins and their density is represented using the colour scale. The cross in each column denotes the mean average for that column; the "error" bars represent ±1 standard deviation from the mean.

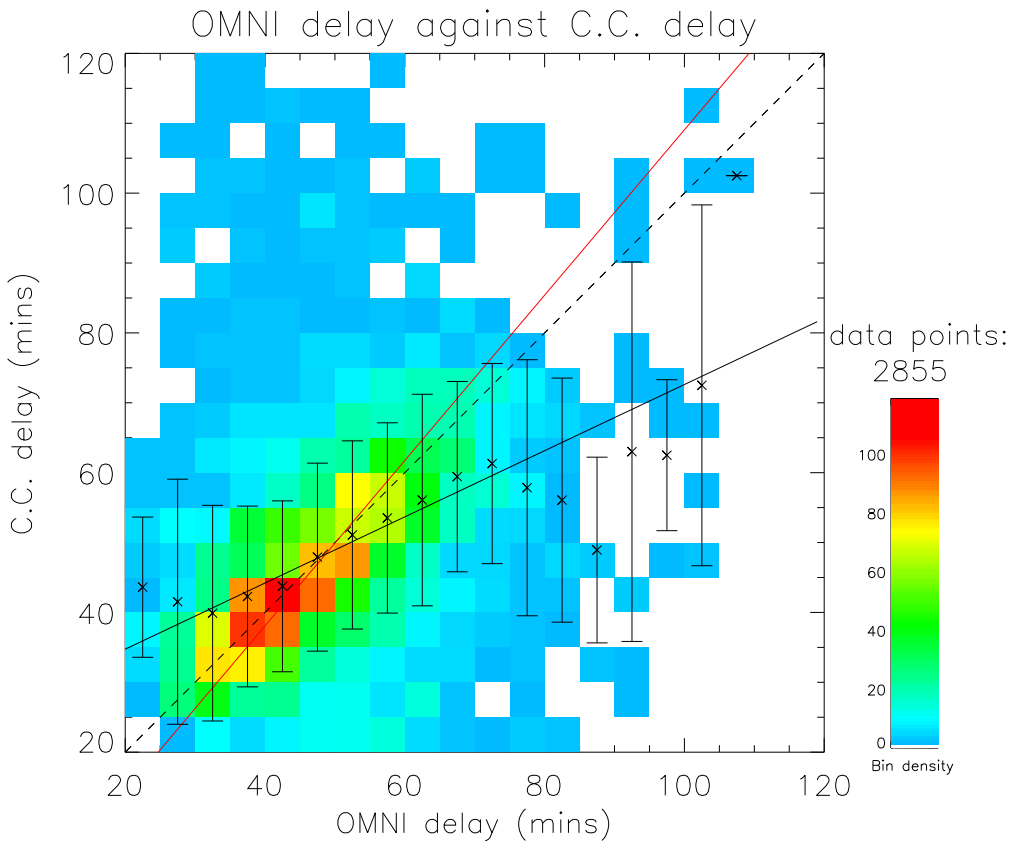

FIGURE 4.3: A density plot of the OMNI delay against the cross-correlation delay. There are no quality constraints in place on the data. The black line is a standard least squares fit whilst the red line is weighted least squares fit.

The origin of the plot has been set at twenty minutes on both axes, rather than zero, since it was found that the minimum flat delay was twenty three minutes, with the overwhelming majority of flat delays greater than thirty minutes. It was therefore considered unlikely that any cross-correlation delay or OMNI delay was correct if it was estimated to be less than twenty minutes.

The data shown in Figure 4.3 has no quality measures in place (i.e. no restrictions on the minimum correlation or maximum threshold), resulting in 4938 delays produced from the 2001-2010 Cluster data set.

The black line in the plots is a standard least squares fit computed from all data points;

whilst the red line is a weighted least squares fit, again computed from all data points, which also incorporates the standard deviation of the two data series. This weighted least squares function is able to reduce the effect of an outlying point when calculating the line of best fit.

There is considerable spread in the delays shown in Figure 4.3, however, note that the blue coloured bins are an order of magnitude less in density than the red coloured bins. The plot clearly exhibits a dense grouping of delays in the region of 30-60 minutes (on both axes). The averages of the columns in this dense grouping all fall within ± 1 s.d. of the $y = x$ line.

In Figure 4.4, the OMNI and cross-correlation delays are again compared, in the same format as before. However, with the quality constraints of a minimum correlation coefficient of 0.6 and a 60% maximum threshold now in place, only 164 delays are plotted.

Most of the spread has been filtered out, with just one outlier significantly off the $y = x$ line, and almost all of the column averages lie within ± 1 s.d. from the $y = x$ line. Only the high density region observed in Figure 4.3, corresponding to delays of approximately 30-70 minutes, remains.

4.3.1 A Flat Delay

Figure 4.5 presents the density of delays for the cross-correlation delay against the flat delay, using the same format as in Figure 4.3. It is quite apparent that the cross-correlation method can produce delays which are much longer than their equivalent flat

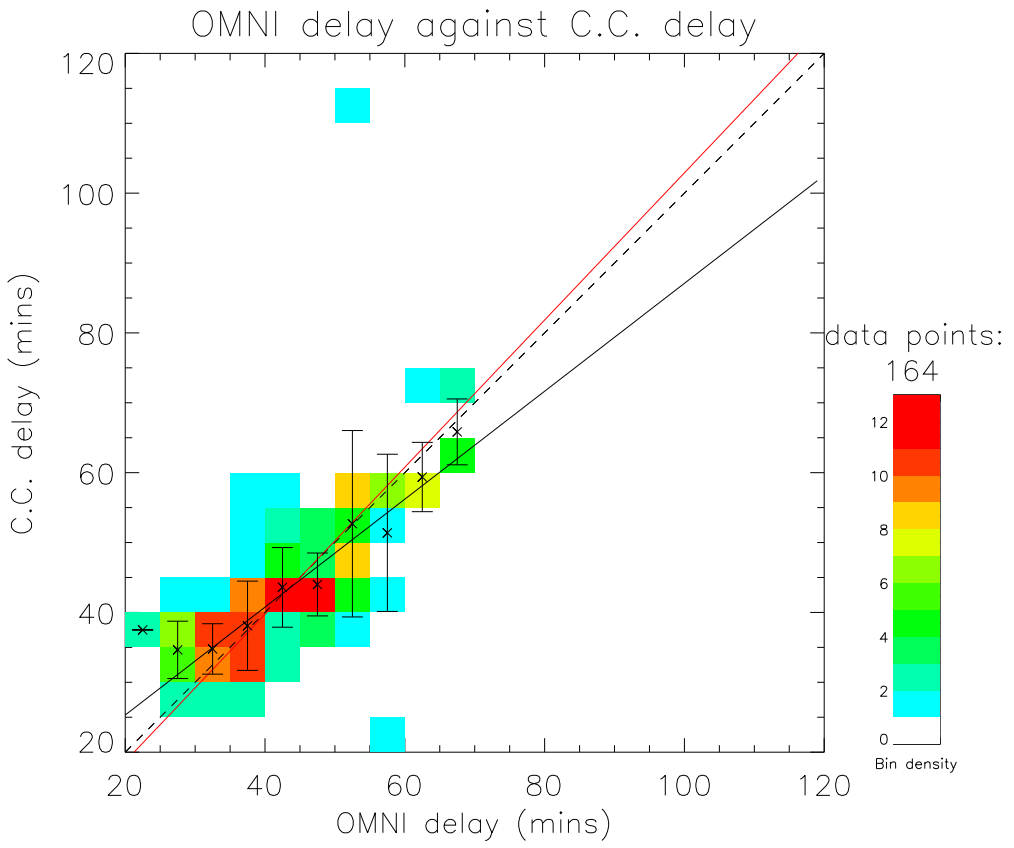

FIGURE 4.4: A density plot of the OMNI and cross-correlation delays constrained by a minimum correlation of 0.6 and maximum threshold of 60%.

delay. However, as with Figure 4.3, there is a clear high density grouping from around 30-60 minutes which seems to fit well with the y=x line.

Figure 4.6 shows the density of delays from the OMNI data set against the flat delay with the same formatting as the earlier density plots. The delays used here are from the months where Cluster's orbit would primarily pass outside of the bowshock, i.e. January - April, for seasons 2001 through 2010. The delays are not limited to those matching up with the delays calculated by the cross correlation method. There is considerably less spread than with the cross-correlation plots and, as with the other plots, there is a high density region from approximately 30-60 minutes (on both axes) which fits well with the $y = x$ line. Note how the red coloured bins are four orders of magnitude greater than

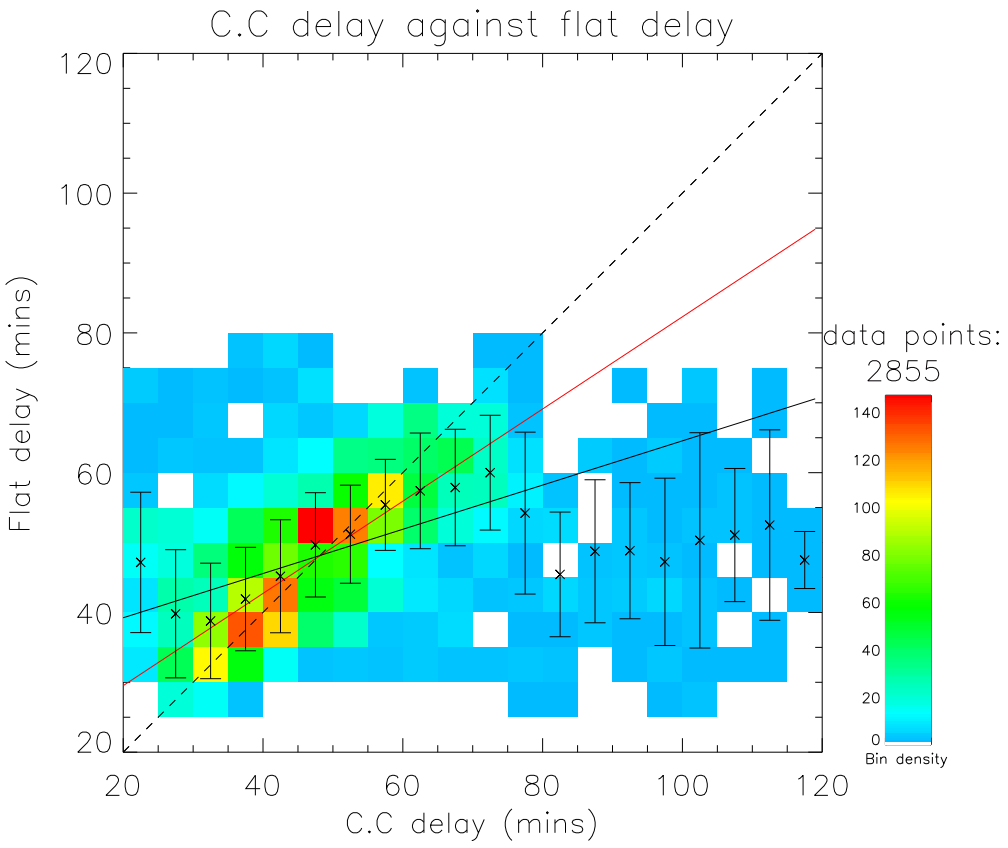

FIGURE 4.5: A density plot of the cross-correlation delay against flat delay.

the blue coloured bins.

4.3.2 The Effect of Solar Wind Speed

Solar wind speed is defined herein as the x-component of the solar wind velocity, as the solar wind flows past ACE, averaged over the cross-correlation period.

In Figure 4.7, the OMNI and cross-correlation delays are compared and coloured by the solar wind speed. As in Figure 4.4 the data is constrained by a minimum correlation coefficient of 0.6 and maximum threshold of 60%.

In order to determine what effect, if any, the solar wind speed may have on the relationship between OMNI and the cross-correlation delay method, it is prudent to split the

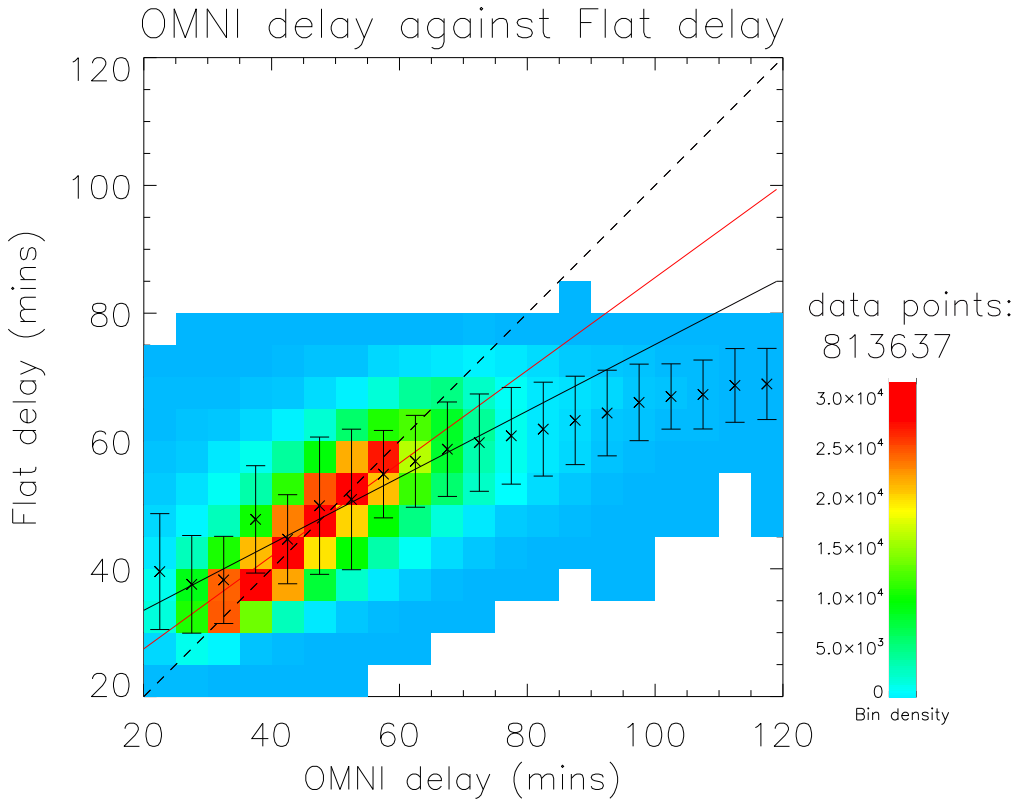

FIGURE 4.6: A density plot of the OMNI delay against the flat delay

delays depending upon their respective solar wind speed. In Figure 4.7 the delays have been grouped into slow, medium and fast solar wind speeds. Rather than arbitrarily choosing what limits each grouping should have, the groupings were determined using tertiles.

As would be expected, there is a general trend indicating that slower solar wind speeds tend to produce longer delay times than the faster solar wind. There is good agreement between OMNI and the cross-correlation method for fast, medium and slow solar wind speeds when using the weighted least squares fit function.

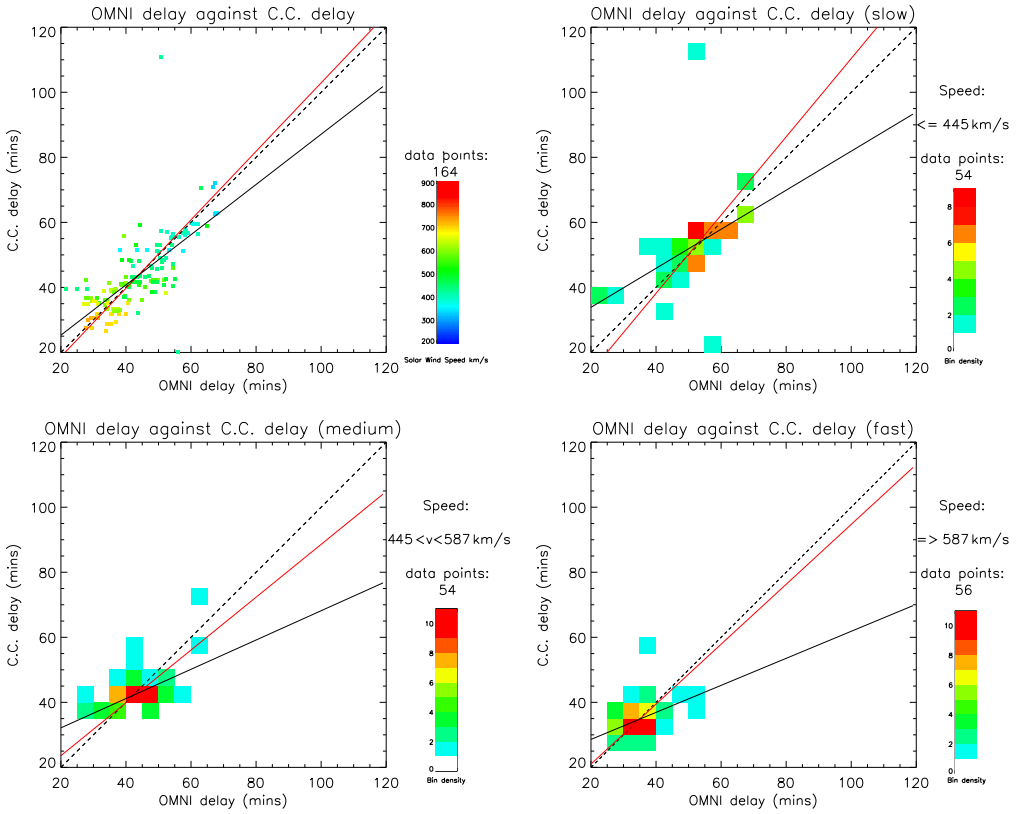

FIGURE 4.7: OMNI and cross-correlation delays are represented by their respective solar wind speed. In the first of the plots in the figure, the delays are coloured by their speed. In the three other plots, the delays have been split into slow, medium and fast speeds and shown as a density plots.

4.3.3 The Effect of IMF Orientation

The orientation of the IMF can be described using spherical coordinates, where the inclination and azimuth angles are the clock angle and cone angle respectively.

The clock angle may be calculated as previously shown in equation 4.2; whilst the cone angle, as shown in equation 4.4, is the angle between the IMF vector and the Earth-Sun line.

$$\phi = \arctan\left[\frac{Bx}{\sqrt{(By^2 + Bz^2)}}\right] \tag{4.4}$$

The following figures show the OMNI and cross-correlation delays coloured by their clock angle in Figures 4.8 and 4.9 and by their cone angle in Figure 4.10.

4.3.3.1 Clock Angle

The clock angle has a range of 360 degrees. In the GSE co-ordinate system, a vector with clock angle 0°/360° points in the upward direction perpendicular to the plane of the Earth's orbit, hereafter referred to as "North", and with 180° points downward, hereafter referred to as "South"; vectors with clock angles of 90° and 270° point Duskward and Dawnward respectively.

Figure 4.8 shows the delays by the different clock angles for minimum correlation coefficient 0.6 and maximum threshold of 60%. Since the clock angle freely fluctuated during the correlation periods, the clock angles were binned into 45° sectors and the most common sector value was chosen as the clock angle for that period.

The sectors of 45° were specifically chosen so as to be aligned with the major and semi-major orientations and the densities of these sectors are shown in Figure 4.9. This will indicate what, if any, statistical effect the direction of the IMF has upon the relationship between the OMNI and cross-correlation delays.

4.3.3.2 Cone Angle

The cone angle has a range of 180° (±90°); a vector with a -90° cone angle points toward the Earth along the Earth-Sun line whilst one with a +90° cone angle points toward the Sun. Figure 4.10 shows the directionality of the IMF, by its cone angle, for

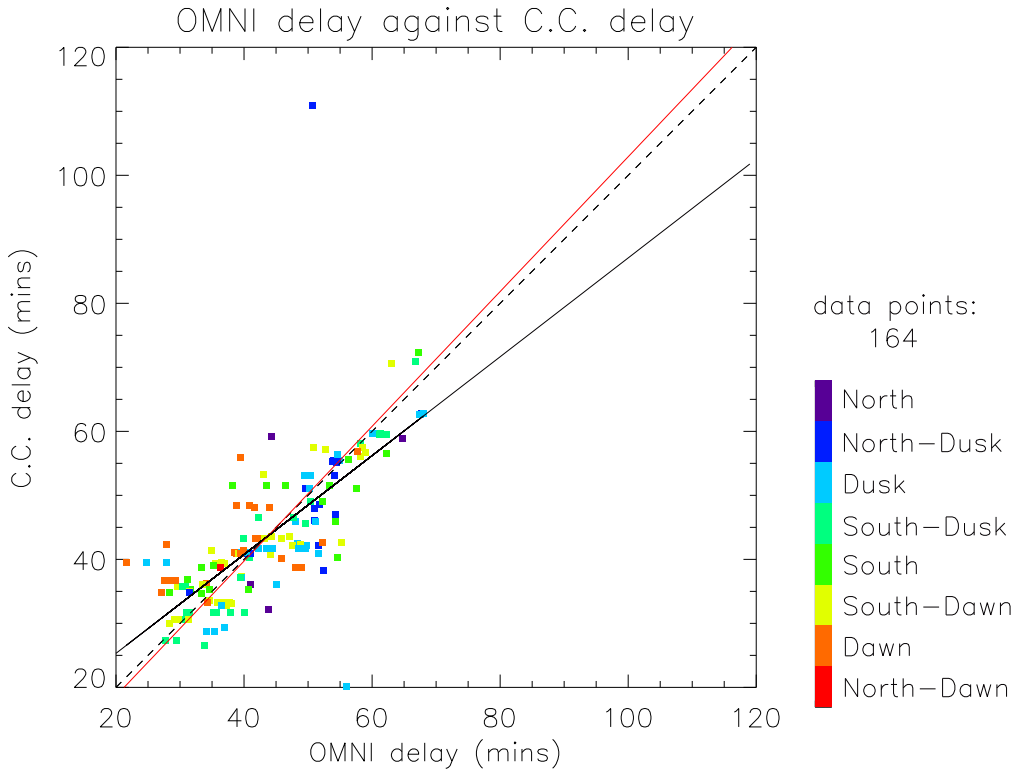

FIGURE 4.8: A scatter plot of the OMNI and cross-correlation delay represented by solar wind clock angle.

a minimum correlation coefficient of 0.6 and a maximum threshold of 60%. As with the clock angle, the cone angle chosen for the correlation period was the most common sector value. However, in the case of the cone angle three specific sectors were chosen: angles primarily pointing in the positive GSE x-direction; in the negative GSE x-direction and in a direction within the y-z plane.

In the first plot in the figure, the delays have been coloured by their sector cone angle. The other three plots in the figure show the density of delays for each sector.

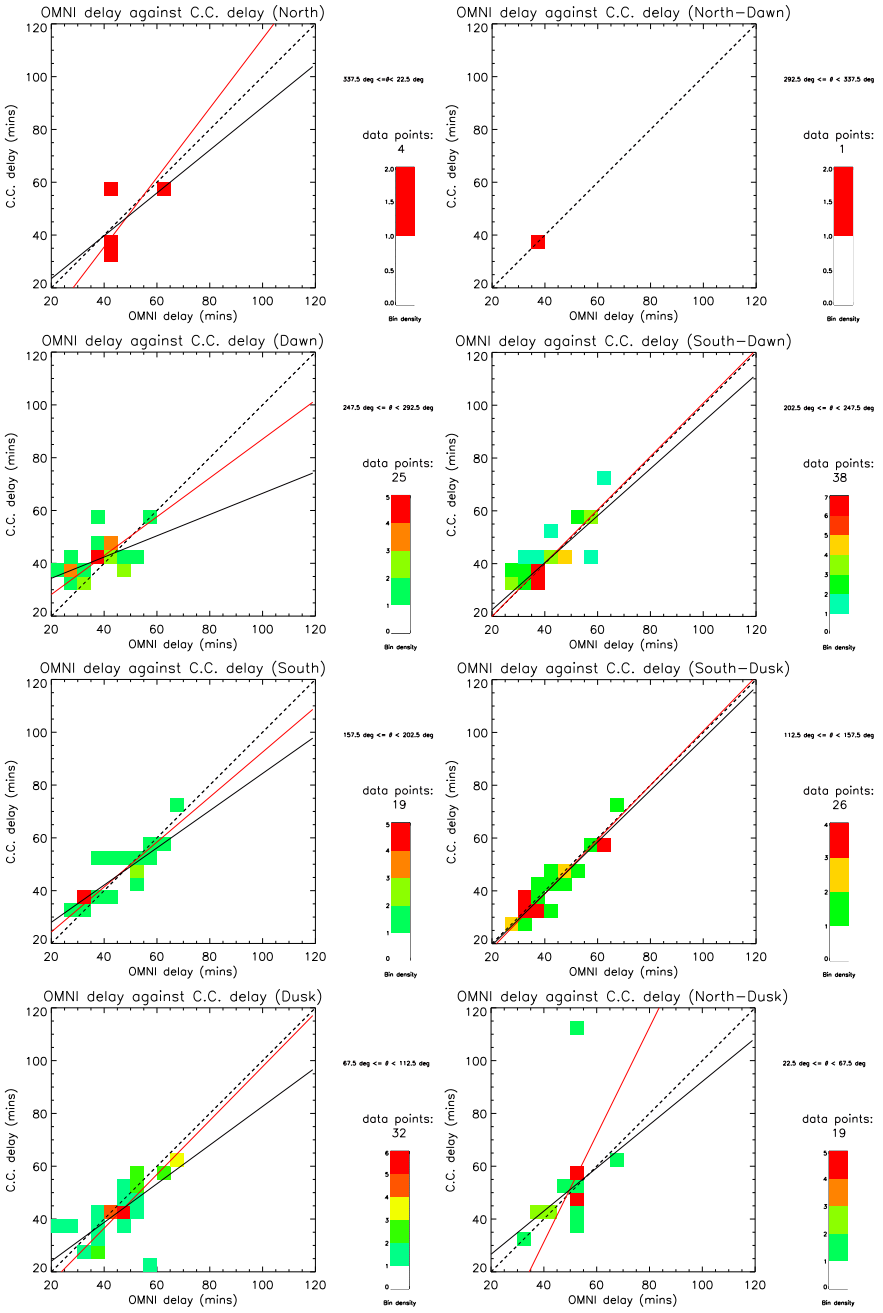

FIGURE 4.9: Delays represented by clock angle (θ) grouped into eight directions. The quality conditions imposed were minimum correlation 0.6 and maximum threshold of 60%.

4.4 Discussion

We have presented a statistical analysis of nearly 5000 solar wind propagation delays, reduced to 164 delays after quality filtering, calculated by performing a cross-correlation

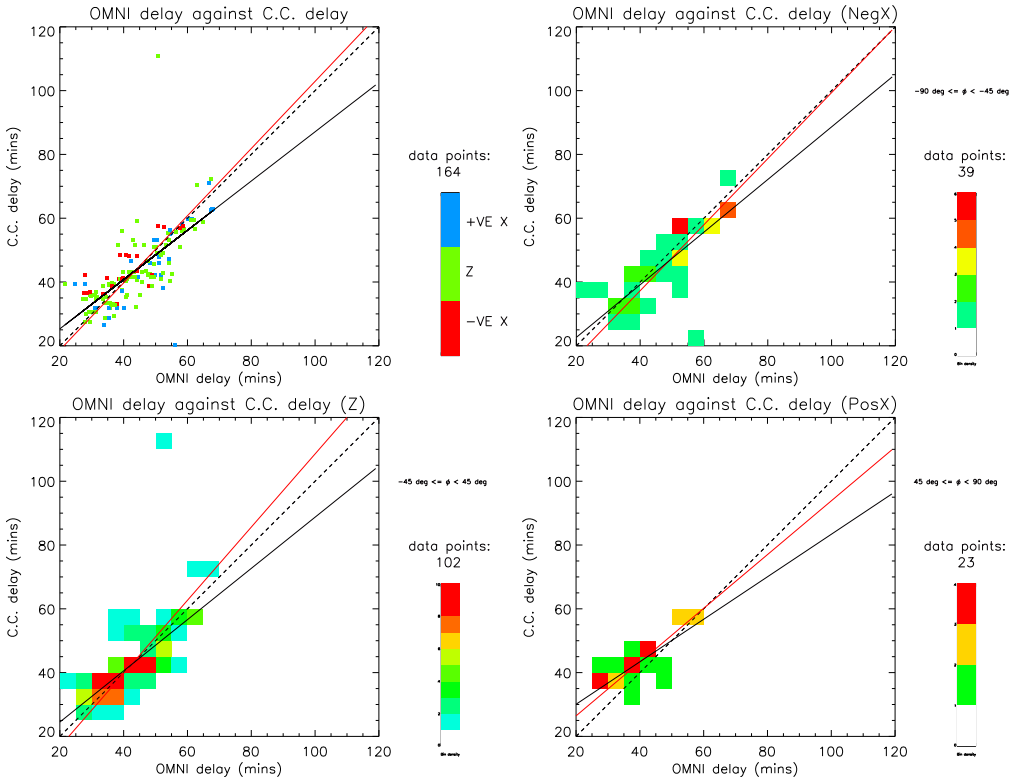

FIGURE 4.10: Delays represented by the decomposed solar wind cone angles (ϕ).

function on magnetic field data from ACE and Cluster-1. We required that Cluster was upstream of the bowshock at 15 R_E from Earth (in the GSE x-direction) and that the on-board CIS instrument recorded ion temperatures of below 1keV. Two further quality conditions filtered out those delays whose correlation profiles were deemed to be of poor quality and a least squares fit condition ensured that the resultant clock angle data mapped each other well.

Manual inspection of the data, and their resultant correlation profiles, revealed that the cross-correlation analysis worked best, i.e. provided distinct and substantial correlation peaks, when there was a distinct discontinuity in the IMF clock angle. Other studies, such as *Mailyan et al.* (2008), had primarily only considered such cases, though those events were chosen through manual filtering, resulting in far fewer delays calculated. However,

once our quality conditions were in place, our data set was subsequently reduced to a similar size as used by *Mailyan et al.* (2008).

With no conditions in place on the data there were 4938 calculated propagation delays, but when the quality controls were set at minimum correlation 0.6 and maximum threshold of 60% the usable data was diminished to 164 delays. Altering the minimum correlation had the greatest effect on the reduction in usable data by far, most likely because as the correlation of the peak increases the likelihood that it is a distinct peak should increase (if the time series is not periodic). There is, therefore, a trade-off between having a large data set and having a high quality data set.

Crooker et al. (1982) had previously applied the cross-correlation method to IMF measurements between ISEE 1 and ISEE 3. They determined that a coherence scale length of 90 R_E existed for magnetic structures embedded within the solar wind and that for separation distances greater than this scale length the quality of the correlation decreases substantially. Their findings agree well with other studies such as *Chang and Nishida* (1973) and *Sari and Valley* (1976), who also found coherence scales with a maximum length of 80 R_E and 150 R_E respectively. The separation distance between ACE and Cluster (~225 R_E) is far greater than any of those coherence scale lengths and so it is unsurprising that such a reduced number of delays is noticed at high correlation requirements.

In Figure 4.3, OMNI's 10 minute-averaged delay times were directly compared to the cross-correlation delay times, with no quality conditions in place, in the form of a density plot. There is considerable spread, especially at longer cross-correlation delays but correspondingly short OMNI delays. However, the densities of these bins is very low

and in most cases is less than ten delays per bin. Two possible scenarios exist to explain this: either OMNI underestimates those delays or the cross-correlation method has overestimated them.

A weighted least squares fit (shown as red on the plot) has a gradient of 1.18 ± 0.024 and intercept of -9.23 ± 0.05, whilst this may indicate an 18% difference in the gradient when compared to the $y = x$ line, owing to the intercept it only amounts to a maximum difference of the order of a couple of minutes from the $y = x$ line in the high density region. The distribution of the column means further indicate that the two methods agree particularly well in the very high density region (approximately 30-70 minutes) where all the means fit within 1 s.d. of the $y = x$ line. The relationship doesn't hold as well at longer OMNI delay times (> 80 minutes) since the column averages of the cross-correlation method do not increase.

When the quality constraints of minimum correlation coefficient 0.6 and maximum threshold of 60% are in place, as in Figure 4.4, the number of data points is reduced significantly and so too is the amount of spread in the data. Nearly all the column means are within 1 s.d. of the $y = x$ line and the weighted least squares fit is described by $y = (1.05 \pm 0.24)x - (2.39 \pm 0.14)$. There is no extended delay (> 80 minutes) region for either methods.

The flat delays are compared to the cross-correlation delays in Figure 4.5. Again, the spread is considerable, especially at longer delays. The weighted least squares fit gradient (red) is 0.66 ± 0.12 with an intercept of 16.3 ± 0.03, indicating that the cross-correlation method, in general, predicts longer delay times, especially in the extended delay region.

It could be that the flat delay underestimates the delay or that the cross-correlation function, in some case, overestimates it.

In Figure 4.6, the OMNI one-minute resolution delays are compared to the calculated flat delays. The gradient of the weighted least squares fit (red) is 0.73 ± 0.06 with an intercept of 12.95 ± 0.00 and the column means in the high density regions fit within 1 s.d. so, as with the previous two plots, the two sets of delays seem to agree well, with OMNI having a slight tendency to produce longer delays than the flat model in the extended delay region.

Since both OMNI and the cross-correlation method tend to estimate longer delay times than the flat model, it seems likely that the flat model underestimates the delay time (rather than the other two methods overestimating it) in the extended delay region. The flat model rarely predicts a delay which is longer than 80 minutes; whereas both OMNI and the cross-correlation method do so much more frequently.

The OMNI and the cross-correlation delays were then compared based upon the solar wind speed in Figure 4.7. There seems to be no effect on the relationship between the two methods based upon the speed of the solar wind. The lines of best fit in the fast solar wind have tilted away from the $y = x$ line, with a gradient of less than one, however, this is due to the "turning power" of an outlying point, rather than a real trend.

Figure 4.9 presents the OMNI and cross-correlation delays by clock angle in eight separate plots. The IMF clock angle dawn-dusk preference, a result of the Parker spiral, is clearly demonstrated in the density plots. There is a distinct lack of delays for northward pointing clock angles, a reduced number when compared east/west is expected due to

the Parker Spiral but it is unknown as to why there are considerably less than southward pointing clock angles. With the exception of the north-dawnward (for lack of data) and the north-duskward pointing clock angles, there is no significant difference between the relationship of the OMNI delays and the cross-correlation delays for different clock angles. The north-duskward clock angle plot shows a large spread in delays but there is no determinable reason known to us as why this spread should occur and may simply be a statistical anomaly.

The cross-correlation and OMNI delays, sorted by IMF cone angle, are presented in Figure 4.10. The cones angles are split into three directions: primarily pointing in the positive and negative GSE x-directions and primarily pointing somewhere in the GSE y-z plane. There is little difference between the three directions, suggesting that the IMF cone angle has no effect on the relationship between the two delay methods.

4.5 Conclusions

Our study has shown that statistically there is little difference in the delays calculated by OMNI, the cross-correlation method and the flat propagation model, however, there is often considerable spread in the compared delays. This indicates that, in general, the methods agree well; but, on occasion, the methods can produce delays which differ by over 30mins.

In Figure 4.11 the differences between the OMNI and cross-correlation delays are shown. The histogram shows that the vast majority of delays differ by less than 15 minutes, with two instances where the delays differ by over 30 minutes.

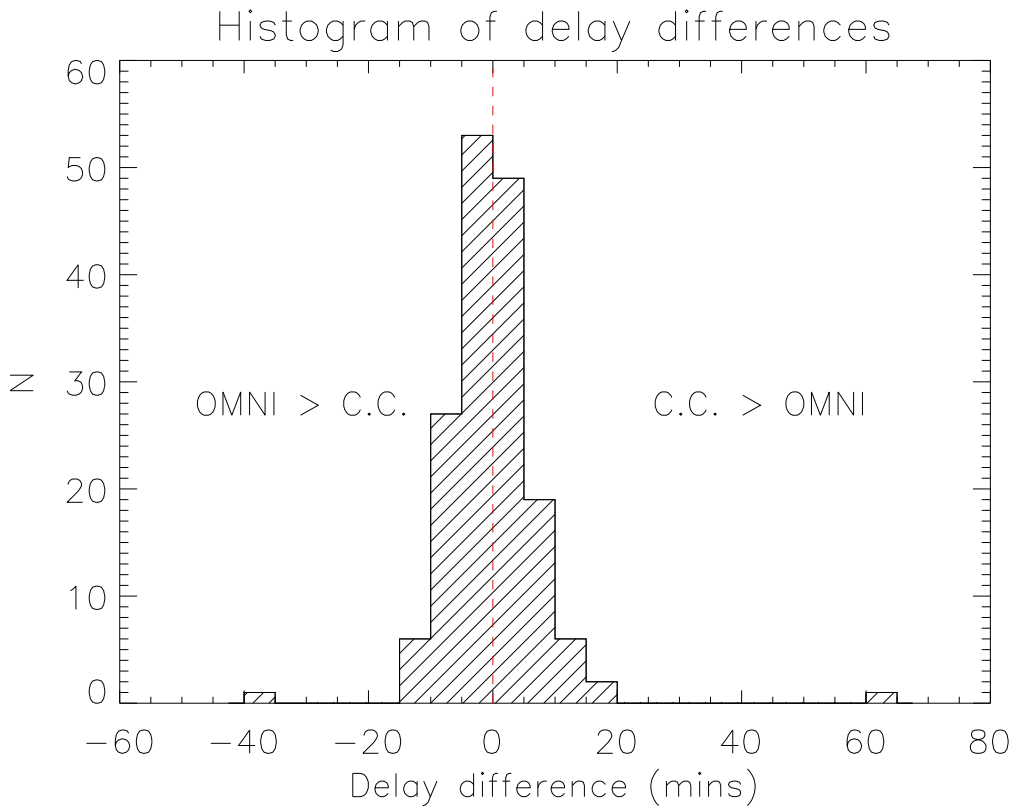

FIGURE 4.11: A histogram of the differences between the OMNI and cross-correlation delays.

The cross-correlation method uses data from ACE and Cluster to calculate its delay times directly, rather than through use of a model, and so is independent of many assumptions required when using a model, though some assumptions are needed, e.g. that the signal is effectively the same at both spacecraft and has simply propagated between them. If the cross-correlation method were flawless, it should be a true representation of the propagation delay, and if the OMNI delays were accurately calculated then it is logical to assume that they should, statistically at least, present very similar results to that of the cross-correlation method.

Interestingly, the flat propagation model produces very similar results also, especially for delays $\leq$ 80 mins. However, there is an extended delay region (or a "tail"), when

compared with the other two delay methods, for delays > 80 mins, indicating that the flat propagation model is too simple and fails to account for times of longer delay. Several studies have shown that delay times are affected by tilted IMF variations (e.g. *Weimer et al.* (2003)) and the tail could be the physical representation of this.

Of course, the cross-correlation method is not a definitive calculation for the delay time. Several factors affect the reliability of this method, most notably the separation distance between the first and second observers; which, in the case of ACE and Cluster, is a significant separation and one which, according to *Crooker et al.* (1982), is far greater than the correlation coherence length of the solar wind structures.

It is also noted that the distance not only in the GSE x-direction, but also in the y-direction may have a significant effect on the delays calculated as in this study no limits were set on the distance of Cluster, or ACE, from the Earth-Sun line. However, *Richardson et al.* (1998) had previously shown that correlation coefficients between ISEE 3 (at L1) and IMP 8 (in a circular orbit about the Earth) had little dependence upon the separation of the craft in the y-direction since the separation distance in the x-direction was much greater. In our periods of interest, Cluster's maximum deviation from the Earth-Sun line, in the y-direction, was $\pm$ 10 R_E whilst ACE's maximum deviation was $\pm$ 40 R_E whereas their separation in the x-direction was 225 R_E. It was therefore assumed that these deviations from the Earth-Sun line would not have the same impact as the x-direction separation distance.

The relationship between the cross-correlation and OMNI delays, at minimum correlation 0.6 and maximum threshold of 60%, is not affected by the orientation of the IMF; except, perhaps, for the North-Duskward clock angle where a greater spread was noticed; nor is

it particularly affected by the solar wind speed. This would seem to indicate that, since OMNI accounts for the IMF orientation in its estimations, via the PFN, and that we see no obvious difference with the cross-correlation, the PFN does indeed affect the delay time.

Unlike other techniques, the cross-correlation method does not require a discrete discontinuity in the IMF to calculate a delay time. However, clearly, for occasions where such discontinuities exist the cross-correlation delay is more likely to be representative of the true propagation delay, than for those occasions where the clock angle is almost constant ("flat"). Note that if the clock angle were indeed truly flat throughout the cross-correlation period, there would be perfect correlation for every delay time, which would be meaningless in this context.

The findings of this study can be summarised as follows:

1. The cross-correlation analysis provides a method to benchmark the propagation delays of the solar wind as it traverses from L1 to Cluster in the vicinity of the bow shock nose, as predicted by the OMNIweb service. Although the cross-correlation method does not rely on distinct discontinuities in the solar wind, it is likely to produce higher quality estimates when they are present.

2. When no quality controls on the correlation were in place, nearly 5000 delays were calculated from 10 years of ACE and Cluster data. However, when the data were constrained to reject ambiguous correlations, this amount diminished significantly to 164 delays.

3. With the constrained data, the OMNI and cross-correlation methods gave statistically similar results. However, we note that individual delays derived from the OMNI and cross-correlation techniques delays could differ by up to 50%.

4. Although equivalent delays computed by the two techniques can differ substantially, examination of prevailing upstream parameters revealed no solar wind/IMF control over the cross-correlation-OMNI relationship. Further investigation of those occasions where the delays differed substantially should therefore be undertaken to help improve the OMNI prediction process and/or the correlation method.

5. Based on these findings, we suggest that to determine the solar wind conditions during a period of interest, it is preferable to employ the use of a solar wind monitor just upstream of Earth at the bow shock. However, we acknowledge that this is not always possible and that the OMNIweb data products are convenient and provide statistically valid upstream parameters.

Chapter 5

The location of the Earth's magnetopause: a comparison of modelled position and in-situ Cluster data

This chapter is formed from the publication *Case and Wild* (2013).

Exploiting eight years of magnetic field data from the Cluster mission, in this chapter an automated magnetopause crossing detection routine is employed to determine the magnetopause location over varying magnetic latitude and local time. For a period spanning nearly one solar cycle a database of 2709 magnetopause crossings is built and compared to the magnetopause models of *Petrinec and Russell* (1996), *Shue et al.* (1998), *Dmitriev and Suvorova* (2000) and *Lin et al.* (2010). The detected locations are compared with

the predicted locations for a variety of solar wind conditions and positions on the magnetopause. It is found that, on average, the *Petrinec and Russell* (1996) and *Shue et al.* (1998) models overestimate the radial distance to the magnetopause by $\sim$1 R_E (9%) whilst the *Dmitriev and Suvorova* (2000) and *Lin et al.* (2010) models underestimates it by 0.5 R_E (4.5%) and 0.25 R_E (2.3%) respectively. Some varying degree of control on the differences between the predicted and encountered locations, by the solar wind and location parameters, are found.

5.1 Introduction

The accurate determination of the size and configuration of the magnetosphere is acutely important when investigating interactions between the interplanetary and near-Earth space environments. Understanding how the solar wind and interplanetary magnetic field (IMF) constrains the Earth's magnetosphere requires accurate specification of the magnetopause location under a variety of conditions.

Chapman and Ferraro (1931) first introduced the concept of a magnetopause whose shape and size is dependent upon the solar wind dynamic pressure (P_d). Since then, several empirical models have been developed to describe the shape and location of the magnetopause based on *in situ* satellite measurements. Examples include *Fairfield* (1971), *Roelof and Sibeck* (1993), *Petrinec and Russell* (1996), *Shue et al.* (1997) and *Suvorova et al.* (1999). The accuracy of such models can be assessed further by comparing the predicted magnetopause position with spacecraft observations of the boundary not included in the original modelling process (e.g. *Shue et al.* (1998), *Šafránková et al.* (2002) and *Dmitriev et al.* (2011)).

Although it is possible to survey the magnetopause location via changes in the observed magnetic field and plasma characteristics at a spacecraft, the boundary can vary in thickness from around 400-700 km (*Berchem and Russell*, 1982) and, depending upon a spacecraft's trajectory, it may pass through the boundary rapidly (∼seconds) or skim along the magnetopause passing in and out in multiple times in quick succession over a longer period (∼hours).

Manual determination of a magnetopause crossing can be a labour-intensive task requiring the identification of discontinuities in magnetic field data, plasma data or both. In a large scale survey, with hundreds or thousands of potential crossings, this can become impractical and an effective automated routine is desirable. Such an automated method would need to exploit a clearly-defined set of criteria to determine what physical parameter changes constitute a boundary crossing event over an appropriate spatial and temporal timescale.

In this study, a modified version of the *Ivchenko et al.* (2000) automated magnetopause crossing routine is applied to ∼8 years of magnetic field data from the Cluster mission to determine the location of the magnetopause. The detected crossings locations are then compared to the commonly-used magnetopause models of *Petrinec and Russell* (1996), *Shue et al.* (1998), *Dmitriev and Suvorova* (2000) and *Lin et al.* (2010).

Petrinec and Russell (1996) presents a cylindrically symmetrical empirical magnetopause model based on data from the ISEE satellite missions (*Song et al.*, 1988) and is an amalgamation of two earlier models: *Petrinec et al.* (1991) and *Petrinec and Russell* (1993). *Petrinec et al.* (1991) modelled the dayside magnetopause using a best fit ellipsoid function to ISEE 1 and 2 magnetopause crossings; *Petrinec and Russell* (1993) used magnetic

pressure balancing of the magnetopause to infer the location of the magnetotail. *Petrinec and Russell* (1996) then combine these two models with a smooth connection at the terminator.

The *Petrinec and Russell* (1996) model ignores non-axisymmetric functions on the dayside magnetopause (including the magnetic cusp regions). It has a range of validity for the input parameters of -10 $< B_z <$ 10 nT and 0.5 $< P_d <$ 8 nPa and has different modelling parameter values based upon the sign of B_z.

The *Shue et al.* (1998) model is an improved version of the earlier *Shue et al.* (1997) model which was derived as an empirical best fit to data from several magnetospheric satellites, including ISEE 1 & 2 and IMP 8. After further testing with a magnetic cloud event in 1997, in which the magnetopause passed inside geosynchronous orbit, *Shue et al.* (1998) improved the functional forms of the *Shue et al.* (1997) model to better represent the effect of P_d on the flaring angle and of B_z on the subsolar stand-off distance. As with *Petrinec and Russell* (1996), the *Shue et al.* (1998) model is cylindrically symmetric and does not account for the magnetospheric cusp regions.

The previous two models are both 2-dimensional and empirically derived using two input parameters: the magnetic field component B_z and the solar wind dynamic pressure (P_d) as these two parameters have been found to be significant in modelling the magnetopause location by many previous studies (e.g. *Petrinec et al.* (1991), *Sibeck et al.* (1991) and *Roelof and Sibeck* (1993)). *Dmitriev and Suvorova* (2000), however, used an Artificial Neural Network (ANN) to develop a complex, multi-parameter, 3-D model of the magnetopause.

Dmitriev and Suvorova (2000) employ the selection criteria developed by *Kuznetsov and Suvorova* (1997) on dayside magnetopause crossings from *Roelof and Sibeck* (1993) and geosynchronous crossings from *Kuznetsov and Suvorova* (1997) to build a data set of 999 magnetopause crossings (assuming a mirrored symmetry in the ecliptic plane) to input into the ANN model. Initially, 30 different parameters were included in the model, however, *Dmitriev and Suvorova* (2000) were able to reduce the number of required inputs to five parameters (λ - the GSE latitude , φ - the GSE longitude, B_y (GSM), B_z (GSM) and $\ln[P_d]$) whilst keeping a model correlation accuracy of 0.92 and a standard deviation of 1.04 R_E (*Dmitriev and Suvorova*, 2000). The *Dmitriev and Suvorova* (2000) model is asymmetric in the dawn-dusk plane.

With the ANN model there are several validity ranges on the input parameters, which *Dmitriev and Suvorova* (2000) state should keep the relative error under 10%. The longitude and latitude (GSE) should be between $\pm$ 90 degrees and $\pm$ 80 degrees respectively. The magnetic field components should be between: -20 $< B_y <$ 20 nT and -20 $< B_z <$ 20 nT and the dynamic pressure should be between 0.5 $< P_d <$ 40 nPa.

Lin et al. (2010) present a three-dimensional asymmetric magnetopause model which is built upon the *Shue et al.* (1997) magnetopause model. In addition to exploiting the solar wind dynamic pressure and the B_z component of the IMF as model parameters, the *Lin et al.* (2010) model also takes into account the solar wind magnetic pressure (P_m) and the Earth's magnetic dipole tilt angle (ϕ).

The *Lin et al.* (2010) model was developed using 980 magnetopause crossings from a range of satellite missions (including Geotail, IMP and Cluster) with 5 minute averaged solar wind parameters and 1482 Hawkeye magnetopause crossings with hourly solar wind

parameters. Using the Levenberg-Marquardt method for non-linear multi-parameter fitting, *Lin et al.* (2010) determine the important control parameters for the magnetopause size and shape and the relationships between them.

Unlike most magnetopause models, including *Petrinec and Russell* (1996) and *Shue et al.* (1998), the *Lin et al.* (2010) model is able to account for the north-south asymmetry of the magnetopause and for the indentations near the magnetic cusps and so should provide more accurate results in these regions.

In the sections that follow, we discuss how we utilize the *in situ* magnetic field data and how we modify the *Ivchenko et al.* (2000) magnetopause crossing detection routine to determine the location of the magnetopause for eight years of satellite data. We then compare our results to the models previously described.

5.2 In Situ Magnetic Field Data

The four European Space Agency (ESA) Cluster spacecraft have been in an elliptical polar orbit around the Earth since 2000. During the northern hemisphere's winter months the spacecraft pass through the dayside magnetopause on their outward trajectory from perigee to apogee. Over the mission lifetime, the orbital configuration has varied resulting in encounters with the magnetopause over a wide range of latitudes and at varying local times, due to the Earth's orbit about the Sun. The wide range of latitudes accessible to Cluster is in contrast to some earlier studies (e.g. *Ivchenko et al.* (2000) and *Dušík et al.* (2010)) that focussed on spacecraft measurements at low latitudes.

The magnetic field data are collected by each spacecraft's FGM instrument which consists of two three-axis fluxgate magnetometers (*Gloag et al.*, 2010). The FGM data used in this study are obtained from the Cluster Active Archive (see *Laakso et al.* (2010)) at four second resolution and are presented in this paper in the GSM co-ordinate system. Magnetic field data are used exclusively, rather than in combination with plasma data, as they are one of the most commonly available spacecraft data sets (both for Cluster and other missions).

Solar wind data, which are required as an input into the models, are obtained from the OMNIweb service (http://omniweb.gsfc.nasa.gov) at one minute resolution and are then averaged to five minute resolution, as in *Shue et al.* (1997). This"High Resolution OMNI" data set contains an interspersal of ACE, Wind, IMP 8 and Geotail data which have been time-shifted to the bow shock nose. The solar wind data are averaged to five minute resolution since it is unclear how quickly the magnetopause responds to changing solar wind conditions and the averaging also removes any ambiguity due to the lagging process through the magnetosheath. Additionally, propagation times across the magnetosheath are ∼4 mins (e.g. *Khan and Cowley* (1999) and *Wild et al.* (2009)) and so this averaged data is generally representative of the conditions at the magnetopause.

5.3 Methodology

We base our magnetopause crossing selection criteria on those of *Ivchenko et al.* (2000), whose detection routine was applied to two and a half years of three-second resolution magnetic field data from the Geotail mission. The four *Ivchenko et al.* (2000) criteria for the determination of a crossing are:

1. the transition across the magnetopause should be completed within 30s;

2. the standard deviation of the magnetospheric magnetic field is required to be less than 40% of the magnetic field on the magnetosheath side of the assumed boundary;

3. the northward component of the magnetospheric magnetic field is required to exceed 10 nT and;

4. the northward component of the magnetospheric magnetic field is required to be at least a factor of 1.3 times greater than the corresponding magnetosheath component.

Since Geotail only encountered the magnetopause in a narrow range of latitudes, around ± 2 R_E from the GSM-x axis (typically in a skimming-type configuration) (*Nishida*, 1994), whereas Cluster passes through the magnetopause at a range of latitudes, the *Ivchenko et al.* (2000) criteria require modification. Specifically, *Ivchenko et al.* (2000) consider the difference in the northward component of the magnetic field (B_z) either side of the magnetopause boundary. This generally works well except in the following two cases: (1) when the IMF is primarily orientated northward, in which case the B_z component of the magnetic field is similar in both the magnetosheath and magnetosphere, and (2) at high latitudes, where B_z tends to zero as the magnetic field is directed primarily toward/away from the Earth (in the cusp region this changes with B_z once again becoming dominant but now in the opposite direction). Case (1) is somewhat difficult to account for, but to account for case (2): at high latitudes (where the angle

between the spacecraft position in the GSM x-y plane is greater than 45 degrees) we instead use the radial component of the magnetic field (B_r).

Data from all four Cluster spacecraft between 2002-2010 are analysed and, using the modified *Ivchenko et al.* (2000) criteria, magnetopause crossings are detected. To reduce data processing time, we focus on time intervals centred on the predicted magnetopause crossings as given in the Cluster predicted events catalogue (*Hapgood et al.*, 1997). In order to avoid a bias toward finding the magnetopause in close proximity to where the Cluster planning software (which employs the *Sibeck et al.* (1991) magnetopause model) predicts it will be located, we examine data from a four hour window. Over this window, the spacecraft typically travel a distance of $\sim 5\ R_E$. We thus expect to capture virtually all potential magnetopause crossings.

For determination of a magnetopause crossing, we employ a running average method on the four hour window of magnetic field data. Two three minute segments of magnetic field data, separated by a 32 second gap, are selected and tested against the following modified *Ivchenko et al.* (2000) crossing criteria. If a crossing is not encountered then the two segments of data chosen are shifted along in time by four seconds, however, if a crossing is encountered then the segments chosen are shifted forward by 10 minutes. All criteria must be met for a crossing to be determined.

1. The transition across the magnetopause boundary should be completed within 32 seconds (equivalent to eight spins of the Cluster spacecraft). The time of the crossing event is recorded as when the spacecraft first crosses into the boundary

layer and so by enforcing this transition time limit we ensure that the recorded time of crossing is accurate.

2. Multiple magnetopause crossings should not occur within 10 minutes. Multiple crossings may occur when the spacecraft is skimming the magnetopause or when the magnetopause location is rapidly fluctuating; rather than having multiple crossing events, we instead choose the first event to represent the crossing location.

3. The standard deviation of the three minute window of magnetosheath magnetic field must be greater than 4.5 on average and it must be a factor of 2.5 times larger than the standard deviation of the three minute window of magnetospheric magnetic field. This criteria requires that the magnetic field observed in the magnetosheath is fluctuating by a larger amount than the magnetospheric magnetic field.

4. At low latitudes the B_z, and at high latitudes the B_r, component of the magnetospheric magnetic field must be greater than 10nT, since we take this to be a conservative estimate of the minimum terrestrial magnetosphere field strength.

5. The particular magnetospheric magnetic field component, as determined by criteria (4), must be a factor of at least 1.3 times greater than the corresponding magnetosheath magnetic field component. Although this may rule out occasions where the orientation of the IMF is similar of that to the magnetosphere, this factor was determined to be most appropriate in preventing small changes in the magnetic field from registering as crossing events.

An example of a magnetopause encounter is shown in Figure 5.1. The three panels on the left of the figure present magnetic field data from Cluster 1 showing the overall magnetic field strength $|B|$, the appropriate magnetic field component (in this case B_r), the three minute running standard deviation of $|B|$, and the clock angle of the measured magnetic field, respectively. The clock angle is defined as the arctangent of the ratio of the y- and z-components of the magnetic field (see equation 4.2) and is shown as measured at Cluster (yellow) and the equivalent parameter predicted at the bowshock by OMNIweb (blue). The dashed vertical black line in the left panel indicates the time at which the Cluster predicted events catalogue suggested a crossing would occur; the dashed red line indicates the time at which the automated routine detected a crossing. The panel on the right of the figure shows the Cluster spacecraft's position and a Tsyganenko-96 magnetic field model magnetosphere in GSE co-ordinates. The modelled magnetosphere is determined for the time of the detected crossing and is projected into the GSE X-Z plane (i.e. at $\mathrm{Y}_{GSE} = 0$).

5.4 Results and Discussion

In total, 2709 crossings were detected using the automated routine described above, reducing to 2640 useful crossings due to missing/bad data in the OMNIweb database. This value is significantly less than 7418 predicted crossings listed in the predicted events catalogue, however, this was to be expected since our selection criteria are somewhat conservative.

The locations of these crossings are shown in Figure 5.2. The four panels in Figure 5.2 represent different co-ordinate planes (from top left to bottom right): the noon-midnight

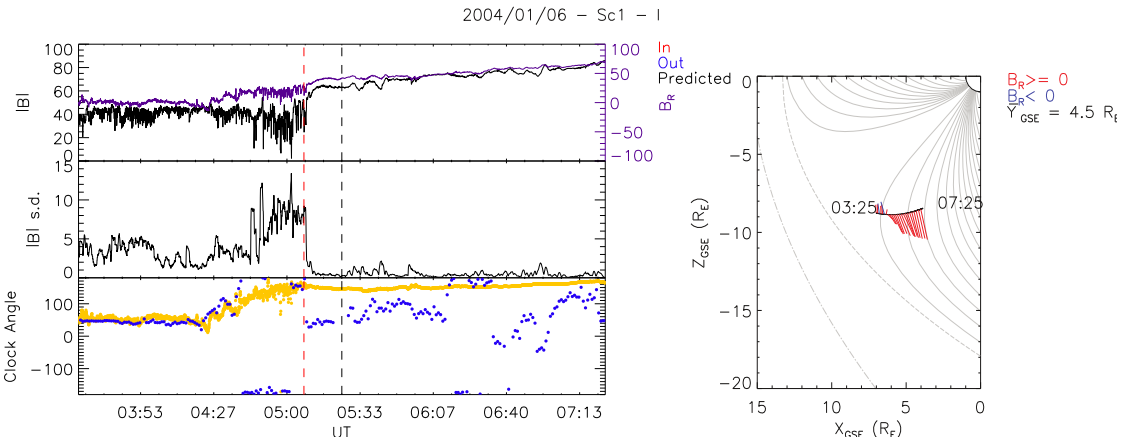

FIGURE 5.1: An example of the plots produced by the crossing detection routine. The three panels on the left of the figure present the magnetic field data (the magnetic field strength $|B|$ (black) and chosen magnetic field component which is B_r in this case (purple), the running standard deviation of a three minute segment of the magnetic field strength, and the clock angle (measured with Cluster in blue and predicted by OMNIweb in yellow). The red dashed line indicates a detected inward crossing; the black dashed line indicates the time the spacecraft were predicted to cross the magnetopause. The panel on the right shows the spacecraft position and a modelled magnetosphere for the time of the crossing (in GSE co-ordinates).

meridian of the magnetosphere (with the Sun off to the left-hand side of the plot), a projection of the GSM equatorial plane from above the magnetic North Pole, a view of the Earth from the direction of the Sun and a projection onto the y-z plane of the radial distance to the magnetopause from the Earth as a function of X_{GSM} position.

Cluster's encounters with the magnetopause were detected over almost a full 180 ° range of latitudes with particularly high density regions at ± 10 R_E in the z-axis and over local times of 0900-1500 due to Cluster's orbital configuration.

The detected crossing locations were compared with the predicted magnetopause locations for each of the four models discussed in the Introduction. The steps involved in calculating the radial separation distance (Δr) between the spacecraft location and the modelled magnetopause location are as follows. Firstly, we define the separation distance as the radial location of the spacecraft subtracted from the radial location of the

magnetopause:

$$\Delta r = r_{mp} - r_{sc} \tag{5.1}$$

where r_{sc}, the radial distance to the spacecraft, is defined as the length of the vector drawn from the Earth to the spacecraft location in the x-ρ plane:

$$r_{sc} = \sqrt{{x_{sc}}^2 + \rho^2} \tag{5.2}$$

where ρ is the length of the spacecraft position vector in the y-z plane:

$$\rho = \sqrt{{y_{sc}}^2 + {z_{sc}}^2} \tag{5.3}$$

and where r_{mp} is the radial distance to the modelled magnetopause, as determined individually for each model at spacecraft angle θ, the latitude in the x-ρ plane:

$$\theta = \arctan\left(\frac{\rho}{x_{sc}}\right) \tag{5.4}$$

where x_{sc}, y_{sc} and z_{sc} are the spacecraft's location in GSM x, y and z components.

Due to the validity limitations on the input parameters of the models we were able to compare 2599 crossings to the *Petrinec and Russell* (1996) model and 2621 crossings to the *Dmitriev and Suvorova* (2000) model. All 2640 crossings were compared against the *Shue et al.* (1998) and *Lin et al.* (2010) models since no parameter restrictions were specified.

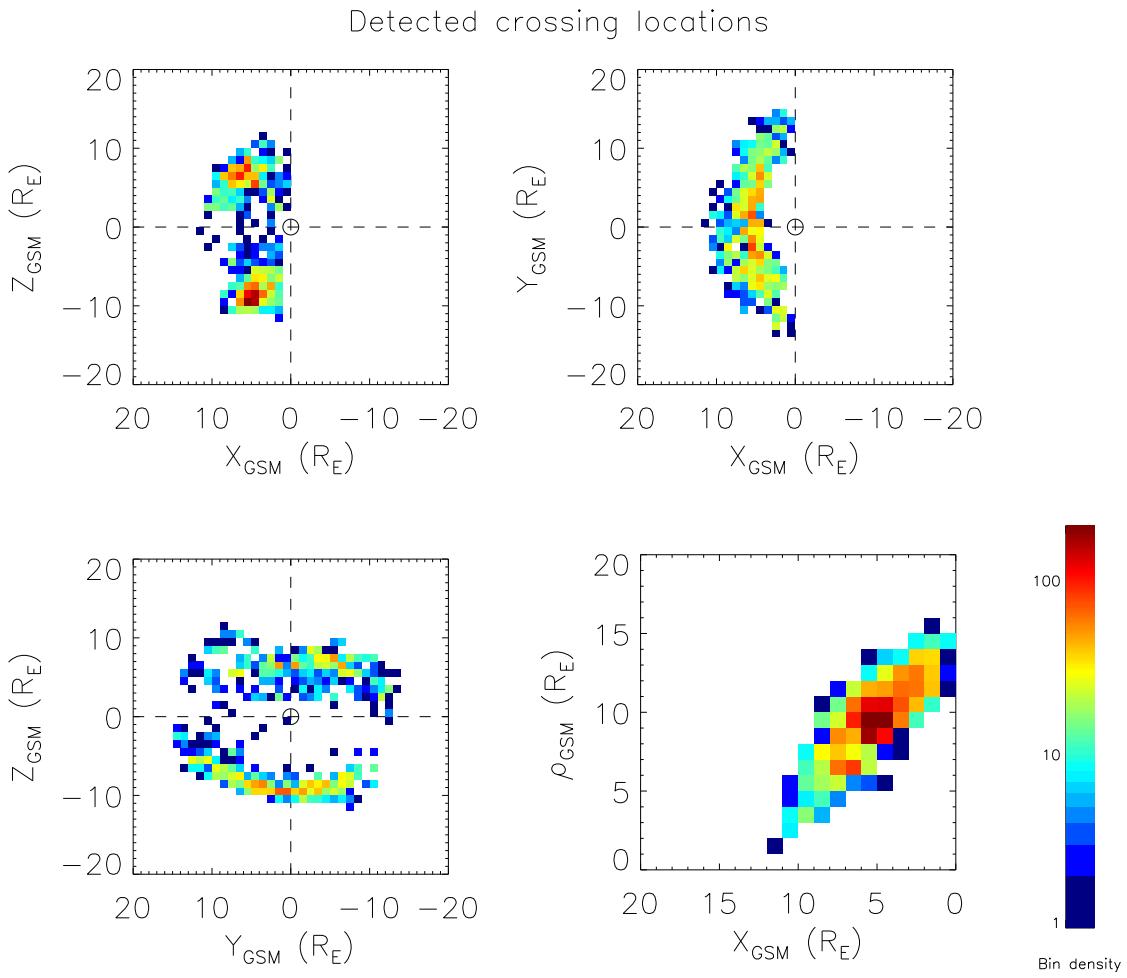

FIGURE 5.2: A density plot of detected magnetopause crossings locations in GSM coordinates. Position ρ is defined as $\sqrt{{Y_{GSM}}^2 + {Z_{GSM}}^2}$ (see equation 5.3 for further details). The density of each bin is represented by the logarithmic colour scale.

Figure 5.3 compares the location of the *Petrinec and Russell* (1996) model magnetopause to the crossings detected by Cluster using the technique described above. The median difference in the radial location is found to be 1.06 R_E, with the positive value indicating that the modelled magnetopause location is typically radially further from the Earth than the detected location. The histogram is generally symmetrically distributed about the median.

Figure 5.4 is a comparison between the *Shue et al.* (1998) model and our detected crossings. We find that the median difference is 1.48 R_E, again indicating that the median

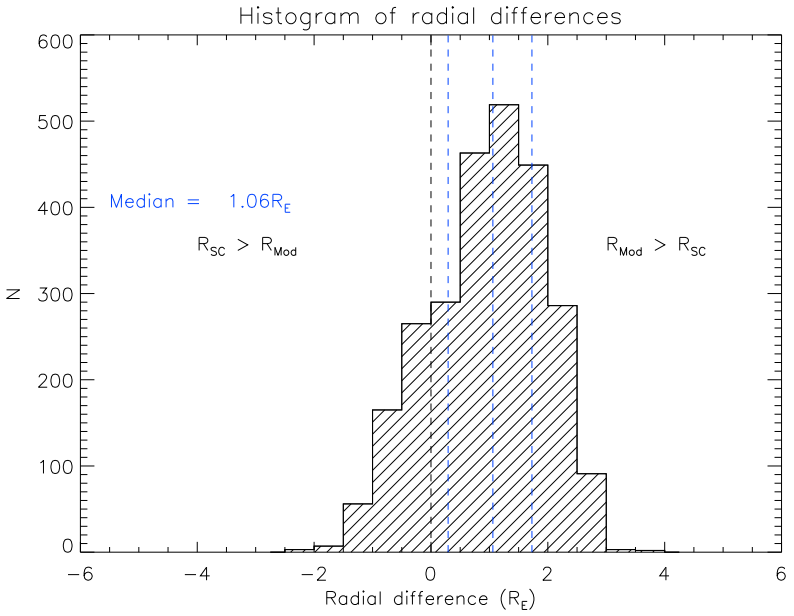

FIGURE 5.3: A histogram of the radial differences, as calculated in equation 5.1, between the detected crossing location and the *Petrinec and Russell* (1996) modelled magnetopause location. The three vertical dashed blue lines represent the lower interquartile, the median and the upper interquartile respectively.

modelled location was radially further out from the Earth than the detected location. The histogram is symmetrical around the median, though with a greater spread than with the *Petrinec and Russell* (1996) model.

The detected crossing locations and the *Dmitriev and Suvorova* (2000) modelled magnetopause locations are compared in Figure 5.5. The median difference between the model and the detected crossing locations is -0.52 R_E, which, opposite to the previous two models, shows that the median modelled location was radially closer to the Earth than the detected crossing location. The difference distribution is non-symmetrical with a substantial tail, of approximately 250 (10%) events, at radial differences of -3 to -6 R_E.

In Figure 5.6 the detected and predicted crossing locations are compared for the *Lin et al.* (2010) model. The median difference is -0.24 R_E which, as with the *Dmitriev and Suvorova* (2000) model, suggests that, in general, the *Lin et al.* (2010) model slightly

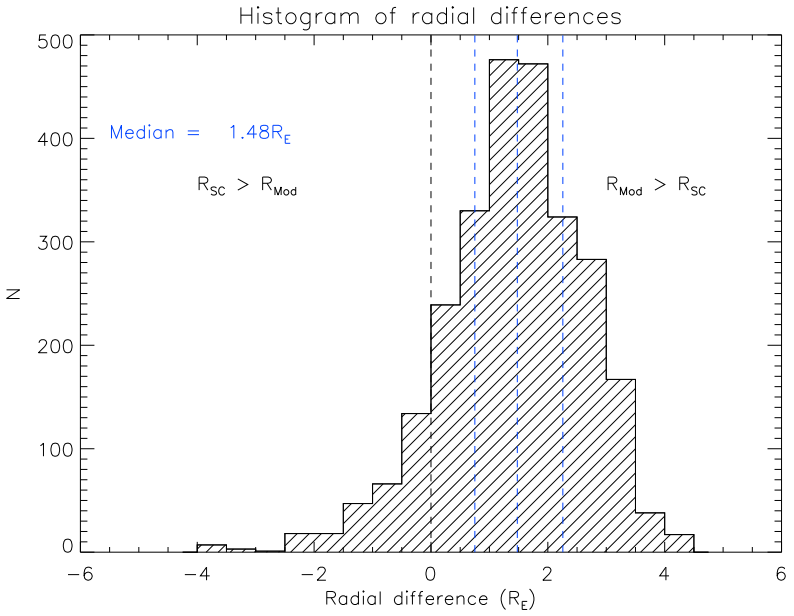

FIGURE 5.4: A histogram, of the same form as Figure 5.3, for the *Shue et al.* (1998) model.

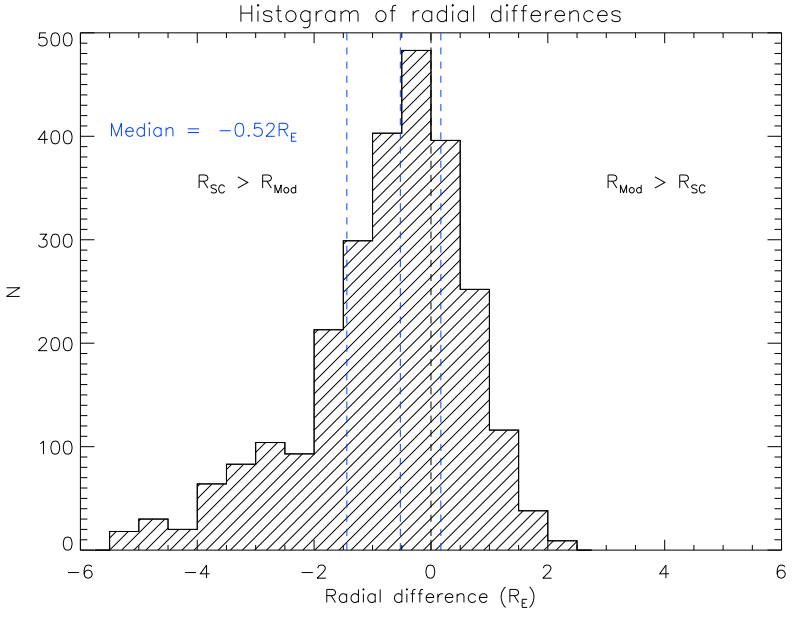

FIGURE 5.5: A histogram, of the same form as Figure 5.3, for the *Dmitriev and Suvorova* (2000) model.

underestimates the distance to the magnetopause. The distribution of differences is similar to the *Dmitriev and Suvorova* (2000) distribution but with a smaller tail region (approximately 5% of events). Over half of the data lie within ± 1 R_E.

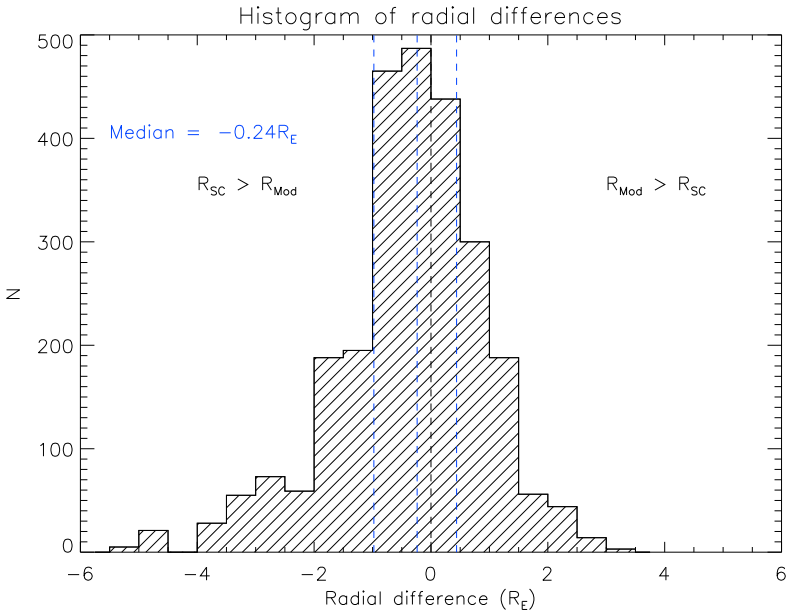

FIGURE 5.6: A histogram, of the same form as Figure 5.3, for the *Lin et al.* (2010) model.

The radial differences between the detected crossing locations and the four models are shown for four parameters (clock angle, B_z, P_d and θ) in Figure 5.7. The number of crossings are represented by the colour-scaled density bins. The crosses indicate the median value for the row of bins and the error bars represent the standard deviation of the distribution in each row.

The clock angle has little or no influence on the radial difference for any of the models. There is little apparent relationship between the radial differences of the modelled and observed magnetopause locations and B_z for the *Petrinec and Russell* (1996) model. At B_z<4nT, the radial differences for the *Shue et al.* (1998) model decrease from around 2 R_E to around 0 R_E. The *Dmitriev and Suvorova* (2000) and *Lin et al.* (2010) model plots have a similar form as the *Shue et al.* (1998) plot but are off set by about -2 R_E. Approximately 11% of the data fall below a B_z value of less than -4nT.

With the P_d parameter, there is some small dependence of the radial difference for the

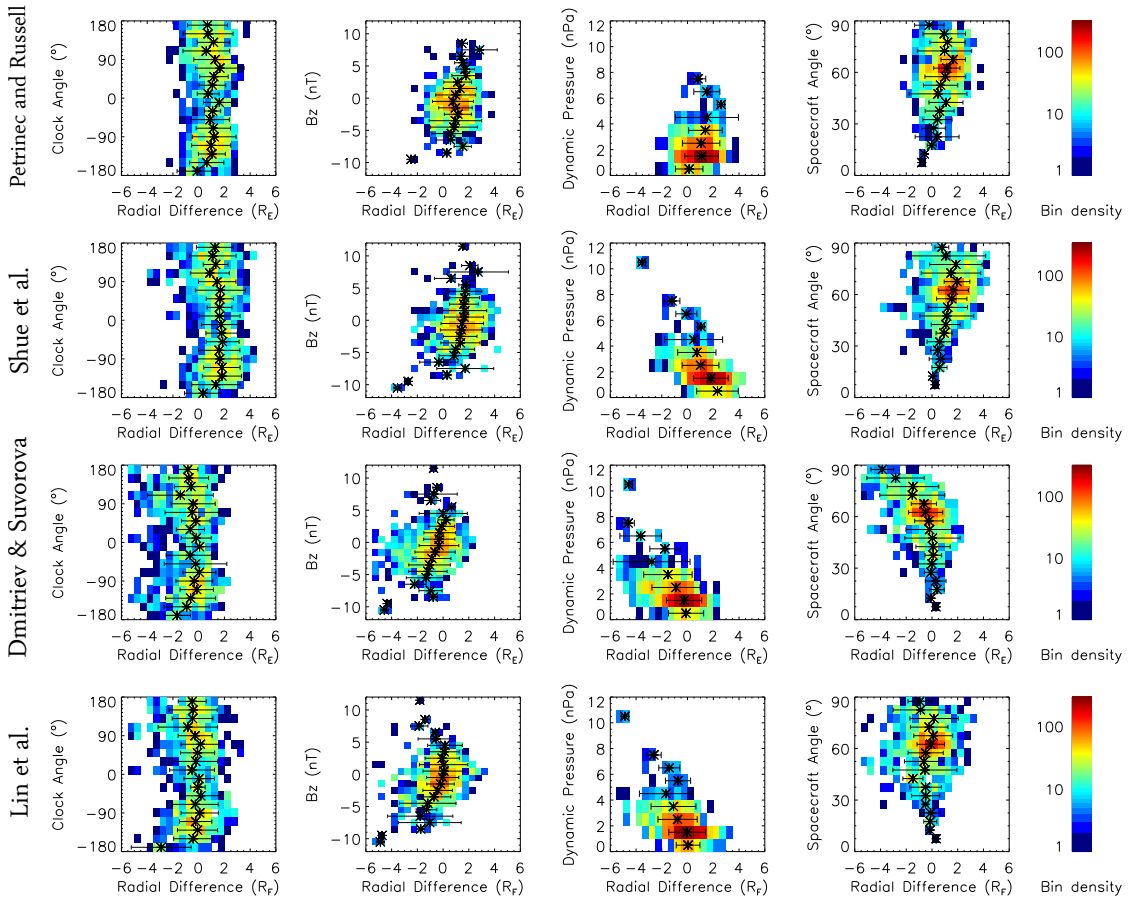

FIGURE 5.7: A comparison of the radial difference between the detected magnetopause location and the modelled locations for each of the three models, plotted for the four parameters (clock angle, B_z, P_d and spacecraft angle θ). The density of the bins is represented by the logarithmic colour bar. The median radial difference for each row is denoted by the cross and the error bars represent the interquartile range of the row.

Petrinec and Russell (1996) model. At larger P_d, the radial differences for the *Petrinec and Russell* (1996) model increase, however, the opposite is true for the other three models. As P_d increases, the radial differences decrease for the *Shue et al.* (1998) model and become increasingly negative for the *Dmitriev and Suvorova* (2000) and *Lin et al.* (2010) models.

The spacecraft angle, θ, has a small influence on the radial difference, with increasing radial differences at increasing spacecraft angles (i.e. at high latitudes), for both the *Petrinec and Russell* (1996) and *Shue et al.* (1998) models. A more pronounced, but

opposite, effect is noticed with the *Dmitriev and Suvorova* (2000) model where increasing spacecraft angle results in an increasingly negative radial difference. The radial differences for the *Lin et al.* (2010) model do not seem to be affected by the spacecraft angle.

The primary aim of this study was to as to use an automated routine, rather than manual inspection, to determine crossing events and then compare these events to the magnetopause models. However, to ensure that the results presented are statistically valid, and not the product of an erroneous automated routine, we conducted a sample study on the results. A random sample totalling 20% of the data was manually analysed and any false crossing identification events were removed. Of the 528 random events, 341 were identified as accurate crossing events. These were then plotted and compared to the main plots and, with the exception for dynamic pressure for the *Dmitriev and Suvorova* (2000) and *Lin et al.* (2010) models, we found similar distributions for all; see Figure 5.8 for the comparison of the medians from the full population and from the sample.

On inspection of those events where the routine had identified a crossing yet no such crossing had occurred, we found that most events had only just qualified under our criteria. Increasing the magnitude of the discontinuity in the magnetic field data required to determine a crossing would help eliminate these false positives further but would also severely impact the total number of accurate magnetopause crossing detections.

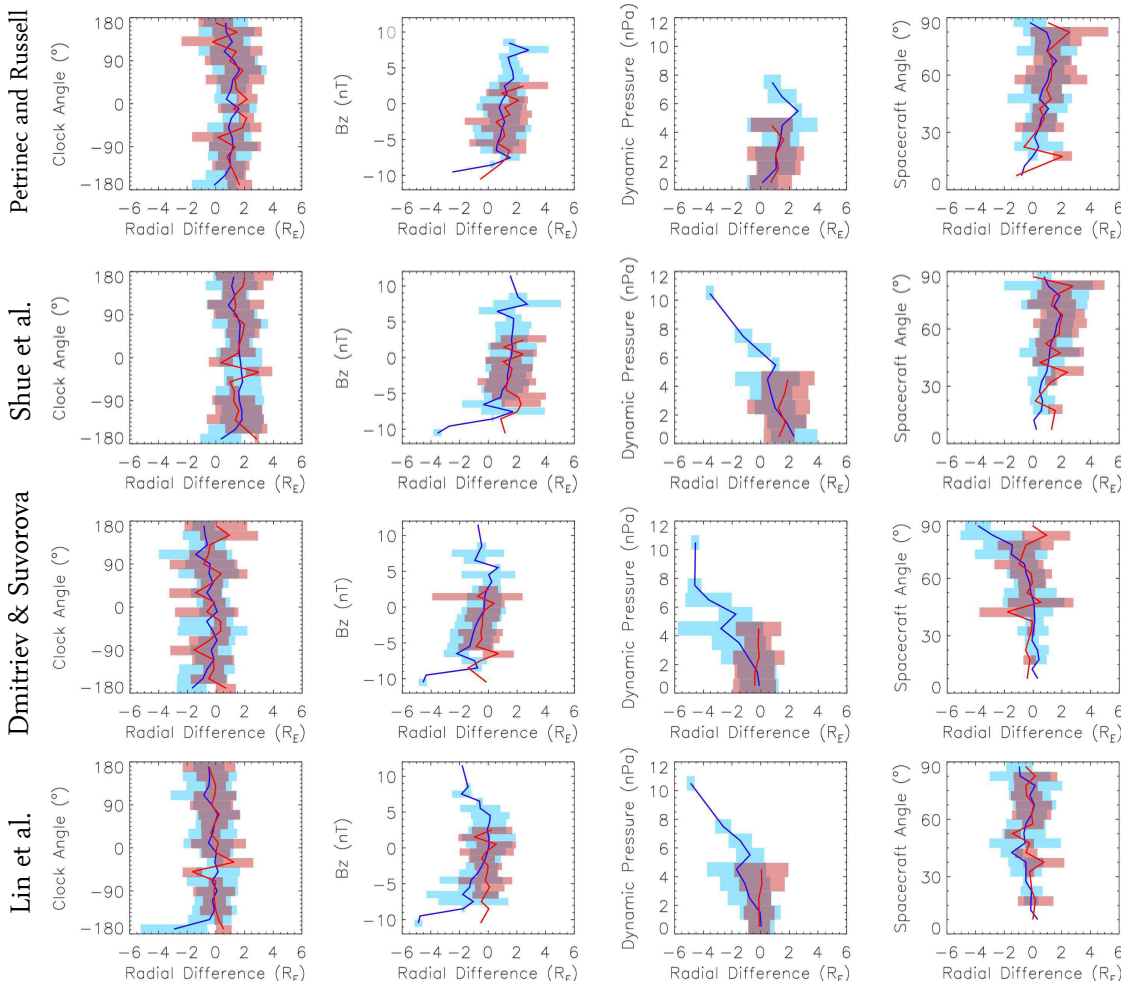

FIGURE 5.8: A comparison of the medians for the full population (blue) and the 20% sample (red), plotted again for the four parameters (clock angle, B_z, P_d and spacecraft angle θ). The solid lines indicate the median value for the row and the lightly shaded areas represent the interquartile range of each row.

5.5 Summary

In this investigation, we created a more generalized version of the *Ivchenko et al.* (2000) magnetopause crossing detection routine to explore its application at higher latitudes. After applying our modified criteria to 8 years of Cluster magnetic field data we have identified 2709 crossings of which we were able to compare 2640 crossings to four models: two commonly used 2-D empirical models, one 3-D ANN model and one asymmetric empirical 3-D model.

We find that the two empirical 2-D models, *Petrinec and Russell* (1996) and *Shue et al.* (1998), generally agree well with each other. They both produce similar median differences and interquartile ranges, when compared to our detected crossing locations, though this is perhaps not unexpected since when *Shue et al.* (1998) compared their model with that of *Petrinec and Russell* (1996) they found that the two models generally correctly predicted dayside magnetopause crossings (the major differences occurring in the flanks). Additionally, both models were developed using very similar datasets and so one might expect similar results when using these models.

The radial differences between the detected crossing locations and the *Petrinec and Russell* (1996) and *Shue et al.* (1998) modelled locations are off set about a median of just over 1 R_E. This indicates that, in general, the models over-estimate the radial distance to the magnetopause (by about 9%). There are a couple of reasons for why this may be the case. Firstly, the vast majority of the data in their crossing databases were obtained using near-equatorial satellite missions (ISEE-1 & 2). It is now well known that, under the same external conditions, the magnetopause is greater in size in the equatorial plane than in the meridional plane (*Dmitriev and Suvorova*, 2000). Since these two models were based on low-latitude satellite missions, at middle latitudes where the magnetopause is flatter, they would tend to overestimate the distance to the magnetopause.

This assumption is strengthened when the differences between the modelled magnetopause locations of *Petrinec and Russell* (1996) and *Shue et al.* (1998) and the detected locations are compared with the spacecraft angle. The models agreed well with the detected locations at spacecraft angles (θ) of $< 40^\circ$ but there was an increase in the

difference at angles larger than this.

Secondly, the majority of the ISEE 1 & 2 data was collected during a period of of rising solar activity (1977-1979) which resulted in an increased frequency of co-rotating high-speed solar wind streams. The trailing edges of such solar wind streams are often accompanied by regions of quasi-radial IMF and it has been shown that, under such conditions, the magnetopause is expanded beyond its normal location (*Suvorova et al.*, 2010). Hence, in the case of *Petrinec and Russell* (1996) and *Shue et al.* (1998), who used large amounts of data from this period to build their models, we should expect that the models will overestimate the distance to the magnetopause during normal IMF conditions.

There was a clear trend in the radial difference between the detected location and the modelled locations of *Shue et al.* (1998), *Dmitriev and Suvorova* (2000) and *Lin et al.* (2010) when compared with solar wind dynamic pressure. For *Shue et al.* (1998), the differences range from a median of 2 R_E at $P_d < 1$ nPa through to -2 R_E at $P_d = 8$ nPa, with 0 R_E occurring at around 4 nPa. The distribution in Figure 5.4 closely matches that of *Dušík et al.* (2010) who compared 6649 THEMIS magnetopause crossings to the *Shue et al.* (1998) model, though we compare crossings over a much wider range of latitudes. For *Dmitriev and Suvorova* (2000) and *Lin et al.* (2010), there was a similar trend to *Shue et al.* (1998) but the data was distributed approximately -2 R_E from the *Shue et al.* (1998) distribution.

The median difference between the predicted and measured location of the magnetopause for the *Dmitriev and Suvorova* (2000) and *Lin et al.* (2010) models both suggest that the models underestimate the radial distance to the magnetopause by 0.52 R_E and 0.24 R_E

respectively whereas the other two models overestimate it: by 1.06 R_E for *Petrinec and Russell* (1996) and by 1.48 R_E for *Shue et al.* (1998).

As with many automated routines, we acknowledge that the modified *Ivchenko et al.* (2000) routine used in this study will not identify all crossings and that it may determine a crossing when no such event occurred. It does, however, provide a statistically valid approach to detecting crossings with a large-scale data set.

The *Ivchenko et al.* (2000) crossing criteria, and our modified version of them, are based purely on magnetic field data. Whilst this is convenient, since magnetic field data is the most commonly available, straightforward and reliable data set, it is well known that there are clear differences in the plasma characteristics between the magnetosheath and magnetosphere regimes. Indeed, some studies (e.g. *Hapgood and Bryant* (1990)) primarily use the plasma characteristics as the defining data set for determination of magnetopause crossings. Incorporation of plasma data criteria into the modified *Ivchenko et al.* (2000) crossing criteria requires further investigation.

In addition, we have used magnetic field data from the Cluster mission to determine the magnetopause location since the spacecraft encountered the magnetopause at varying magnetic latitude and local time. This was an improvement on other magnetopause studies, whose spacecraft often visited similar regions of space. Nevertheless combining data from multiple spacecraft missions, to increase spatial and temporal coverage, may prove to be a useful future exercise.

This study has performed a comparison between detected and modelled magnetopause locations as a way of testing the validity of these models. It would seem beneficial for

future studies to include the results of this study, specifically our detected locations, when building new or improved magnetopause models.

Additionally, we note that one may wish to determine the effect of upstream solar wind conditions on the magnetopause location (rather than just the difference when compared to a model). During the course of this study the detected magnetopause locations were plotted based upon the year in which the data was recorded (in a similar format to Figure 5.2) and based upon upstream conditions (in a similar format to Figure 5.7).

Unfortunately, due to changes in the mission's orbit and due to crossing the magnetopause in different places, it was difficult to draw any conclusions from these plots alone and so they were not included in this study. Further investigation, perhaps through mapping the crossings onto a modelled magnetopause and comparing the location of the nose of this modelled magnetopause for different years and different upstream conditions would therefore be a worthwhile exercise.

Chapter 6

Magnetic field draping through the magnetosheath

Previous studies have shown that as the embedded IMF traverses through the magnetosheath its orientation is modified through a process known as magnetic draping. Investigation of eight years worth of near-magnetopause magnetic field data, provided by the Cluster mission, is undertaken and the changes in magnetic field orientation are presented. We show that, over the course of 2,688 magnetopause crossings, the upstream IMF conditions have a considerable impact upon the amount of modification of the orientation of the magnetic field as does the location of the recording on the magnetopause. Overall, only 13% of data points exhibit "perfect draping" (where the clock angle is not substantially affected by the magnetosheath traversal).

6.1 Introduction

Embedded within the solar wind, a quasi-neutral plasma emitted from the Sun, is the interplanetary magnetic field (IMF). The IMF is "frozen-in" to the solar wind and will always move parallel to the plasma flow. As the solar wind extends out into the heliosphere, in a Parker spiral configuration, it encounters the obstacle of the Earth's magnetic field and flows around it and thus so must the embedded IMF. This changing orientation of the IMF is known as magnetic draping.

Being able to accurately determine the orientation of the magnetic field in the magnetosheath is important for many reasons. For example, almost all magnetopause models rely upon the magnetic field orientation in the magnetosheath when determining the shape and location of the magnetopause (see Chapter 5 for examples). Additionally, knowing the impinging magnetic field orientation is important when studying magnetic reconnection at the magnetopause and the processes which rely on it. Specifically, magnetic reconnection is one of the primary drivers for injecting energy and particle populations into the magnetosphere which in turn can lead to events such as magnetic storms and substorms (*Angelopoulos et al.*, 2008).

There are several models which aim to predict the effect of draping on the IMF. These include the "perfect draping" approximation (which assumes that the IMF clock angle is preserved through the bowshock and magnetosheath but makes no predictions for any changes in B_x), the gas-dynamic model of *Spreiter et al.* (1966) and the analytical magnetosheath model of *Kobel and Flückinger* (1994).

The gas-dynamic model of *Spreiter et al.* (1966) assumes that the bulk flow properties of the solar wind, as it passes by an impenetrable object, can be described through the hydrodynamics of a single-species gas and ignores any effect from magnetohydrodynamic (MHD) forces. The model is too simplistic for most cases, but tends to agree fairly well with observations under steady-state IMF conditions (*Luhmann et al.*, 1986). *Kobel and Flückinger* (1994) analytically solve the Laplace equation to produce a scalar potential which describes the draped IMF in a steady state. The *Kobel and Flückinger* (1994) model contains five physical parameters: the stand-off distances of the magnetopause and the bowshock, and the three IMF components.

It has been shown (e.g. *Coleman* (2005)) that all three of these models give rise to qualitatively similar results for the magnetic field in the magnetosheath and for the location of anti-parallel regions in the magnetopause - with the largest deviations occurring further away from the sub-solar point.

In this study, we use magnetic field data collected from OMNI (bowshock) and Cluster (magnetopause) to investigate how the IMF clock angle is affected by the traversal through the magnetosheath. Data are analysed through a period spanning nearly one solar cycle and are filtered based upon the IMF orientation.

6.2 Methodology

To study magnetic draping through the magnetosheath, one must observe the IMF just before it enters the magnetosheath and then again just before it encounters the magnetopause. There are several complicating factors which mean that this is not a

trivial exercise. Firstly, there is poor temporal resolution of spacecraft data in both the near-bowshock and near-magnetopause regions. Secondly, in addition to the poor temporal resolution, the task is further complicated by the fact that there must be a coincidence of both the near-bowshock and near-magnetopause data recorders. Finally, even if there is a data recorder in both regions of interest during the same time period, one must know how long it will take the IMF, embedded within the shocked solar wind, to travel through the magnetosheath so that the measurements taken at the data recorders can be temporally aligned and compared.

In this study, to maximize the amount of data available, the near-bowshock observer is not a single observer but rather a collection of observers whose data have been collated appropriately lagged to the bowshock. The data are provided by the high-resolution OMNIweb data service (http://omniweb.gsfc.nasa.gov) which contains an interspersal of data from the ACE, Wind, IMP 8 and Geotail missions. The near-magnetopause data is provided by the four satellites from the Cluster mission whose orbits, during the months of November through March, pass through the dayside magnetopause over a range of magnetic latitudes.

To determine exactly when the Cluster constellation is located in the magnetosheath near the magnetopause, the magnetopause crossing database created in Chapter 5 is used. This database is built using eight years of magnetic data from the Cluster mission where crossings are detected by comparing the spacecraft-measured magnetic field data to a set of crossing criteria. Using this database, it is then possible to determine a one-hour period where the Cluster satellites are located in the magnetosheath near the magnetopause. To ensure that no magnetopause data is included in this one-hour window, a 2 R_E buffer

is implemented between the spacecraft and magnetopause locations.

The time taken for the shocked solar wind to traverse the magnetosheath is variable and depends upon a range of factors; studies such as *Khan and Cowley* (1999) and *Wild et al.* (2009) have shown that the transition time through the sheath is between ∼4 to 8 mins.

Using a cross-correlation method to calculate the individual transition times, such as in Chapter 4, would introduce bias toward finding perfect draping since only those periods where the clock angles matched (i.e. perfect draping) would provide distinct correlation peaks. Instead, the statistical effect of altering the transition time (from 3 to 8 mins) was investigated by performing our data analysis for each of the transition times and determining the standard deviation of the resultant data. Although there was very little difference between the resultant distributions, the results from the transition time with the smallest standard deviation (5 mins) are presented.

A matching one hour window of one minute resolution data is selected, based upon the crossing of the magnetopause by the Cluster satellites, for both the Cluster and OMNI data. To determine the effect of the draping on the magnetic field in the magnetosheath, the clock angle is then computed and compared for each of the corresponding data points in that window. For perfect draping, the difference between the clock angle at the bow shock and the corresponding clock angle at the magnetopause should be within $\pm 10^{\circ}$.

6.3 Results and Discussion

For this study, there are 2,688 usable magnetopause crossings from the crossing database of *Case and Wild* (2013) covering the seasons 2002 through 2010, which provides data for a total of 160,708 clock angles measurements. In the following section, the data are presented in a similar form to the data in *Coleman* (2005) to allow for direct comparisons.

Presented in Figure 6.1 is the unfiltered data. The left hand panel of the figure shows the average positions of the Cluster spacecraft during this investigation, within square bins of size 2 R_E, plotted as filled circles in the GSM y-z plane. The average location is not necessarily located at the centre of the bin and so two (or more) average locations can, in fact, be much closer together than 2 R_E. The colour of the filled circles indicates the average angular difference between the clock angle near the magnetopause and the clock angle at the bowshock for the data in the bin. The filled circles are coloured green for small angular differences ($d \leq 30°$), blue for moderate differences ($30° < d \leq 90°$) and red for large differences ($d > 90°$). The mean clock angle of the near magnetopause data is indicated by a radial line and the standard deviation of the magnetopause clock angles is show by an arc segment which subtends to an angle of twice the standard deviation.

Note that a simple mean is not appropriate when averaging clock angles. For example, the average of $-179°$ and $179°$ is zero, however, the correct average in this case should be +/-180°. So, in order to calculate the mean clock angle for multiple clock angles, two means were taken: one for angles in the range of $[-180°, 180°]$ and one for $[0°, 360°]$. The case with the lowest standard deviation was taken as the mean (and then shifted by 180° if appropriate).

The right hand panel of Figure 6.1 shows the angular differences between the clock angles near the magnetopause and the clock angles at the bowshock. The four histograms in that panel show the distribution of differences for all of the magnetopause as well as three specific regions: subsolar, flanks and high latitude (whose locations are indicated in the plot in the left panel).

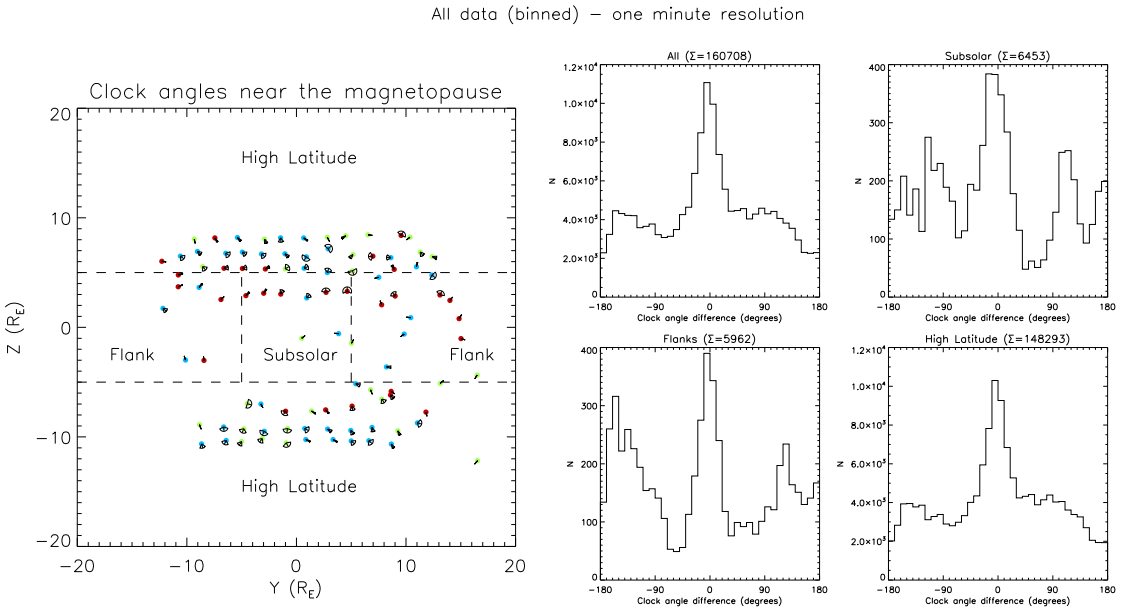

FIGURE 6.1: Clock angles and angular differences measured near the magnetopause with no filtering. (left) Each filled circle is centred at the average spacecraft location (GSM) within a 2 R_E bin. The fill colour indicates the angular difference from perfect draping: green for a difference of less than 30°, blue for a difference of between 30° and 90° and red for a difference greater than 90°. The mean clock angle of each bin is shown with a radial line, with the standard deviation represented by an arc of angular width equal to twice the standard deviation. (right) The difference from perfect draping for all clock angle data points and for clock angles filtered by location on the magnetopause.

For each of the histograms in Figure 6.1 there is a clear peak centred around a difference of zero degrees, with a half-width of approximately 30°. The plots clearly demonstrate that the vast majority of data points are collected in the high latitude region, with a smaller similar-sized fraction of the data collected from both the flanks and subsolar regions, respectively. The location of the peak is consistent with *Coleman* (2005) (see Figure 6.2), however, there is a lot more variation than was present in the results of that

study. The flanks data have the highest level of variation (with a standard deviation of 107.0°), the high latitude data have the lowest (standard deviation of 89.7°) with the subsolar data having a standard deviation of 99.5°.

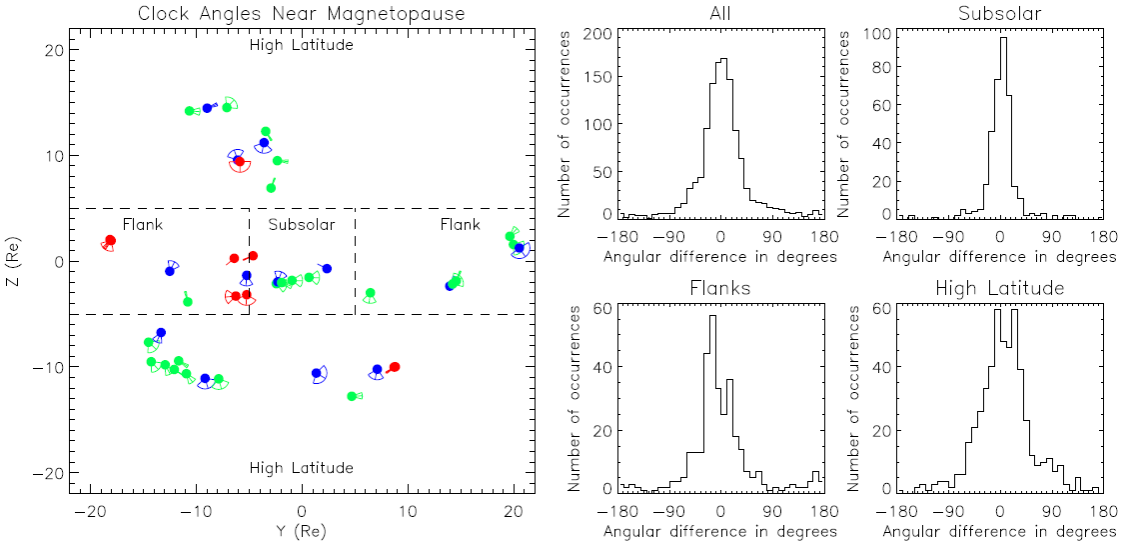

FIGURE 6.2: Figure 2 from *Coleman* (2005) - with the same format and conditions as Figure 6.1.

To determine if there is any dependence upon the draping magnitude to the original IMF orientation, the data are split and grouped depending upon the upstream IMF. Data which correspond to a "northward" IMF (in which the OMNI clock angle is $-15° < \theta < 15°$) are plotted in Figure 6.3.

The northward IMF data is once again predominately taken from the high latitude region and so the "All" histogram closely resembles the "High Latitude" histogram. In these two histograms there is a distinct peak at around $100 - 160°$. With the other regions, there is much less data, however, peaks have formed at around $30 - 50°$. The high latitude region has the most variability, with a standard deviation of 87.0°, whilst the flanks and subsolar regions have much less variability with standard deviations of 41.6° and 23.0° respectively.

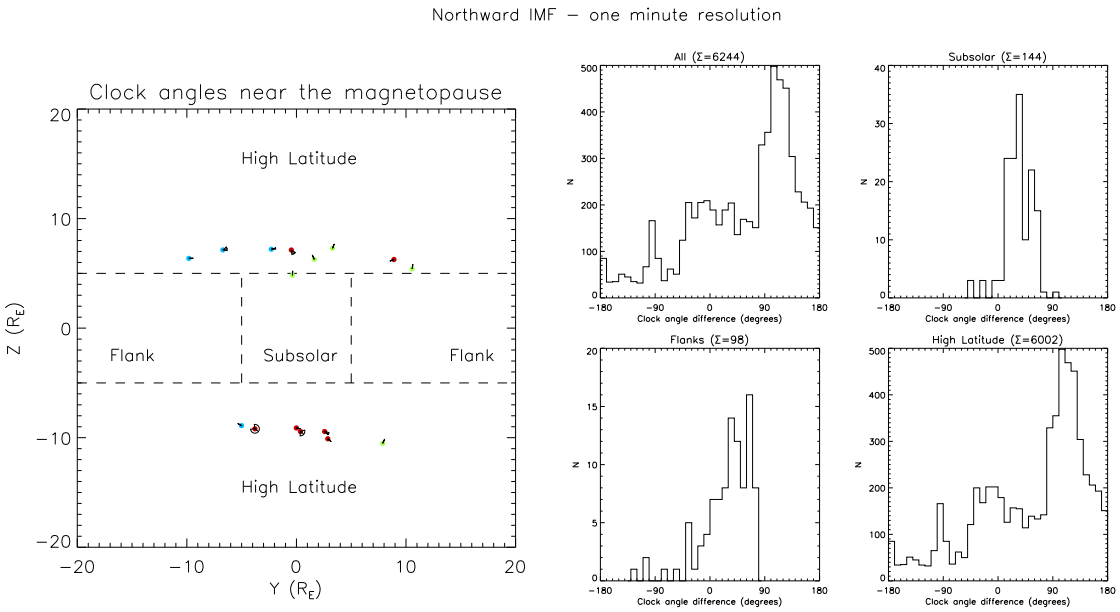

FIGURE 6.3: Clock angles and angular differences measured near the magnetopause for northward IMF - same format as Figure 6.1.

Data in which the corresponding IMF was "eastward" (i.e. OMNI clock angle of $45° < \theta < 135°$), are plotted in Figure 6.4.

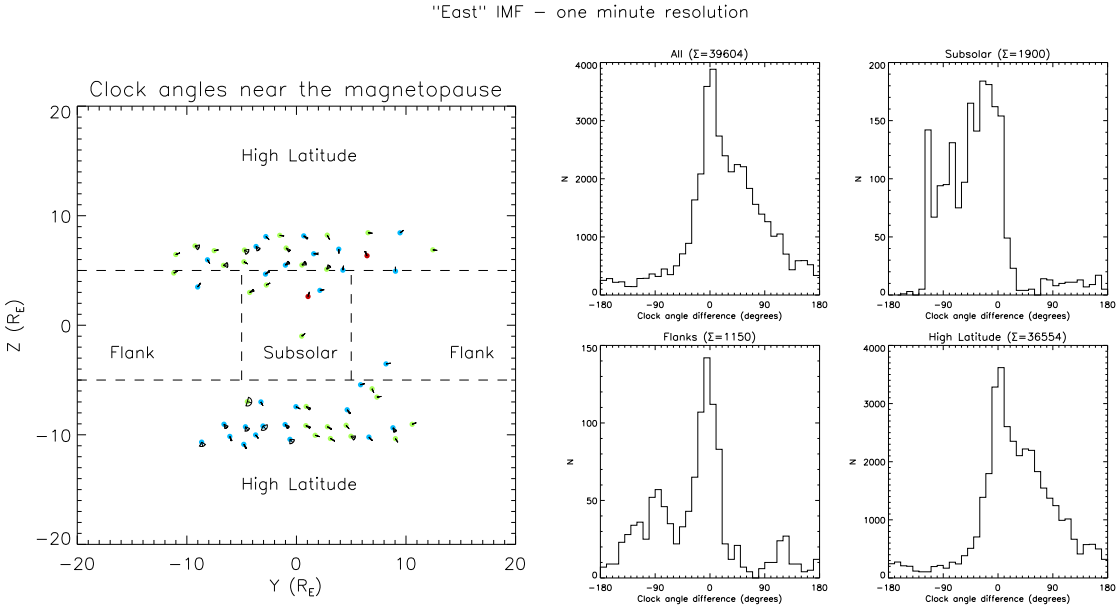

FIGURE 6.4: Clock angles and angular differences measured near the magnetopause for eastward IMF - same format as Figure 6.1.

The eastward upstream IMF group contains approximately 25% of the whole data set

and is the largest IMF grouping shown, closely followed by the westward group (shown in Figure 6.6) which contains approximately 23% of the data set, which is perhaps not surprising due to the Parker spiral configuration of the solar wind favouring an east/west IMF direction. All three magnetospheric regions have a peak around zero degrees difference, though they all have very different distributions. The high latitude data is positively skewed with a large "tail" existing at positive angular differences but no (or a very small) tail existing at negative angular differences. Conversely, the subsolar data is negatively skewed. The flank data is generally very variable. The standard deviations for the three regions are: high latitude 64.5°, flanks 71.8° and subsolar 56.5°.

Data for "southward" IMF, in which the OMNI clock angle is $\theta > 165°$ or $\theta < -165°$, are presented in Figure 6.5.

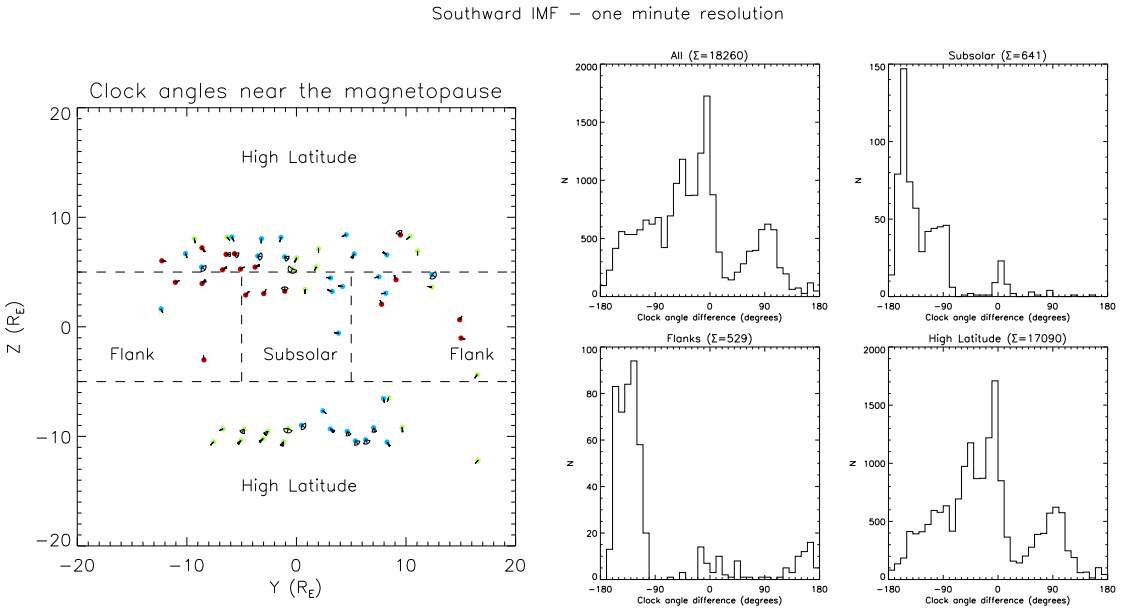

FIGURE 6.5: Clock angles and angular differences measured near the magnetopause for southward IMF - same format as Figure 6.1.

The subsolar and flanks histograms, again, show a similar distribution with the majority of differences being between $-90°$ and $-180°$. The high latitude data, of which there are

approximately 100 times more of than subsolar or flanks data, has a peak around zero degrees difference but also has smaller peaks around ±90°. The standard deviations for each of the regions are: high latitude 74.6°, flanks 93.7° and subsolar 51.2°.

Data in which the corresponding IMF was "westward" (i.e. OMNI clock angle of $-135° < \theta < -45°$), are plotted in Figure 6.6.

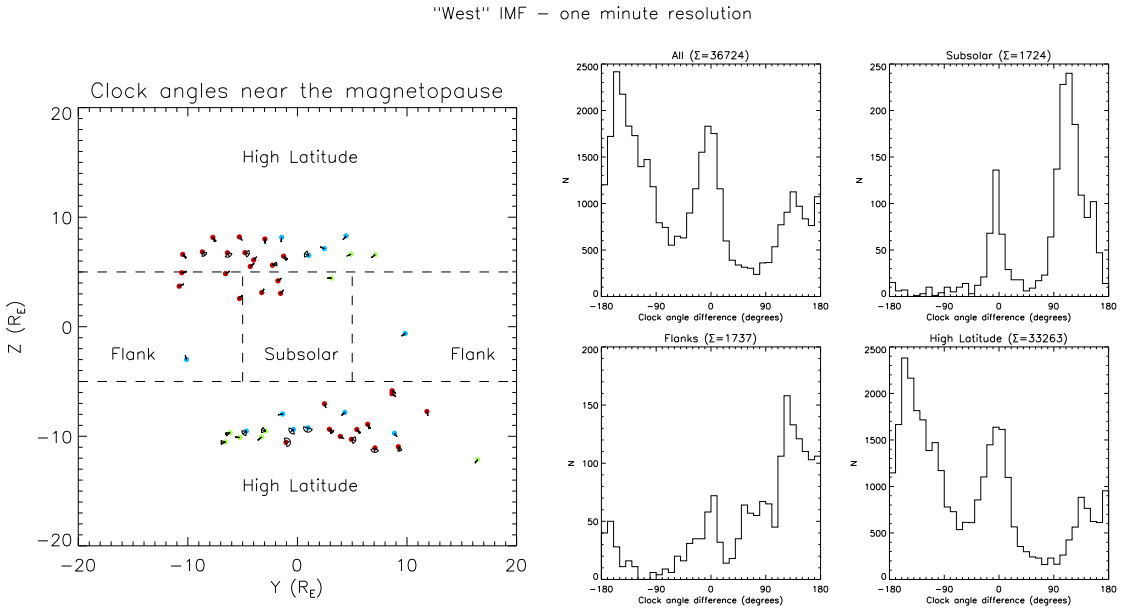

FIGURE 6.6: Clock angles and angular differences measured near the magnetopause for westward IMF - same format as Figure 6.1.

The high latitude region histogram has three distinct peaks at ±150° difference and at zero degrees difference. It has a standard deviation of 103.8°. The subsolar and flanks histograms both have two primary peaks at 150° and zero degrees difference and have standard deviations of 70.0° and 95.9°, respectively.

6.4 Conclusions

This study used eight years of Cluster and OMNI data to determine the difference between the clock angles at the bow shock and the magnetopause. The clock angle difference was used to investigate the effect of magnetic draping on the IMF in the shocked solar wind as it approached the magnetopause.

Owing to the orbital configuration of the Cluster satellites, most encounters with the magnetopause were at high latitude. Several draping studies have previously been conducted with low-mid latitude spacecraft (e.g. *Crooker et al.* (1985); *Coleman* (2005)), however, only a few have used high latitude data (e.g. *Longmore et al.* (2006)) and so this study was a useful exercise to add more high latitude data to the literature.

As shown in Figure 6.1, with no filtering of the data we find that there is a dominant peak (approximately 2.5× the height of the background level) at clock angle differences between ±30°. We note that in *Coleman* (2005) 30% of data points exhibit perfect draping (to within ±10°) and 70% are within ±30° whereas, in this study, we find that the values are 13% and 30% respectively.

In *Coleman* (2005), the distribution is much more confined about zero degrees difference with only a small number of occurrences in the tails of the distribution. This is in contrast to our results. However, this may be due to the fact that our data are predominantly from high-latitude regions whereas the data in *Coleman* (2005) were collected predominantly in the mid-low latitude region. *Coleman* (2005) noted there was high variability in high latitude data in their study and that this could be the result of of enhanced flow irregularities in the cusp entry layer. *Haerendel et al.* (1978) demonstrated

that eddy convection introduces magnetic turbulence near the cusp regions, which could help explain why the high latitude clock angle difference data are more variable. Additionally, this increased variability is also found in *Longmore et al.* (2006) who were investigating the effect of bulk plasma flows on the magnetic field in the magnetosheath.

To determine if the direction of the magnetic field affected the angular difference, the data were filtered based on the IMF orientation at the bowshock. It was clear that the IMF orientation does, indeed, have an affect on the draping angle - a result which is consistent with previous studies (e.g. *Coleman* (2005); *Longmore et al.* (2006)).

For all IMF orientations, other than eastward, the distributions of the angular differences between the clock angle at the magnetopause and at the bowshock show that there are peaks shifted away from zero degrees difference. It is only the eastward IMF orientation which shows a peak centred near zero degrees difference - though this distribution is dominated by the high latitude region which shows a positive skew.

For all of the IMF orientations, the results show that the flanks and subsolar regions often have similar distributions. The distribution for the high latitude region generally differs substantially from them both.

There are some possible systematic uncertainties in the calculation of the clock angles differences. Firstly, we have used an approximated transition time through the magnetosheath of 5 mins. Whilst this produced a distribution with the smallest standard deviation, when tested again other transition times, it does introduce possible errors in matching up the appropriate clock angle. Secondly, by using the OMNI web service for the bowshock data we have a convenient and large dataset available to us. However, OMNI's lagging of data from an upstream observer to the bowshock, whilst statistically

valid, also introduces error in matching up the correct clock angles (see Chapter 4). Finally, data is selected from the Cluster mission based upon the magnetopause locations stored in the crossing database created in Chapter 5. This database was created using an automated routine, to eliminate the need of manually identifying crossings, which could produce anomalous results and affect the differences in clock angle. Reducing the uncertainties in these measurements should be the focus of future comparative work.

The primary result of the study is that it should not be assumed that magnetic field at the magnetopause matches with the upstream IMF orientation. When conducting magnetopause studies, or studies which involve the orientation of the field near the magnetopause, one should endeavour to use *in situ* field measurements. This result is in clear agreement with studies such as *Coleman* (2005) and *Longmore et al.* (2006). It is therefore recommended that further work be undertaken to quantitatively investigate the impact of using estimated/lagged data over *in situ* data on studies into geo-effectiveness, for example.

We also note that many studies have used upstream data to identify the conditions at the magnetopause and that the results obtained are consistent with observations. This suggests that the magnetopause acts as a low-pass filter (e.g. *Tsurutani et al.* (1990), *Vassiliadis et al.* (1995) and *Archer et al.* (2013)) which negates any small time-scale turbulence in the shocked solar wind and instead reacts to longer time-scale changes. This postulation is further supported by the fact that the draping distributions were not significantly altered by our choice of magnetosheath transition times. Further investigation into this low-pass filter effect therefore seems warranted.

Chapter 7

Summary

The work in this thesis has been undertaken to investigate the interaction between the solar wind and the Earth's magnetosphere, particularly, it was of interest to determine whether one could predict the near-Earth magnetic field conditions using an upstream observer.

Determining whether this is possible is an important area of research, since much of the near-Earth research relies on accurate specification of the near-Earth magnetic field strength and orientation. Ideally, this accurate specification would be provided by near-Earth spacecraft, however, this is an unrealistic expectation. To keep spacecraft in proximity of the Earth they must be placed into an orbit about it and orbital mechanics require that the spacecraft will spend some period of time outside of the region of interest (e.g. in the nightside magnetosphere). Short of employing a "net" of spacecraft, which is cost prohibitive, the space physics community therefore relies upon upstream observers

(such as ACE at L1) to provide constant feedback on the specification of the solar wind and the embedded IMF.

Using an upstream observer presents its own challenges. Determining the appropriate propagation delay (i.e. the time it takes for the solar wind to travel from the upstream observer to the Earth) is non-trivial and so the OMNIweb dataset was created. This dataset lags upstream data, through a processed described in Section 3.5.1, to provide convenient near-Earth data.

The work carried out in Chapter 4 investigated the propagation delay between an upstream observer (in this case, the ACE spacecraft) and the Earth's bowshock. Using data from the Cluster mission, spanning nearly a whole solar cycle, the study compared "flat" delays and OMNI delays to calculated cross-correlation delays. The cross-correlation delay was determined by comparing simultaneous data from the ACE and Cluster spacecraft and performing a correlation analysis on the data. The point at which the two data sets best correlated was determined to be the propagation delay.

The primary finding of the study was that, whilst the OMNI propagation delays generally matched well with the calculated cross-correlation delays, there were occasions where the delays could differ by up to 50% (or around 30mins). Investigation of the delay differences found that there was no substantial dependence upon the solar wind or IMF conditions for the cross-correlation-OMNI relationship.

The conclusion drawn from this result is that whilst the OMNI delays are convenient and statistically valid, they should not be assumed accurate when studying individual events.

Improving space weather forecasting methods is a very active area of research at the moment. Investigating those instances where OMNI's predicted delay and the calculated cross correlation delay differ substantially would be a useful future exercise and should help to improve the accuracy of OMNI data and space weather forecasting in the future.

In this study, only one Cluster spacecraft was used. It would be interesting to include all four spacecraft in future studies. This would not only increase data coverage but would also allow calculation of the phase front normal (a core variable used when calculating the OMNI lag times) at the bowshock which could then be compared to the value determined at the upstream observer.

The propagation delay study looked at the IMF conditions at the bow shock, since this is where the OMNI data set lags its data to. However, to understand many of the near-Earth space physics processes, it is important to know the magnetic field conditions at Earth. Many studies have simply assumed that the IMF does not change significantly during its transit through the magnetosheath.

Before being able to test whether this assumption is valid, it was important to accurately determine the location of the magnetopause. Since the magnetopause location is variable and depends upon the impinging solar wind conditions, a statistical study to determine its location under a variety of upstream conditions and at a variety of magnetic latitudes and local times was undertaken. This study is presented in Chapter 5.

The study, which established and hence used a more generalised version of the *Ivchenko et al.* (2000) magnetopause detection routine, compared detected magnetopause crossing locations to predicted locations from four models.

The study found that the two empirical models of *Petrinec and Russell* (1996) and *Shue et al.* (1998) generally agreed well with each other, however, on average, they overestimated the radial distance to the magnetopause by over 1 R_E. The two newer models, *Dmitriev and Suvorova* (2000) and *Lin et al.* (2010), slightly underestimated the distance to the model magnetopause.

The results found in the study, along with the improved *Ivchenko et al.* (2000) routine, should help to improve future magnetopause location models. Additionally, the study created a database of 2709 magnetopause crossings which could then be used to determine the location of the magnetopause for a study of magnetic draping through the magnetosheath.

The study used magnetic field data exclusively to determine when a magnetopause crossing was made. This was convenient since the magnetic field data was the most reliable data set. However, it would be beneficial for future studies to investigate incorporating plasma data in the crossing criteria since it is well known that there are distinct differences between the plasma characteristics in the magnetosheath and magnetosphere.

In Chapter 6, a study was undertaken to investigate the modification of the IMF orientation as it traverses through the magnetosheath. Using the database of magnetopause crossings, created in Chapter 5, appropriate data periods were chosen from both the Cluster and OMNI magnetic field data sets.

Clock angles from OMNI and Cluster were compared to determine what changes may have occurred. The study, which predominantly used high latitude data, found that only 13% of the data showed perfect draping (where the clock angle difference was between $\pm 10^{\circ}$). Though in a previous study (*Coleman* (2005)) this figure was higher (30%), both

studies show that it is unrealistic to assume that the orientation of the IMF is unaffected during its transition through the magnetosheath.

Additionally, the study found that the distributions of clock angle differences were fairly consistent in the flank and subsolar regions. However, the clock angle differences varied more substantially in the high latitude region than in the other two regions.

A few assumptions were made in this study to help with data processing. Such assumptions include using a fixed transition time of 4 mins for the IMF to propagate from the bowshock to the magnetopause. Although this has been shown to be fairly accurate, better determination of this time would increase the accuracy of the results. The possibility of using a cross correlation method, such as that in Chapter 4, could be explored.

In each of the three studies an analysis of spacecraft data was undertaken - primarily ACE (or ACE and WIND via OMNI) and Cluster. Both the OMNI database and the Cluster mission have proved very reliable, however, there were periods of time in our investigations where data was unavailable. For this reason, particularly with the near-Earth data, it would be beneficial for future studies to include data from other spacecraft (such as Double Star, THEMIS or MSS). As well as generally increasing the amount of data available to analyse, adding in these additional data sources would increase the amount of data from the different regions of interest.

To summarise the results and conclusions of this thesis, the three studies undertaken primarily looked at magnetic field data taken by near-Earth spacecraft (Cluster) and compared this to upstream data (either from ACE or OMNI). In doing so, it was possible to test models and approximations which are currently in use in the space physics community.

It was found that, statistically, the OMNIweb data products were valid and could be used for large scale studies. However, it is not recommended that they be used for individual case studies, especially for those case studies which examine events occurring on short time scales, since the lagging process can, on occasion, be out by the order of 30 minutes.

Additionally, it is not safe to assume that the magnetic field orientation at the bowshock (such as that provided by OMNI) is preserved through the magnetosheath. Perfect draping is a very poor approximation and should not be used when determining the magnetic field orientation at the magnetopause.

When looking at the magnetopause location, it was found that the commonly used magnetopause model of *Shue et al.* (1998) was not particularly accurate, especially at high magnetic latitudes, and that newer models (such as *Dmitriev and Suvorova* (2000) and *Lin et al.* (2010)) proved better in this regard.

Bibliography

Angelopoulos, V., J. P. McFadden, D. Larson, C. W. Carlson, S. B. Mende, H. Frey, T. Phan, D. G. Sibeck, K.-H. Glassmeier, U. Auster, E. Donovan, I. R. Mann, I. J. Rae, C. T. Russell, A. Runov, X.-Z. Zhou, and L. Kepko (2008), Tail reconnection triggering substorm onset, *Science*, *321*(5891), 931–935, doi:10.1126/science.1160495.

Antiochos, S. K., C. R. DeVore, and J. A. Klimchuk (1999), A model for solar coronal mass ejections, *ApJ*, *510*, 485–493.

Archer, M. O., T. S. Horbury, J. P. Eastwood, J. M. Weygand, and T. K. Yeoman (2013), Magnetospheric response to magnetosheath pressure pulses: A low-pass filter effect, *J. Geophys. Res.*, *118*, doi:10.1002/jgra.50519.

Balogh, A., M. Dunlop, S. Cowley, D. Southwood, J. Thomlinson, K. Glassmeier, G. Musmann, H. LHR, S. Buchert, M. AcuA, D. Fairfield, J. Slavin, W. Riedler, K. Schwingenschuh, and M. Kivelson (1997), The cluster magnetic field investigation, *Space Science Reviews*, *79*(1-2), 65–91, doi:10.1023/A:1004970907748.

Baumjohann, W., and R. A. Treumann (1996), *Basic Space Plasma Physics*, Imperial College Press.

Berchem, J., and C. T. Russell (1982), The thickness of the magnetopause current layer: ISEE 1 and 2 observations, *J. Geophys. Res.*, *87*(A4), 2108–2114.

Biermann, L. (1951), Kometenschweife und solare korpuskularstrahlung, *Zeit. Astrophys*, *29*, 274.

Carrington, R. C. (1859), Description of a singular appearance seen in the sun on september 1, 1859, *Monthly Notices of the Royal Astronomical Society*, *20*, 13–15.

Case, N. A., and J. A. Wild (2012), A statistical comparison of solar wind propagation delays derived from multispacecraft techniques, *J. Geophys. Res.*, *117*(A2), doi:10.1029/2011JA016946.

Case, N. A., and J. A. Wild (2013), The location of the Earth's magnetopause: a comparison of modeled position and in-situ cluster data, *J. Geophys. Res.*, *118*, 6127–6135, doi:10.1002/jgra.50572.

Cavendish, H. (1790), On the height of the luminous arch which was seen on feb. 23, 1784, *Philosophical Transactions of the Royal Society of London*, *80*, 101–105.

Chang, S. C., and A. Nishida (1973), Spatial structure of transverse oscillations in the interplanetary magnetic field, *Astrophys. Space Sci.*, *23*, 301–314.

Chapman, S., and V. C. A. Ferraro (1931), A new theory of magnetic storm, i, the initial phase, *J. Geophys. Res.*, *36*(77).

Chiu, M. C., U. I. Von-Mehlem, C. E. Willey, T. M. Betenbaugh, J. J. Maynard, J. A. Krein, R. F. Conde, W. T. Gray, J. Hunt, J. W., L. E. Mosher, M. G. McCullough, P. E. Panneton, J. P. Staiger, and E. H. Rodberg (1998), ACE spacecraft, *Space Science Reviews*, *86*(1-4), 257–284, doi:10.1023/A:1005002013459.

Coleman, I. J. (2005), A multi-spacecraft survey of magnetic field line draping in the dayside magnetosheath, *Ann. Geophys.*, *23*, 885–900.

Credland, J., G. Mecke, and J. Ellwood (1997), The Cluster mission: Esas spacefleet to the magnetosphere, in *The Cluster and Phoenix Missions*, edited by C. Escoubet, C. Russell, and R. Schmidt, pp. 33–64, Springer Netherlands, doi:10.1007/978-94-011-5666-0_2.

Crooker, N. U., G. L. Siscoe, C. T. Russell, and E. J. Smith (1982), Factors controlling degree of correlation between ISEE 1 and ISEE 3 interplanetary magnetic field measurements, *J. Geophys. Res.*, *87*, 2224–2230.

Crooker, N. U., J. G. Luhman, C. . T. Russell, E. J. Smith, J. R. Spreiter, and S. S. Stahara (1985), Magnetic field draping against the dayside magnetopause, *J. Geophys. Res.*, *90*(A4), 3505–3510.

Davis, A. J., and G. Hamell (2008), A data services upgrade for advanced composition explorer (ACE) data, *AGU Fall Meeting Abstracts*, p. A1562.

Dmitriev, A. V., and A. V. Suvorova (2000), Three-dimensional artificial neural network model of the dayside magnetopause, *J. Geophys. Res.*, *105*(A8), 18,909–18,918, doi: 10.1029/2000JA900008.

Dmitriev, A. V., A. V. Suvorova, and J.-K. Chao (2011), A predictive model of geosynchronous magnetopause crossings, *J. Geophys. Res.*, *116*(A05208), doi:10.1029/ 2010JA016208.

Dungey, J. W. (1961), Interplanetary magnetic field and the auroral zones, *Phys. Rev. Lett.*, *6*(2), 47–48.

Dušík, Š. G., J. Granko, Šafránková, Z. Němeček, and K. Jelínek (2010), IMF cone angle control of the magnetopause location: Statistical study, *Geophys. Res. Lett*, *37*(L19103), doi:10.1029/2010GL044965.

Escoubet, C. P., R. Schmidt, and M. Goldstein (1997), Cluster science and mission overview, *Space Science Reviews*, *79*, 11–32, doi:10.1023/A:1004923124586.

Escoubet, C. P., M. Fehringer, and M. Goldstein (2001), The cluster mission, *Ann. Geophys.*, *19*, doi:10.5194/angeo-19-1197-2001.

Fairfield, D. H. (1971), Average and unusual locations of the Earth's magnetopause and bow shock, *J. Geophys. Res.*, *78*(23), 6700–6716.

Farris, M. H., and C. T. Russell (1994), Determining the standoff distance of the bow shock: Mach number dependence and use of models, *J. Geophys. Res.*, *99*, 17,681–17,689.

Fritz, T., B. Walsh, M. Klida, and J. Chen (2012), The cusp as a source of magnetospheric particles, *Journal of Atmospheric and Solar-Terrestrial Physics*, *87-88*, 39–46, doi: 10.1016/j.jastp.2011.10.016.

Gloag, J. M., E. A. Lucek, L.-N. Alconcel, A. Balogh, P. Brown, C. M. Carr, C. N. Dunford, T. Oddy, and J. Soucek (2010), FGM data products in the CAA, in *The*

Cluster Active Archive, edited by H. Laakso, M. Taylor, and C. P. Escoubet, Astrophysics and Space Science Proceedings, pp. 109–128, Springer Netherlands, doi: 10.1007/978-90-481-3499-1_7.

Gloeckler, G., J. Cain, F. M. Ipavich, E. O. Tums, P. Bedini, L. A. Fisk, T. H. Zurbuchen, P. Bochsler, J. Fischer, R. F. Wimmer-Schweingruber, J. Geiss, and R. Kallenbach (1998), Investigation of the composition of solar and interstellar matter using solar wind and pickup ion measurements with SWICS and SWIMS on the ACE spacecraft, in *The Advanced Composition Explorer Mission*, edited by C. T. Russell, R. A. Mewaldt, and T. T. Rosenvinge, pp. 497–539, Springer Netherlands, doi: 10.1007/978-94-011-4762-0_18.

Gombosi, T. I. (1998), *Physics of the Space Environment*, Cambridge University Press.

Haaland, S., G. Paschmann, and B. U. O. Sonnerup (2006), Comment on A new interpretation of weimer et al.'s solar wind propagation delay technique by Bargatze et al., *J. Geophys. Res.*, *111*.

Haerendel, G., G. Paschmann, N. Sckopke, H. Rosenbauer, and P. C. Hedgecock (1978), The frontside boundary layer of the magnetosphere and the problem of reconnection, *J. Geophys. Res.*, *83*(A7), 31953216, doi:10.1029/JA083iA07p03195.

Hapgood, M. A., and D. A. Bryant (1990), Re-ordered electron data in the low-latitude boundary layer, *Geophys. Res. Lett*, *17*, 2043–2046.

Hapgood, M. A., T. G. Dimbylow, D. C. Sutcliffe, P. A. Chaizy, P. S. Ferron, P. M. Hill, and X. Y. Tiratay (1997), The joint science operations centre, *Space Sci. Rev.*, *79*, 487–525.

Heikkila, W. J., and J. D. Winningham (1971), Penetration of magnetosheath plasma to low altitudes through the dayside magnetospheric cusps, *J. Geophys. Res.*, *76*(4), 883–891, doi:10.1029/JA076i004p00883.

Horbury, T. S., D. Burgess, M. Franz, and C. J. Owen (2001), Prediction of Earth arrival times of interplanetry southward magnetic field turnings, *J. Geophys. Res.*, *106*, 30,001–30,009.

Iju, T., M. Tokumaru, and K. Fujiki (2013), Radial speed evolution of interplanetary coronal mass ejections during solar cycle 23, *Solar Phys*, *288*, 331–353.

Ivchenko, N. V., D. G. Sibeck, K. Takahashi, and S. Kokubun (2000), A statistical study of the magnetosphere boundary crossings by the geotail satellite, *Geophys. Res. Lett*, *27*(18), 2881–2884.

Khan, H., and S. W. H. Cowley (1999), Observations of the response time of high-latitude ionospheric convection to variations in the interplanetary magnetic field using EISCAT and IMP-8 data, *Ann. Geophys.*, *17*, 1306–1335.

Kivelson, M. G., and C. T. Russell (Eds.) (1995), *Introduction to Space Physics*, Cambridge University Press.

Knetter, T., and F. M. Neubauer (2004), Four-point discontinuity observations using Cluster magnetic field data: A statistical survey, *J. Geophys. Res.*, *109*, doi:doi:10.1029/2003JA010099.

Kobel, E., and E. O. Flückinger (1994), A model of the steady state magnetic field in the magneticsheath, *J. Geophys. Res.*, *99*, 617–623.

Koon, W. S., M. W. Lo, J. E. Marsden, and S. D. Ross (2008), *Dynamical Systems, the Three-Body Problem and Space Mission Design*, Marsden Books.

Kuznetsov, S. N., and A. V. Suvorova (1997), Magnetopause shape near geosynchronous orbit (in Russian), *Geomagn. Aeron*, *37*(3), 1–11.

Laakso, H., M. Taylor, and C. P. Escoubet (Eds.) (2010), *The Cluster Active Archive*, Astrophysics and Space Science Proceedings, Springer New York.

Lin, R. L., X. X. Zhang, S. Q. Liu, Y. L. Wang, and J. C. Gong (2010), A three-dimensional asymmetric magnetopause model, *J. Geophys. Res.*, *115*, doi:10.1029/2009JA014235.

Longmore, M., S. Schwartz, and E. Lueck (2006), Rotation of the magnetic field in Earth's magnetosheath by bulk magnetosheath plasma flow, *Ann. Geophys.*, *24*, 339–354, doi:10.5194/angeo-24-339-2006.

Luhmann, J. G., R. J. Warniers, C. T. Russell, J. R. Spreiter, and S. S. Stahara (1986), A gas dynamic magnetosheath field model for unsteady interplanetary fields: Application to the solar wind interaction with venus, *J. Geophys. Res.*, *91*(A3), 3001–3010, doi: 10.1029/JA091iA03p03001.

Mailyan, B., C. Munteanu, and S. Haaland (2008), What is the best method to calculate the solar wind propagation delay?, *Ann. Geophys.*, *26*, 2383–2394.

McComas, D. J., S. J. Bame, P. Barker, W. C. Feldman, J. L. Phillips, P. Riley, and J. W. Griffee (1998), Solar wind electron proton alpha monitor (SWEPAM) for the advanced composition explorer, in *The Advanced Composition Explorer Mission*, edited by C. T. Russell, R. A. Mewaldt, and T. T. Rosenvinge, pp. 563–612, Springer Netherlands, doi:10.1007/978-94-011-4762-0-20.

McComas, D. J., H. A. Elliott, N. A. Schwadron, J. T. Gosling, R. M. Skoug, and B. E. Goldstein (2003), The three-dimensional solar wind around solar maximum, *Geophys. Res. Lett.*, p. 1517, doi:10.1029/2003GL017136.

Nishida, A. (1994), The geotail mission, *Geophys. Res. Lett*, *21*, 2871–2873, doi:10.1029/94GL01223.

Nykyri, K., A. Otto, E. Adamson, E. Kronberg, and P. Daly (2012), On the origin of high-energy particles in the cusp diamagnetic cavity, *Journal of Atmospheric and Solar-Terrestrial Physics*, *87-88*, 70–81, doi:10.1016/j.jastp.2011.08.012.

Parker, E. N. (1958), Dynamics of the interplanetary gas and magnetic fields, *Astrophys. J.*, *128*, 664.

Parker, E. N. (1960), The magnetohydrodynamic treatment of the expanding corona, *Astrophys J.*, *132*, 175.

Petrinec, S. M., and C. T. Russell (1993), An empirical model of the size and shape of the near-Earth magnetotail, *Geophys. Res. Lett*, *20*(2695).

Petrinec, S. M., and C. T. Russell (1996), Near-Earth magnetotail shape and size as determined from the magnetopause flaring angle, *J. Geophys. Res.*, *101*.

Petrinec, S. M., P. Song, and C. T. Russell (1991), Solar cycle variation in the size and shape of the magnetopause, *J. Geophys. Res.*, *96*, 7893–7896.

Pizzo, V. (1978), A three-dimensional model of corotating streams in the solar wind, 1. theoretical foundations, *J. Geophys. Res.*, (A12).

Rème, H., C. Aoustin, J. M. Bosqued, I. Dandouras, B. Lavraud, J. A. Sauvaud, A. Barthe, J. Bouyssou, T. Camus, O. Coeur-Joly, A. Cros, J. Cuvilo, F. Ducay, Y. Garbarowitz, J. L. Medale, E. Penou, H. Perrier, D. Romefort, J. Rouzaud, C. Vallat, D. Alcaydé, C. Jacquey, C. Mazelle, C. d'Uston, E. Möbius, L. M. Kistler, K. Crocker, M. Granoff, C. Mouikis, M. Popecki, M. Vosbury, B. Klecker, D. Hovestadt, H. Kucharek, E. Kuenneth, G. Paschmann, M. Scholer, N. Sckopke, E. Seidenschwang, C. W. Carlson, D. W. Curtis, C. Ingraham, R. P. Lin, J. P. McFadden, G. K. Parks, T. Phan, V. Formisano, E. Amata, M. B. Bavassano-Cattaneo, P. Baldetti, R. Bruno, G. Chionchio, A. Di Lellis, M. F. Marcucci, G. Pallocchia, A. Korth, P. W. Daly, B. Graeve, H. Rosenbauer, V. Vasyliunas, M. McCarthy, M. Wilber, L. Eliasson, R. Lundin, S. Olsen, E. G. Shelley, S. Fuselier, A. G. Ghielmetti, W. Lennartsson, C. P. Escoubet, H. Balsiger, R. Friedel, J.-B. Cao, R. A. Kovrazhkin, I. Papamastorakis, R. Pellat, J. Scudder, and B. Sonnerup (2001), First multispacecraft ion measurements in and near the Earth's magnetosphere with the identical cluster ion spectrometry (CIS) experiment, *Annales Geophysicae*, *19*(10/12), 1303–1354, doi: 10.5194/angeo-19-1303-2001.

Richardson, J. D., F. Dashevskiy, and K. I. Paularena (1998), Solar wind plasma correlations between L1 and Earth, *J. Geophys. Res.*, *103*, 14,619–14,629.

Roelof, E. C., and D. G. Sibeck (1993), Magnetopause shape as a bivariate function of interplanetary magnetic field bz and solar wind dynamic pressure, *J. Geophys. Res.*, *98*, 21,421–21,450, doi:10.1029/93JA02362.

Sari, J. G., and G. C. Valley (1976), Interplanetary magnetic field power spectra: Mean field radial or perpendicular to radial, *J. Geophys. Res.*, *81*, 5489–5499.

Shen, C., M. Dunlop, Y. H. Ma, Z. Q. Chen, G. Q. Yan, Z. X. Liu, Y. V. Bogdanova, D. G. Sibeck, C. M. Carr, Q. H. Zhang, and E. Lucek (2011), The magnetic configuration

of the high-latitude cusp and dayside magnetopause under strong magnetic shears, *J. Geophys. Res.*, *116*(A09228), doi:10.1029/2011JA016501.

Shue, J. H., J. K. Chao, H. C. Fu, C. T. Russell, P. Song, K. K. Khurana, and H. J. Singer (1997), A new functional form to study the solar wind control of the magnetopause size and shape.

Shue, J.-H., P. Song, C. T. Russell, J. T. Steinberg, J. K. Chao, G. Zastenker, O. L. Vaisberg, S. Kokubun, H. J. Singer, T. R. Detman, and H. Kawano (1998), Magnetopause location under extreme solar wind conditions, *J. Geophys. Res.*, *103*(A8), 17,691–17,700, doi:10.1029/98JA01103.

Sibeck, D. G., R. E. Lopez, and E. C. Roelof (1991), Solar wind control of the magnetopause shape, location, and motion, *J. Geophys. Res.*, *96*(A4), 54895495, doi:10.1029/90JA02464.

Smith, C. W., J. L'Heureux, N. F. Ness, M. H. Acua, L. F. Burlaga, and J. Scheifele (1998), The ACE magnetic fields experiment, in *The Advanced Composition Explorer Mission*, edited by C. T. Russell, R. A. Mewaldt, and T. T. Rosenvinge, pp. 613–632, Springer Netherlands, doi:10.1007/978-94-011-4762-0_21.

Song, P., R. C. Elphic, and C. T. Russell (1988), ISEE 1 and 2 observations of the oscillating magnetopause, *Geophys. Res. Lett*, *15*, 744.

Sonnerup, B. U. O., and M. Scheible (1998), Minimum and maximum variance analysis, in *Analysis Methods for Multi-Spacecraft Data*, edited by G. Paschmann and P. W. Daly, Int. Space Sci. Inst.

Spreiter, J. R., A. L. Summers, and A. Y. Alksne (1966), Hydromagnetic flow around the magnetosphere, *Planetary and Space Science*, pp. 223–253.

Stone, E. C., A. M. Frandsen, R. A. Mewaldt, E. R. Christian, D. Margolies, J. F. Ormes, and F. Snow (1998), The advanced composition explorer, *Space Science Reviews*, *86*(1-4), 1–22, doi:10.1023/A:1005082526237.

Suvorova, A., A. Dmitriev, and S. Kuznetsov (1999), Dayside magnetopause models, *Rad. Meas.*, *30*.

Suvorova, A. V., J.-H. Shue, A. V. Dmitriev, D. Sibeck, J. McFadden, H. Hasegawa, K. Ackerson, K. Jelinek, J. Safrankova, and Z. Nemecek (2010), Magnetopause expansions for quasi-radial interplanetary magnetic field: Themis and geotail observations, *J. Geophys. Res.*, *115*(A10216), doi:10.1029/2010JA015404.

Tsurutani, B., M. Sugiura, T. Iyemori, B. Goldstein, W. Gonzalez, S. Akasofu, and E. Smith (1990), The nonlinear response of AE to the IMF Bs driver: a spectral break at 5h, *Geophys. Res. Lett.*, *17*, 279–282.

Vassiliadis, D., A. Klimas, D. Baker, and D. Roberts (1995), A description of the solar windmagnetosphere coupling based on nonlinear filters, *J. Geophys. Res.*, pp. 3495–3512.

Šafránková, J., Z. Němeček, Š. Duší k, L. Přech, D. G. Sibeck, and N. N. Borodkova (2002), The magnetopause shape and location: a comparison of the interball and geotail observations with models, *Ann. Geophys.*, *20*, 301–309.

Wang, C.-P., M. Gkioulidou, L. R. Lyons, and V. Angelopoulos (2012), Spatial distributions of the ion to electron temperature ratio in the magnetosheath and plasma sheet, *J. Geophys. Res.*, *117*, doi:10.1029/2012JA017658.

Weimer, D. R. (2004), Correction to Predicting interplanetary magnetic field (IMF) propagation delay times using the minimum variance technique, *J. Geophys. Res.*, *109*.

Weimer, D. R., and J. H. King (2008), Improved calculations of interplanetry magnetic field phase front angles and propagation time delays, *J. Geophys. Res.*, *113*(A01105), doi:10.1029/2007JA012452.

Weimer, D. R., D. M. Ober, N. C. Maynard, M. R. Collier, D. J. McComas, N. F. Ness, C. W. Smith, and J. Waterman (2003), Predicting interplanetry magnetic field (IMF) propagation delay times using the minimum variance technique, *J. Geophys. Res.*, *108*(1026).

Wild, J. A. (2000), Electrodynamics of the auroral ionosphere during magnetospheric substorms, Ph.D. thesis, University of Leicester.

Wild, J. A., E. E. Woodfield, and S. K. Morley (2009), On the triggering of auroral substorms by northward turnings of the interplanetary magnetic field, *Ann. Geophys.*, *27*(9), 3559–3570, doi:10.5194/angeo-27-3559-2009.

Wright, J., T. Lennon, R. Corell, N. Ostenso, W. Huntress Jr, J. Devine, P. Crowley, and J. Harrison (1995), The national space weather program, strategic plan. office of the federal coordinator for meteorological services and supporting research, *Tech. rep.*, Publication FCM-P30-1995 (Washington, DC).

Zhou, X. W., C. T. Russell, G. Le, S. A. Fuselier, and J. D. Scudder (2000), Solar wind control of the polar cusp at high altitude, *J. Geophys. Res.*, *105*(A1), 245–251, doi:10.1029/1999JA900412.

Zwickl, R. D., K. A. Doggett, S. Sahm, W. P. Barrett, R. N. Grubb, T. R. Detman, V. J. Raben, C. W. Smith, P. Riley, R. E. Gold, R. A. Mewaldt, and T. Maruyama (1998), The noaa real-time solar-wind (RTSW) system using ACE data, in *The Advanced Composition Explorer Mission*, edited by C. T. Russell, R. A. Mewaldt, and T. T. Rosenvinge, pp. 633–648, Springer Netherlands, doi:10.1007/978-94-011-4762-0_22.